Title
Aluminum Nitride Sensors for Harsh Environments

Author
Goericke, Fabian Thomas

Publication Date
2013

Peer reviewed|Thesis/dissertation

Aluminum Nitride Sensors for Harsh Environments

by

Fabian Thomas Goericke

A dissertation submitted in partial satisfaction of the

requirements for the degree of

Doctor of Philosophy

in

Engineering – Mechanical Engineering

in the

Graduate Division

of the

University of California, Berkeley

Committee in charge:

Professor Albert P. Pisano, Chair
Professor Tsu-Jae King Liu
Professor Liwei Lin

Fall 2013

Aluminum Nitride Sensors for Harsh Environments

by

Fabian Thomas Goericke

Abstract

Aluminum Nitride Sensors for Harsh Environments

by

Fabian Thomas Goericke

Doctor of Philosophy in Engineering – Mechanical Engineering

University of California, Berkeley

Professor Albert P. Pisano, Chair

Harsh environment applications include high temperature, pressure and mechanical shock. Aluminum nitride is a strong ceramic material with very good high temperature survivability. It also has piezoelectric properties that can be used for sensing applications and it can be deposited with good control as thin polycrystalline film for the fabrication of micro-electromechanical systems. In this dissertation, optimized deposition parameters for aluminum nitride films and characterization techniques for film stress gradients are investigated. Furthermore, two different fabrication processes are presented that can be used to build several sensors and other micromechanical elements on a single chip. The more advanced process includes a bulk-micromachining step that enables the use of the silicon substrate as large proof masses for accelerometers. At the same time, the fabrication process can be used to create membranes for devices such as pressure sensors. Several different devices are discussed from the device design and theoretical analysis to the fabrication and experimental verification. The most significant contribution is the performance improvement of several orders of magnitude that can be achieved with aluminum nitride accelerometers by switching from double-ended tuning forks to triple-beam tuning forks and by using the newly discovered sensing concept of bent-beam sensing. Additionally, rate gyroscopes were presented that use aluminum nitride as the structural material and for both actuating the drive axis and reading the sense axis. Both types of sensors have potential applications in inertial navigation at high temperature. Double-ended tuning forks and triple-beam tuning forks were tested in hot environment and it was shown that they can be used as highly sensitive strain sensors up to at least 570 °C. Additionally, a testing setup for high temperature testing of accelerometers was demonstrated.

Contents

List of Figures

List of Tables

Acronyms

AC alternating current.

AlN aluminum nitride.

ASIC application-specific integrated circuit.

BCl_3 boron tricholoride.

BHF buffered hydrofluoric acid.

BMAD the Berkeley Micromechanical Analysis and Design Laboratory.

C_4F_8 octafluorocyclobutane.

CAD computer-aided design.

CF_4 tetrafluoromethane.

CHF_3 fluoroform.

Cl_2 chlorine.

CM cassette module.

CMOS complementary metal-oxide-semiconductor.

CTE coefficient of thermal expansion.

DC direct current.

DETF double-ended tuning fork.

DUT device under test.

EMI electromagnetic interference.

ESC electronic stability control.

FBAR film bulk acoustic resonator.

FEM finite element method.

FWHM full width at half maximum.

GPS global positioning system.

HF hydrofluoric acid.

IMU inertial measurement unit.

IR infrared.

LPCVD low temperature chemical vapor deposition.

MEMS micro-electromechanical system.

PCB printed circuit board.

PI proportional-integral.

PID proportional-integral-derivative.

PLL phase-locked loop.

PM process module.

RF radio frequency.

RIE reactive ion etching.

RMS root mean square.

SAU stress adjustment unit.

SEM scanning electron microscope.

SF_6 sulfur hexafluoride.

Si_3N_4 silicon nitride.

SiC silicon carbide.

SiO_2 silicon dioxide.

SMT surface mount technology.

TBTF triple-beam tuning fork.

TM transfer module.

TMAH tetramethylammonium hydroxide.

XeF_2 xenon difluoride.

XRD x-ray diffraction.

Acknowledgements

I thank my research adviser Professor Albert Pisano for his support in the long and strenuous Ph.D. process. I am grateful for the unique opportunity to follow my own interests in many different aspects of my research field without constantly having to worry about funding sources and logistics. Of equal importance to my eventual success and especially to my mental sanity was my fiancée Hanna with her unconditional love and constant encouragement.

I am also grateful for the support from my dissertation committee members Professor Tsu-Jae King Liu and Professor Liwei Lin.

I am thankful to my parents for putting me on the right path and supporting my endeavors in every way possible throughout the years. Special thanks go out to my office mates Matthew Chan, Wei-Cheng Lien, Chris McCoy, Michael Sheppy, Sarah Wodin-Schwartz, who have helped me more than once when I could not figure out a problem by myself and have become friends for life. I would also acknowledge Gabriele Vigevani for being a great research partner and friend. Without his previous work and his help this dissertation would not have had nearly as many results. The same is true for Kansho Yamamoto, who was a major contributor to the advanced aluminum nitride fabrication process and a great person to work with. I was also very lucky to have the help of two very smart and hard-working undergraduate researchers Ivan Maríc and Sumeet Singh. I received an enormous amount of help from Igor Izyumin and Mitchell Kline and I cannot thank them enough for their selfless support with electrical circuits and measurements. Kirti Mansukhani has been a great person to work with and I hope that she continues this research and takes it to the next level. I would also like to acknowledge Debbie Senesky, who has become both a mentor and a good friend to me.

All members of the Berkeley Micromechanical Analysis and Design Laboratory have been a pleasure to work with and I thank them for their support. The staff of the Berkeley Sensor & Actuator Center was extremely helpful over the years and deserves special thanks. The same is true for staff members of the Berkeley Marvell Nanofabrication Laboratory, especially Kim Chan, Joe Donnelly, Bill Flounders, Jay Morford and Ryan Rivers.

Chapter 1

Introduction

This dissertation research attempts to develop aluminum nitride (AlN) sensor technology with the potential of deployment in harsh environment conditions. It represents one building block of an envisioned autonomous harsh environment sensing system under development at the Berkeley Micromechanical Analysis and Design Laboratory (BMAD). Figure 1.1 shows a schematic view of the sensor chip and lists the current researchers working on the individual projects as a quick reference to find literature. AlN is a promising material for the micro-electromechanical system

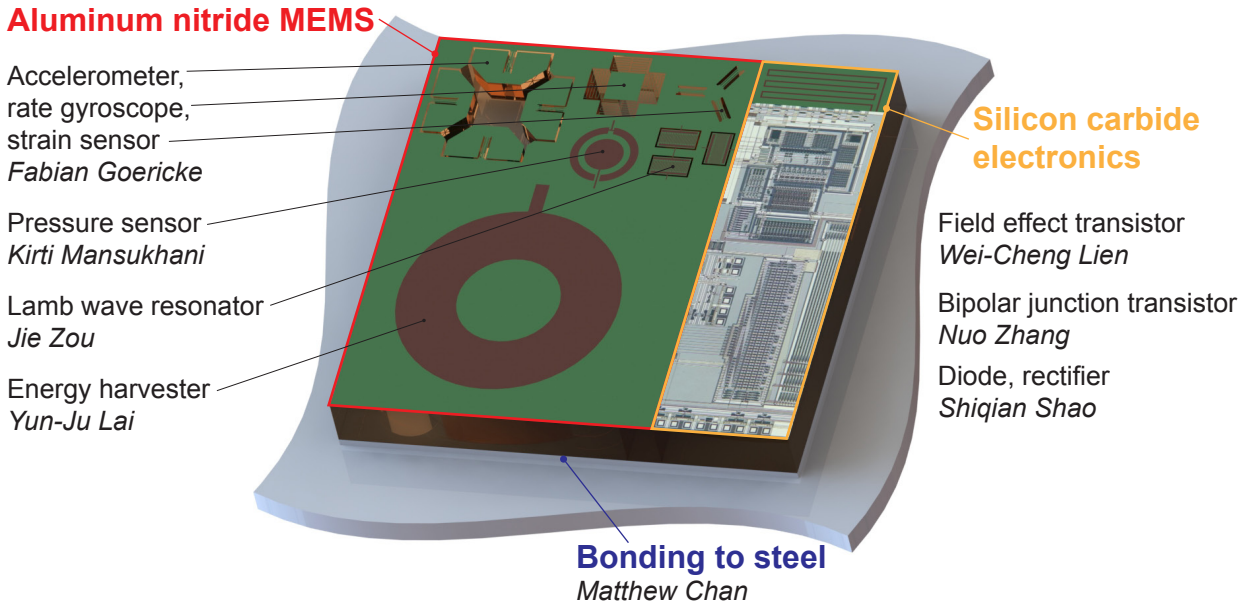

Figure 1.1. Schematic drawing of the envisioned fully integrated harsh environment sensing system. Individual components are labeled with the name of the current researcher at BMAD.

(MEMS) portion of the sensing system because of its unique properties. It can be sputter deposited

efficiently with good control of film quality and residual stress. It is piezoelectric and maintains this property until at least 1000 °C. A thin protective oxide layer forms in an oxidizing environment at elevated temperature and protects the material up to at least 1000 °C before bulk oxidation occurs. AlN has a high melting point of 2470 °C and maintains most of its mechanical strength up to very high temperatures. Silicon carbide (SiC) is the second material chosen for the sensing system as its properties complement those of AlN. It does not melt and has a very high sublimation point of 2830 °C. Like AlN, SiC is a hard and strong ceramic material even at elevated temperatures. It does not possess piezoelectric properties and its micromachining processes are more challanging than those of AlN. However, due to its lower bandgap around 3.2 eV it can be doped and turned into n-type and p-type regions similar to silicon. As a result, electronic components such as diodes and transistors can be made out of SiC and those components have been shown to operate at 600 °C [1].

1.1 MEMS market

MEMSs have become an important and rapidly growing field in engineering. The total market value for MEMS surpassed 10 billion US$ for the first time in 2011 and it is expected to continue growing at a rate of about 13 %[1]. Over 50 % of the MEMS market is made up of sensors. Inertial sensors (accelerometers and gyroscopes) make up more than one quarter of the market due to their widespread application in the automotive and consumer electronics fields. In automobiles, gyroscopes are mainly used for electronic stability control (ESC) and accelerometers to sense deceleration in accidents to control the deployment of airbags. In consumer electronics, both accelerometers and gyroscopes are used for user motion sensing, e.g., in smart phones and video game controllers. Due to the increasing accuracy of the sensors an emerging market is navigation without global positioning system (GPS) by use of MEMS inertial measurement units (IMUs), which are made up of 3-axis accelerometer, 3-axis gyroscope and typically also a 3-axis magnetometer.

Current trends in MEMS are driven by the ever growing desire for data that can be generated by better, cheaper and smaller sensors. The *Internet of Things* is a popular term for the vision that every piece of technology is wirelessly connected to contribute to and benefit from a globally generated pool of data. The *Trillion Sensors* movement led by Silicon Valley MEMS visionary Janusz Bryzek is projecting that a trillion MEMS sensors will have shipped by 2022 and is working on a roadmap to guide and accelerate the required growth in the industry towards this goal [3]. It is the hope that exponential growth can create a powerful enough sensor network to help bridge the gap between global need for goods and services and the capability to produce them and thus help solve global problems such as food or water shortage[2].

AlN is commercially used as a material for resonating devices, such as frequency references, filters and duplexers. Film bulk acoustic resonators (FBARs) are a particular success story for AlN and played a big role in the miniturization and evolution of modern cellular phones [5]. Harsh environment sensors are still a niche market due to the problems with power generation and storage,

[1] The data in this section was taken from a presentation by Jeff Perkins [2].

[2] This concept is described in the chapter *Exponential Technologies* in the book *Abundance* [4].

wireless communication and signal processing at high temperature. AlN has the potential to solve the problem of generating a usable sense signal for a variety of sensing applications. Furthermore, AlN could eventually find its way into mainstream sensing applications due to its integrability with CMOS technology [6], the ability to combine sensors and resonators in one chip and potentially performance improvements compared to existing technology. It is the author's hope that the content of this dissertation will be a significant contribution to move AlN closer to sensor commercialization for both harsh environment and conventional sensing applications.

1.2 Previous work

The field of harsh environment sensing applications is very broad and as a result different technologies are being developed for different sets of operating parameters. Harsh environments include exposure to high *g*-shock, high pressure and corrosive substances. The latter two challenges are almost entirely dealt with by the design and material choice of the primary or secondary package, which represents the boundary between the MEMS chip and the surrounding environment. However, high *g*-shock survivability requires the entire sensing system to be designed accordingly because this mechanical load cannot be shielded by a package. The most frequently cited and most important property for harsh environment sensing systems is high temperature survivability. Depending on the application the tempature that the sensor is exposed to could be anywhere from 200 to 800 °C or for some applications even higher. Example applications and their temperature demands are listed in Table 1.1. Today, the electronics are often placed outside of the hot environment and the sensors are interrogated using optical methods. An example would be an optically actuated and sensed MEMS membrane for pressure measurements in the high temperature environment of a geothermal well [11]. When it is not possible to separate the electronics and the sensing element SiC is the most commonly used material for both the electronics [12, 13] and the sensors [14, 15, 16].

Table 1.1. Examples of high temperature environments for sensing applications.

Category	Application/Location	Temperature (°C)
Automotive [7]	combustion pressure based engine control	200-450
	diesel engine control, preak pressure control	200-450
	mass flow sensor for exhaust gas remission	200-300
	fast exhaust gas sensors	850
Geothermal energy [8, 9]	conventional geothermal wells	up to 380
	unconventional, deep geothermal wells	up to 600
Gas turbine [10]	compressor	400-465
	combustion zone	1370-1427
	turbine exhaust	482-638

AlN MEMS sensors are currently not commercially produced in significant numbers because of the early state of the technology development compared to established technologies, especially

based on silicon. However, the need for ongoing miniaturization for the mobile electronic device market could make AlN an attractive option in the future because it can be combined on a chip with complementary metal-oxide-semiconductor (CMOS) electronics and resonator devices. Prior to this dissertation research, accelerometers have been developed at BMAD that use a thin film of AlN as structural and piezoelectrically active material [17]. Other groups have used AlN, e.g., for gravimetric sensors [18, 19], microphones [20], magnetic field detectors [21], range finders [22] and pressure sensors [23, 24].

1.3 Dissertation structure

Chapter 2 talks about some detailed findings in the development of optimized AlN deposition processes. Chapter 3 discusses the fabrication processes developed in this doctoral research to make the AlN sensors. In Chapter 4, double-ended tuning forks and triple-beam tuning forks are discussed as sensing elements for strain and acceleration. Chapter 5 explains how the same fabrication process is used to make rate gyroscopes. Testing of the sensors at high temperatures is presented in Chapter 6 and concluding remarks and recommendations for future work can be found in Chapter 7.

Chapter 2

Aluminum Nitride Deposition

Conventional direct current (DC) sputtering from a single conductive target is an established technique for the deposition of thin films. However, the deposition of aluminum nitride (AlN) with good crystal orientation and stress control requires some advanced sputtering techniques. In this chapter, work on optimizing the AlN films produced in the Marvell Nanofabrication Laboratory is presented. Section 2.1 gives an overview of the material properties of AlN and its technical applications. In Section 2.2, the deposition of thin AlN films via reactive alternating current (AC) magnetron sputtering is explained. Sections 2.3 and 2.4 discuss research results of this doctoral work in the characterization of AlN films and the optimization of those films, respectively.

2.1 Properties of aluminum nitride

AlN is a truly remarkable engineering material with a unique set of properties. Although it is a wide bandgap semiconductor and very good electrical insulator, AlN has a very high thermal conductivity. Its melting point is high and due to a protective surface oxide, it does not degrade in oxidizing atmospheres (e.g., air) up to 1077 °C [25]. In reducing atmospheres (e.g., pure nitrogen), the usable temperature is at least as high because, unlike other micro-electromechanical system (MEMS) materials that are based on oxides of elements, AlN is a nitride and cannot be reduced. Finally, AlN has significant piezoelectric properties, which enables it to be used as the active MEMS material for all of the devices presented in this dissertation. Bulk AlN can be made as a single crystal or in polycrystalline form. AlN used for MEMS applications is usually deposited as a polycrystalline thin film with a specific crystal orientation, but it can also be deposited epitaxially as a single crystalline layer. Some of the most important properties of AlN are compared to three other materials in Table 2.1. Silicon is listed because it is the conventional material for electronic components and MEMS sensors. A comparison of the material properties of silicon and AlN at high temperature can be found in Section 6.1. Silicon carbide (SiC) is listed because it is

the preferred material for high temperature electronics as explained in Chapter 1. Molybdenum is also mentioned because it is the preferred material for electrical connections in combination with AlN as described in Chapter 3. AlN, 4H-SiC and molybdenum can be used up to at least 600 °C. Furthermore, their coefficients of thermal expansion (CTEs) are closely matched, which is advantageous in order to minimize the thermal mismatch stresses when using them together over a wide temperature range.

Table 2.1. Properties of aluminum nitride compared to silicon, 4H-silicon carbide and molybdenum

Property	Unit	Silicon	4H-Silicon carbide	Aluminum nitride	Molybdenum
Melting point	°C	1420	2830 (sublimes)	2470	2623
Bandgap	eV	1.12	3.2	6.2	N/A (metal)
Applications		circuits, sensors	circuits	sensors	connections
Maximum temperature	°C	350	650	>1000	600
Failure mechanism		thermal carriers, softening	ohmic contacts problem	bulk oxidation	bulk oxidation
Thermal conductivity	W/m-K	149	490	1.83-319*	138
Young's modulus	GPa	190	450	340	329
Coefficient of thermal expansion	10^{-6}/K	2.6	4.5	4.0	4.8

*: 319 (bulk, single crystalline, along c-axis) [26], 9.6-25.2 (1 μm film, single crystalline) [27], 1.83/76.5 (200 nm/2 μm film, polycrystalline) [28]

2.2 Reactive sputtering of aluminum nitride films

The different deposition methods that can be used to deposit thin film AlN include chemical vapor deposition, molecular beam epitaxy, reactive evaporation, reactive ion beam deposition and reactive sputtering. For industrial implementation of any fabrication process, the deposition rate has to be high enough to be economically feasible. If the aluminum nitride devices are supposed to be post-complementary metal-oxide-semiconductor (CMOS) fabricated, i.e. created on top of previously made CMOS layers, the deposition temperature has to be low enough to leave the CMOS unharmed. 400 °C is generally considered to be the highest temperature that can be tolerated by unpackaged CMOS wafers. The crystal structure of the AlN film is important because it determines its piezoelectric properties. Single crystallinity is not necessary for most applications, but a very good alignment of the c-axis normal to the substrate plane is required to achieve significant piezoelectric properties within the plane. Finally, control of both the overall film stress and the film stress gradient can be critical for released MEMS structures. This issue is discussed in more detail

in Section 2.4. Reactive AC magnetron sputtering has become the preferred method for thin-film AlN deposition in industry because of the favorable combination of high deposition rate, low deposition temperature, good crystal structure and superior stress control. The Marvell Nanofabrication Laboratory is using a state of the art *Endeavor AT* multi-chamber sputtering tool manufactured by *Tegal Corporation*'s plasma tool branch, which has been bought up by *OEM Group, Inc.* A cross-sectional schematic of the tool's AlN deposition chamber is shown in Fig. 2.1[1]. Two conical

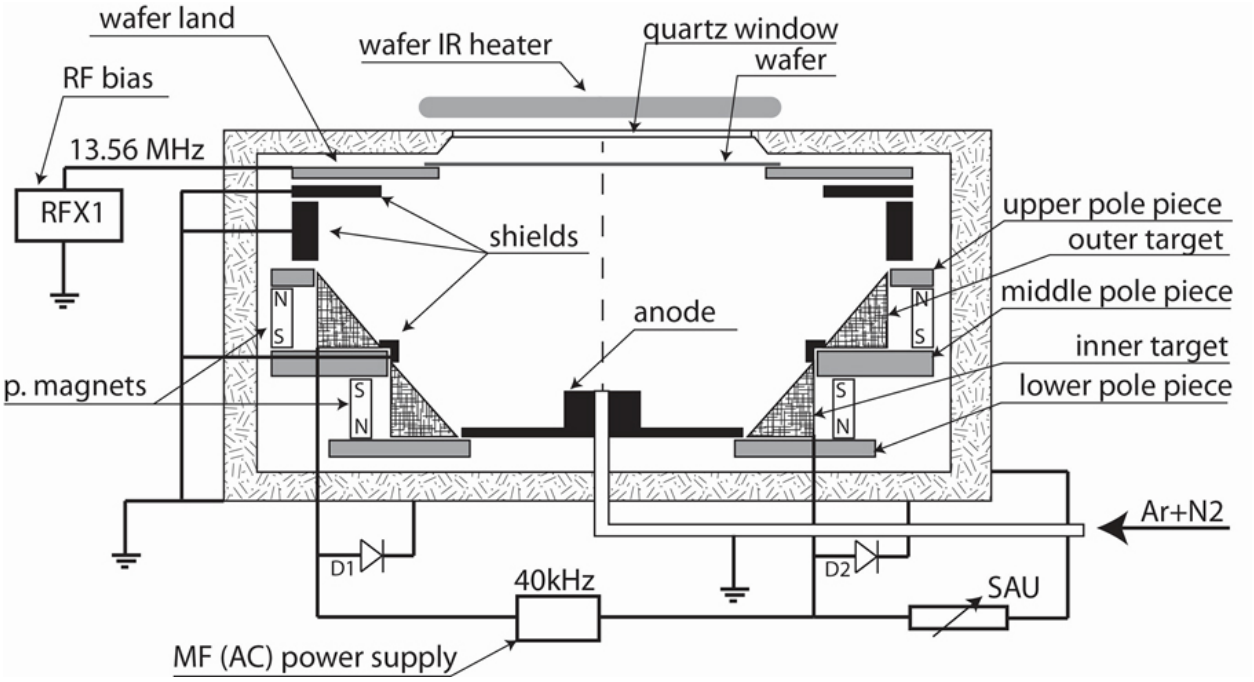

Figure 2.1. Schematic view of deposition chamber for reactive sputtering of aluminum nitride films.

aluminum targets are placed concentrically underneath the wafer, which rests on a wafer land with the device side facing down. In conventional DC sputtering, inert gas ions are accelerated toward the target, which is kept at the low potential thus forming the cathode. Atoms are knocked out of the target via momentum transfer and get deposited on the substrate. In the Endeavor sputtering tool, an AC power supply is used to alternately turn each target into the cathode at a frequency of 40 kHz. The material is then deposited in a sputter-up process onto the substrate. This configuration of dual cathodes is commonly known as S-gun. Permanent magnets are placed around the targets to create magnetic fields above the target surfaces. The magnetic fields capture electrons and thus increase the plasma density close to the target, which consequently increases the sputtering rate. This usage of magnetic fields to improve the process is called magnetron sputtering. The most important aspect of this deposition method for AlN is the addition of nitrogen to the argon in the chamber. The added nitrogen reacts with the aluminum ions and forms the desired stoichiometric AlN on the wafer substrate giving the process the name reactive sputtering. Photographs of the deposition tool are shown in Fig. 2.2. The wafers are loaded into the tool using a gate chamber called cassette module (CM), which can be vented to atmospheric pressure. Upon pumping the

[1]This figure is reproduced with permission from [29] and based on a figure in [30].

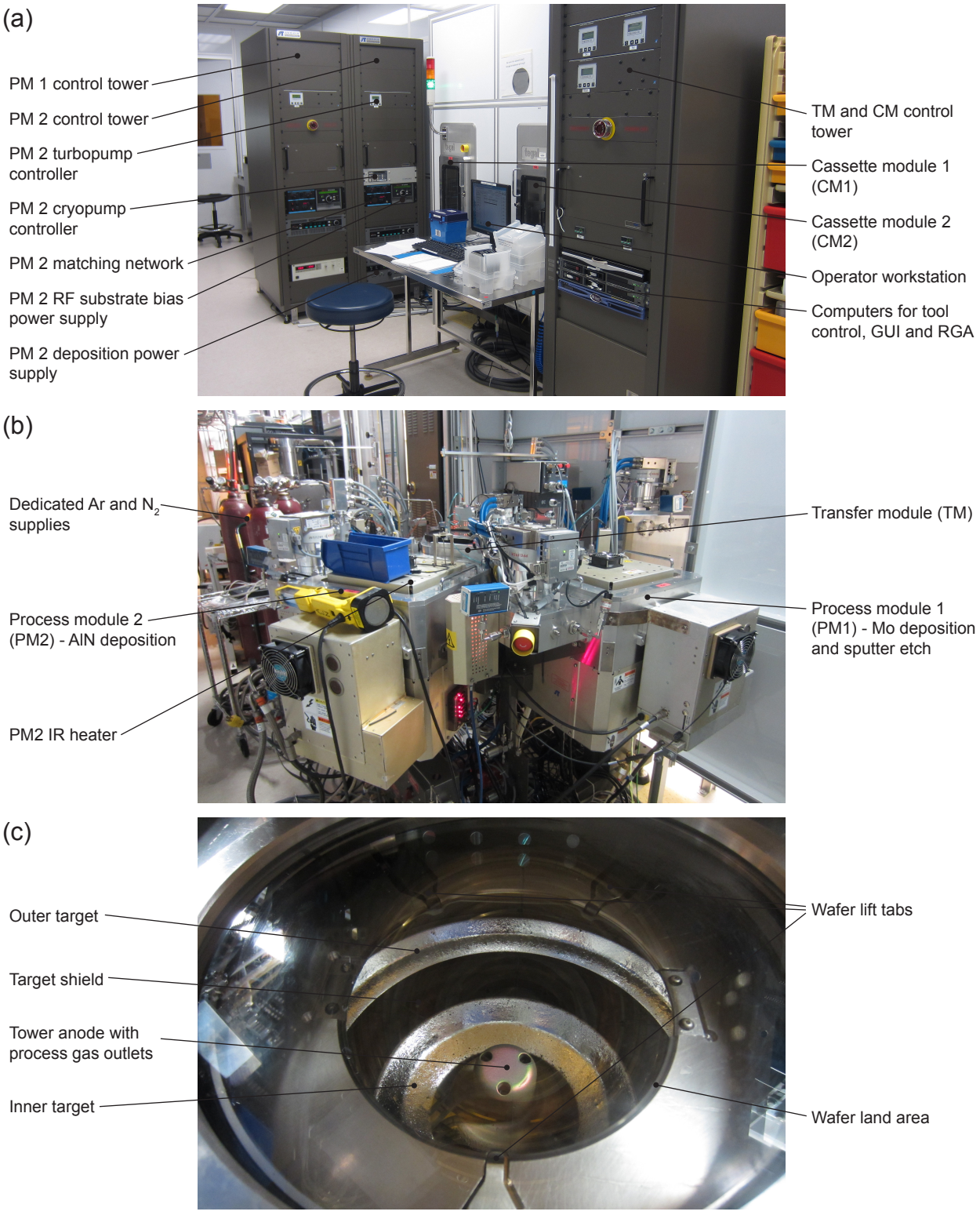

Figure 2.2. Photographs of the Tegal Endeavor tool for AlN and molybdenum deposition. (a): Operator side (front side). (b): Process and transfer modules (back side). (c): Inside of process module 2.

CM to vacuum the wafers are transferred into the individual deposition chambers called process modules (PMs) using a ceramic endeffector connected to a wafer handling robot inside the centrally located transfer module (TM), which connects the CMs and PMs. Each module has its own turbo pump and PMs 2 and 3 also have cryopumps to achieve lower base pressures. Each PM has its own control tower. The tower for PM 2 contains the controllers for turbopump and cryopump, the power supply for radio frequency (RF) substrate bias and the according capacitive matching network controller and the AC power supply that supplies the deposition power to the targets. The stress adjustment unit (SAU) is also housed in the tower but not shown in the picture. The tool has its own supply of the process gases argon and nitrogen to avoid the risk of contamination that would be present if the house supplies of those gases were used. The AlN film quality is especially negatively impacted by any trace amount of oxygen in the process gases. The inside of PM 2 is shown in Fig. 2.2c. The wafer is moved into the chamber by the robot and picked up from the endeffector and lowered onto the wafer land area by the wafer lift tabs. The wafer rests on a very narrow rim during the deposition process so that almost the entire wafer surface (up to about 1 mm from the edge) gets coated. The outer and inner targets shown in the figure have about 50 % of their usable life remaining because a racetrack shaped valley is clearly visible but only a few mm deep.

2.3 Aluminum nitride characterization

The three measurements of importance to determine the quality of an AlN film are film thickness measurement, x-ray diffraction (XRD) rocking curve measurement for crystal quality and measurement of the residual film stress. The following sections discuss some important details of the individual procedures and their implications for AlN.

2.3.1 Thickness measurement

The AlN film thickness can be reliably measured using the Nanolab's *Nanospec* film thickness measurement system (Fig. 2.3a). The tool compares incident light to the wafer surface to the light reflected from it and uses mathematical algorithms to determine the film thickness based on the shift in the interference spectra. This method works for AlN films on bare silicon wafers and on top of molybdenum layers. For this dissertation a measure for the film non-uniformity is defined by:

$$\text{non-uniformity} = \frac{t_{max} - t_{min}}{(t_{max} + t_{min})/2} \tag{2.1}$$

Where t_{max} and t_{min} are the maximum and minimum of the measured film thickness, respectively. A non-uniformity of zero would be a perfectly uniform film with the same thickness everywhere on the wafer. Typical thickness non-uniformity for the deposited AlN films is about 2 %. In order to get comparable numbers for each 15 cm-wafer the thickness is always measured in the same nine locations as shown in Fig. 2.3b.

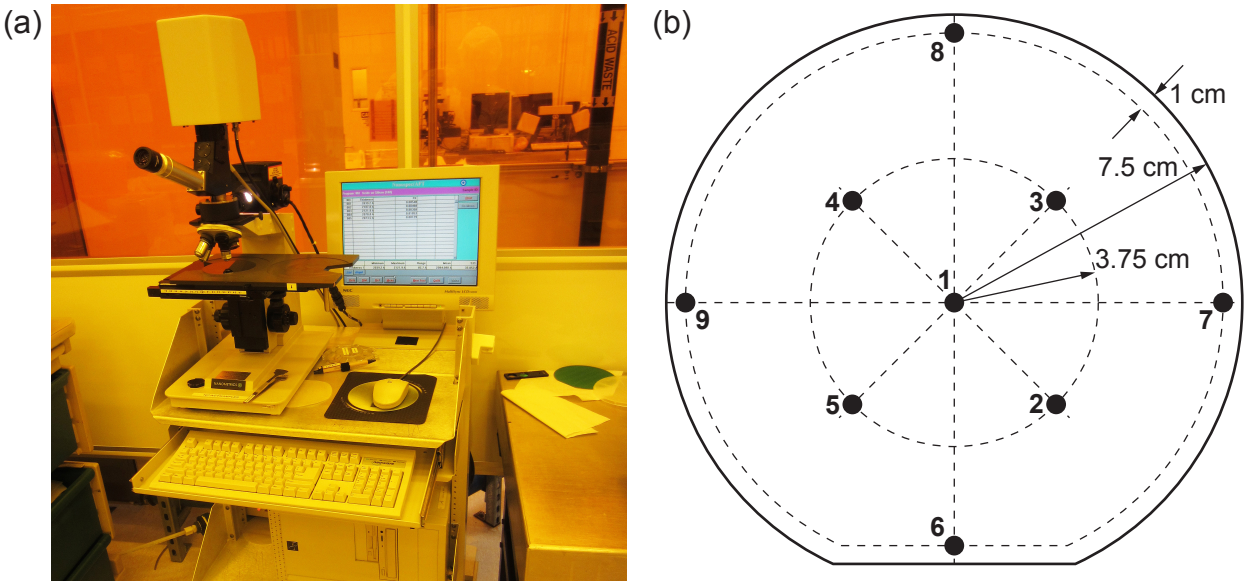

Figure 2.3. (a): Photograph of the Nanolab's Nanospec film thickness measurement system. (b): Schematic of measurement locations for film thickness (black dots) on 15 cm-wafer.

2.3.2 Rocking curve measurement

The AlN films deposited in this research are polycrystalline and have a wurzite crystal structure. The c-axis is oriented in the normal direction to the wafer. X-ray diffractometry can be used to determine the degree of this orientation by means of a rocking curve measurement. The measurement setup is schematically shown in Fig. 2.4a. The angle 2θ between x-ray source and

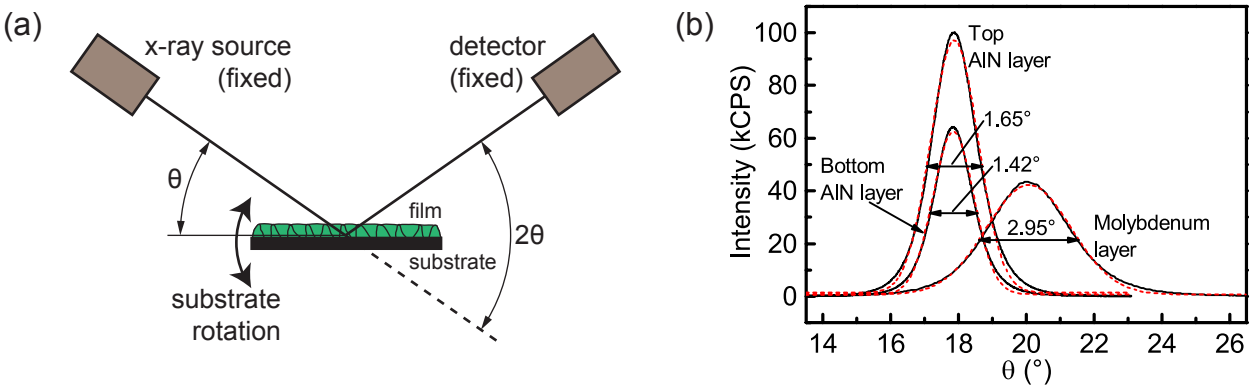

Figure 2.4. (a): Schematic of the measurement setup for XRD rocking curve measurement to determine AlN crystal orientation. (b): Rocking curves of three film layers deposited on a silicon wafer (black solid lines) and Gaussian fit curves (red dashed lines) for the calculation of the FWHM.

detector is fixed at the material dependent position of the expected diffraction peak. The angle θ of the substrate with respect to the incident beam is varied. For an ideal crystal diffraction would only occur when $\theta = \frac{(2\theta)}{2}$. However, for any real crystal the diffraction intensity is normal distributed

around the peak position and the width of the bell curve is an indication of the crystal quality. As in most published work, the full width at half maximum (FWHM) is used as the measure of crystal quality in this dissertation. Figure 2.4b shows a FWHM of 1.42° for the first (bottom) AlN layer of 1 µm thickness deposited on a silicon wafer. The rocking curve of a molybdenum layer is also shown in the figure and it can be seen that the metal also has a preferential crystal orientation when deposited on AlN under the right conditions. This crystallinity is important for the quality of the subsequently deposited 1 µm AlN layer. The rocking curve of this top AlN layer with a FWHM of 1.65° is also shown. For this curve the intensity of the XRD signal is stronger because it is now measuring the combination of first and second layer but the FWHM is worse because AlN deposition on metals generally results in a worse crystal orientation than on a blank silicon wafer.

2.3.3 Film stress measurement

The AlN film stress is a critical parameter for the performance of released MEMS devices. Assuming uniform stress distribution on the whole wafer, the film stress can be calculated from the change in wafer curvature caused by the deposition of the film. If the wafer becomes more concave (bowl-shaped) as viewed from the AlN film side the film stress is tensile and if the wafer becomes more convex (dome-shaped) the film stress is compressive. The Nanolab's *Tencor FLX-2320* (Flexus) thin film stress measurement system uses the reflection of a laser beam to determine the curvature along a line across the wafer. The system automatically calculates the film stress σ_f using the following equation:

$$\sigma_f = \frac{E t_s^2}{6 t_f} \left(\frac{1}{R_1} - \frac{1}{R_0} \right) \tag{2.2}$$

Where E is the biaxial elastic modulus of the substrate (for silicon: $E = 180.5$ GPa), t_s is the substrate thickness, t_f is the film thickness, R_0 is the radius of curvature before the film deposition and R_1 is the radius of curvature after the film deposition. By definition a positive radius of curvature means a concave wafer shape as viewed from the film side and a negative radius of curvature means a convex wafer shape. For this dissertation, the film stress is always determined by measuring the curvature at 0° and at 90° with respect to the wafer flat and averaging the resulting film stress values.

Another method to measure the AlN film stress using the x-ray diffraction data was investigated in this doctoral research. It is based on the fact that the peak position of a rocking curve measurement is related to the crystal spacing, which depends on the intrinsic stress in the film. Therefore, it was speculated that a relationship between the peak position and the film stress could be found. AlN films with a wide variety of film stresses were deposited and the x-ray diffraction peak positions were determined in the standard rocking curve measurement. Three examples of rocking curve results are shown in Fig. 2.5a. The relationship between peak position and film stress for the entire data set is shown in Fig. 2.5b. The results clearly show that the angle of the peak position increases with increasing film stress. The presented data is not very accurate in predicting the stress level, but if the method could be improved in the future it would have great potential especially for local stress mapping of the entire wafer. One improvement that would result in a

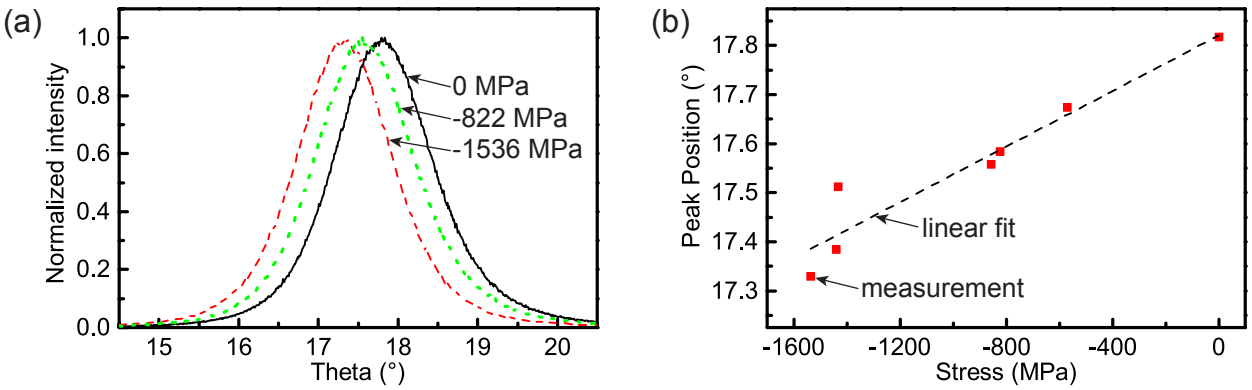

Figure 2.5. (a): Rocking curve data for three different film stress levels in AlN. (b): Relationship between peak position and film stress level for entire data set.

more accurate measurement would be the replacement of the collimator at the x-ray source with a monochrometer [31].

2.4 Sputtering parameter optimization

In principle, it is possible to deposit very high quality AlN films with great control of the residual stress in the Nanolab's Endeavor tool. However, the state of the tool is highly variable and changes with each deposited film due to aging and potential contamination of the targets and the inside of the chamber (most notably the replaceable shielding between the targets). Therefore, before each critical deposition on process wafers, several test runs are required in order to dial in the process parameters. When the tool is operating well, a typical FWHM of the XRD rocking curve of 1.4° for a 1 µm film on a blank silicon wafer can be achieved. A significantly higher value indicates malfunction of the tool. Within wide limits the rocking curve is not a strong function of the residual stress and thus not a strong function of the variable deposition parameters power, argon flow, nitrogen flow, RF substrate bias and resistance of the SAU. All of those parameter have a major effect on the residual film stress and some of them also affect the film thickness uniformity. An investigation into the effect of the process parameters can show trends for the resulting film parameters, which can be useful for process correction in future runs. But due to the short-, medium- and long-term variability of the tool no standard process can be defined that will always yield satisfying results. In the following subsections, the trends found by the author in several hundred film depositions are explained in detail.

2.4.1 First wafer effect

It was consistently observed that the first wafer of any deposition run would have slightly different AlN film properties than the remaining wafers of the same run. Figure 2.6 shows the

trend in FWHM of the rocking curve, deposition rate, thickness non-uniformity and film stress for four wafer runs with three wafers each. All films are about 1 μm thick, but different deposition

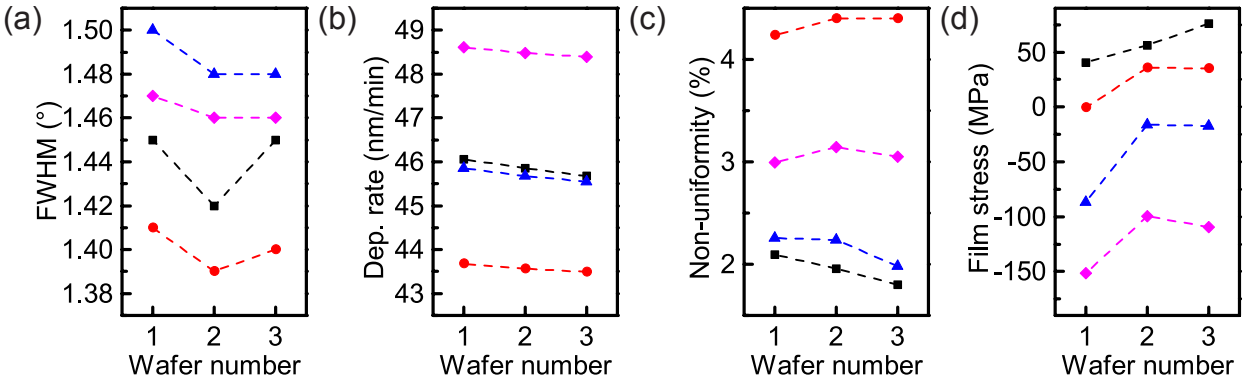

Figure 2.6. Trend of (a) rocking curve FWHM, (b) deposition rate, (c) thickness non-uniformity and (d) film stress for the first three wafers of four different AlN deposition runs. Red circles: Run 1, magenta diamonds: Run 2, black squares: Run 3, blue triangles: Run 4.

recipes were used for each run so that the parameters' absolute values are not comparable. It can be seen that there is no clear correlation between the wafer number in the run and either the the rocking curve FWHM or the thickness uniformity, which indicates that the film quality is not affected by a first wafer effect. The deposition rate decreases monotonically between any two depositions, which is also not a first wafer effect but the result of increasing distance between the target and wafer surfaces as the target gets used up. The film stress, however, shows a clear first wafer effect. For all four runs, it is significantly lower for the first wafer and for all but Run 3 it is nearly identical for the second and third wafer. The deposited films are on average 44.7 MPa more compressive for the first wafer of a run than for the remaining wafers (range: 25.8 to 69.9 MPa). It was found that the best way to compensate for this effect without having to discard the first wafer is to use a different deposition recipe for the first wafer than for the remaining wafers. The nitrogen flow rate was generally used to adjust the stress as explained in the next section. The origin of the first wafer effect was not definitively determined. It is thought that the deposition chamber temperature equilibrates after the first wafer, but this hypothesis is not supported by the fact that experiments with active heating using the infrared (IR) heater during the depositions did not alleviate the first wafer effect.

2.4.2 Effect of gas flow rates

The partial pressures of the process gases argon and nitrogen is determined by the gas flows (and the constant pump speed) since there is no active pressure control mechanism in the tool. The general trend in sputtering processes is that film stress becomes more compressive with decreasing deposition pressure because compaction in the forming film occurs due to higher energetic bom-

bardment[2]. Due to the continuously changing machine condition (and the many problems with machine downtime) it is difficult to get statistically significant, quantitative data on the pressure dependence of film parameters. The general trends can be seen in Fig. 2.7, which shows the results of three deposition runs performed consecutively within the same day. As for the studies

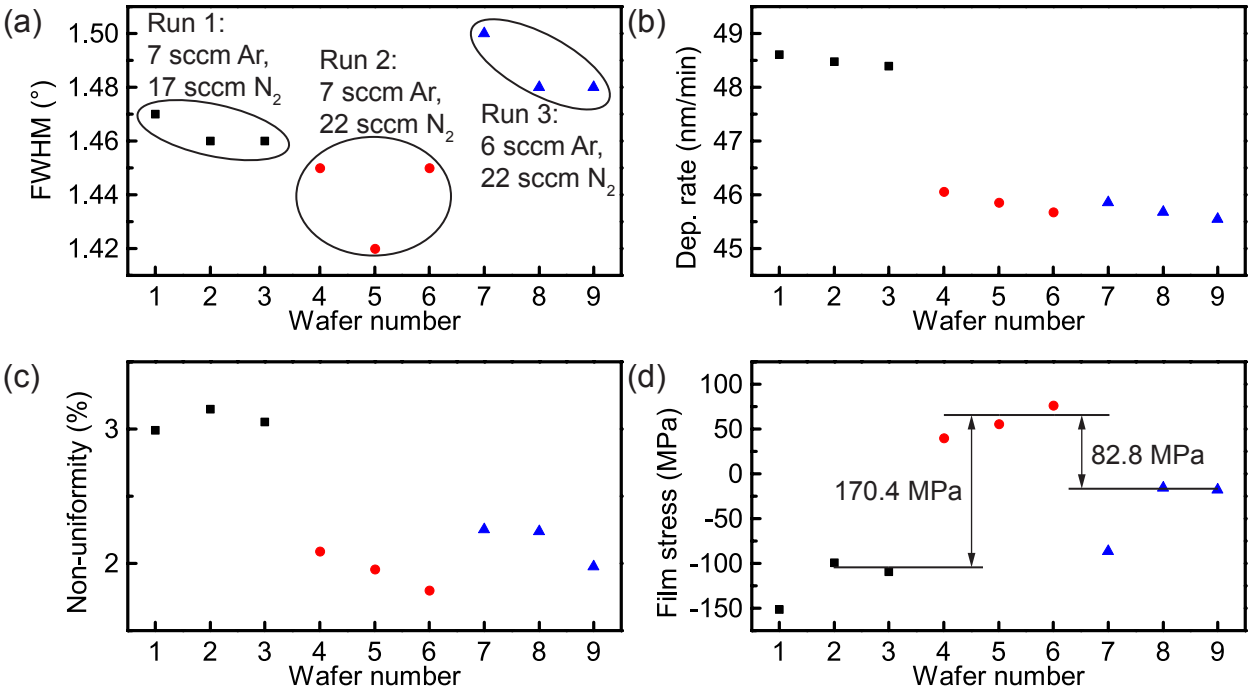

Figure 2.7. Trend of (a) rocking curve FWHM, (b) deposition rate, (c) thickness non-uniformity and (d) film stress for all three wafers of three different AlN deposition runs with different gas flow rates.

on the first wafer effect the standard film of about 1 μm thickness on a bare silicon wafer was deposited in each case. It can be seen that the FWHM is not a strong function of the flow rates. Both the deposition rate and the non-uniformity are inversely related to the deposition pressure, but the variations are small and all recipes give acceptable results. The most important parameter is the film stress, which can greatly affect the performance of MEMS devices and must therefore be controlled precisely. The deposition recipe used for Run 2 has become the standard recipe for AlN deposition because it results in near zero stress for a 1 μm film on bare silicon wafers during much of the life of the sputtering targets. The recipe uses an argon flow rate of 7 sccm and a nitrogen flow rate of 22 sccm. The deviation of the film stress for the cases of reduced nitrogen and argon flow rates are shown in Fig. 2.7d. For small changes in the flow rates the behavior is linear and the sensitivity is 82.8 MPa per sccm of argon and 34.1 MPa per sccm of nitrogen. These values are a good first guess for the process modifications that have to be made if a film with non-zero stress is required or if a zero-stress film is required on top of materials that typically make the AlN film more compressive, e.g., metals or tensile, e.g., silicon dioxide (SiO_2).

[2]There is a turnover pressure above which the stress also becomes compressive with increasing pressure due to other effects, e.g., the increase in the particles' kinetic energy [32].

2.4.3 Effect of RF substrate bias and SAU

The AlN deposition tool has two additional ways to control the film stress. An RF bias voltage can be applied to the substrate to increase the energy of impinging particles and thus achieve a compacting effect that makes the stress more compressive similar to reducing the deposition pressure. In most cases, it is not necessary to use additional methods to decrease the film stress past the capability of reduced nitrogen flow rate. In fact, the problem of films becoming too compressive is much more prevalent, especially when the sputtering target is nearing the end of its useful life. Limited experiments have been performed to test the capabilities of the substrate RF bias and it was observed that the stress in a 2 μm film is reduced by 73 MPa when a 30 W bias is applied. The SAU is another option to modify stress levels and it is specifically designed to reduce the compressive film stresses resulting from an aging sputtering target. The operating principle is based on providing an alternative current path for cold electrons near the substrate surface and thus reducing the amount of ion impingement[3]. It was found that the same process recipe results in a 1 μm film that is 470 MPa more tensile when the SAU is connected and set to 15 Ω compared to the case when the SAU is disconnected.

2.4.4 Film stress gradients

It can often be observed that MEMS devices consisting of sputter deposited AlN films experience significant curving during the final release step even if the film stress was measured to be close to zero. It has been suspected that film stress gradients resulting from the deposition process are the cause of this unwanted behavior. As part of this dissertation research three different methods to determine the stress gradients in sputter deposited AlN films have been investigated. In one method, a 2.5 μm thick film is deposited on a bare silicon wafer and then etched back incrementally until it is completely removed. After each etching step the curvature of the wafer and the remaining film thickness are measured. By comparing the curvature to the previous value the film stress in the removed layer can be determined using Eq. (2.2). Wet etching methods, e.g., using heated phosphoric acid as described in Chapter 3, are not suitable for this experiment as they attack the polycrystalline AlN preferentially along the grain boundaries and therefore cannot remove a uniform layer of a defined thickness. Therefore, it was investigated if a dry-etching process as described in detail in Appendix A could be used for this purpose. The etching was performed in steps of 45 or 22.5 seconds each with the goal of removing 2000 or 1000 Å per step, respectively. The remaining film thickness and the non-uniformity as defined in Eq. (2.1) after each etching step are plotted in Fig. 2.8a. It can be seen that the etch rate is constant throughout the film thickness. However, the film is etched much faster in some areas of the wafer with the non-uniformity exceeding 50 % when about 3000 Å of the film are remaining. This non-uniformity is expected to have a negative effect on the accuracy of the film stress measurement. The stress for each portion of the film is plotted over the distance of that portion's center from the AlN/silicon interface in Fig. 2.8b. The data shows that the film stress is compressive at the beginning of the deposition process and becomes progressively more tensile. However, the data has too much uncertainty for a

[3]The physics of the SAU are quite complicated and best explained by the inventors of the technology [33].

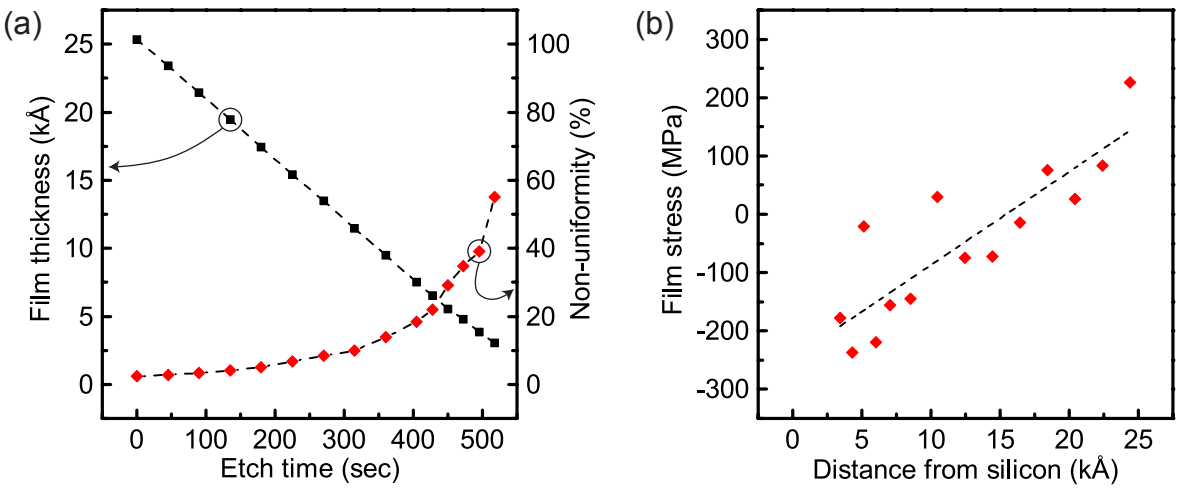

Figure 2.8. Results of AlN film stress gradient measurement by incremental layer removal. (a): Film thickness and non-uniformity after over etch time, (b): film stress of the layers determined from the wafer curvature before and after each etching step.

quantitative analysis, which is thought to be caused by the uneven film removal during the etching process.

Instead of depositing the entire film first and incrementally etching it back to determine the film stress gradient it was also attempted to incrementally grow the film, remove the wafer from the deposition tool after each deposition step and determine the stress from the change of curvature. The advantage of this method is that the film can be grown very uniformly for each step. The disadvantage is that the deposition has to be interrupted and the wafer exposed to air between the steps and thus potentially change the film growth dynamics. Twelve deposition steps were performed with a recipe that would yield a near zero stress film if deposited continuously for a thickness of 1 μm. In each step, AlN was deposited for 100 seconds for a target layer thickness of 1000 Å each. The film thickness and non-uniformity over deposition time are shown in Fig. 2.9a. It can be seen that unlike in the etching method the non-uniformity does not increase over time. Thus, it can be concluded that the stress measurements represent the accurate values. Due to the controlled nature of the sputtering process the deposition rate is very constant for all steps. The stress in each deposited layer is plotted over the distance of that layer's center from the AlN/silicon interface in Fig. 2.9b. The same trend as for the etching method can be observed. Initially, the deposited film is very compressive and each additional layer becomes more tensile. The gradient seems to be steeper in the beginning and flattening out with growing film thickness. The plotted fit line, which gives the best fit for the data, is of the function type $A - B \times \exp(t/C)$, where A, B and C are positive numbers and t is the film thickness.

The deposition-based method of determining the film stress gradient gives better results than the etching-based method. However, it is not clear how much the results are affected by the removal of the wafer from the tool and exposure to air between the deposition of the AlN layers. Therefore, a third method was developed to overcome this problem. Here, the AlN deposition is performed with the same deposition recipe for different lengths of time on separate wafers and the film stress is determined for each layer. Then, assuming that the first part of a thicker film is identical to the

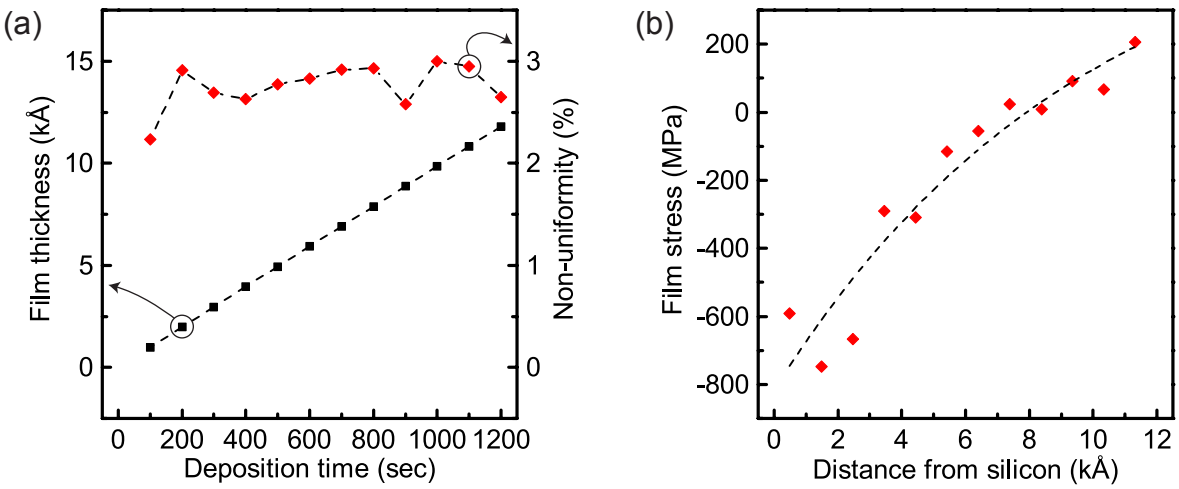

Figure 2.9. Results of AlN film stress gradient measurement by incremental layer deposition. (a): Film thickness and non-uniformity after over deposition time, (b): film stress of the layers determined from the wafer curvature before and after each deposition step.

thinner film, the stress in the added film thickness $\sigma_{n,n-1}$ can be calculated:

$$\sigma_{n,n-1} = \frac{\sigma_n t_n - \sigma_{n-1} t_{n-1}}{t_n - t_{n-1}} \tag{2.3}$$

Where σ_n and σ_{n-1} are the stresses in the AlN layers of wafers n and $n-1$, respectively, and t_n and t_{n-1} are the according AlN film thicknesses, respectively (see Fig. 2.10a). The overall measured

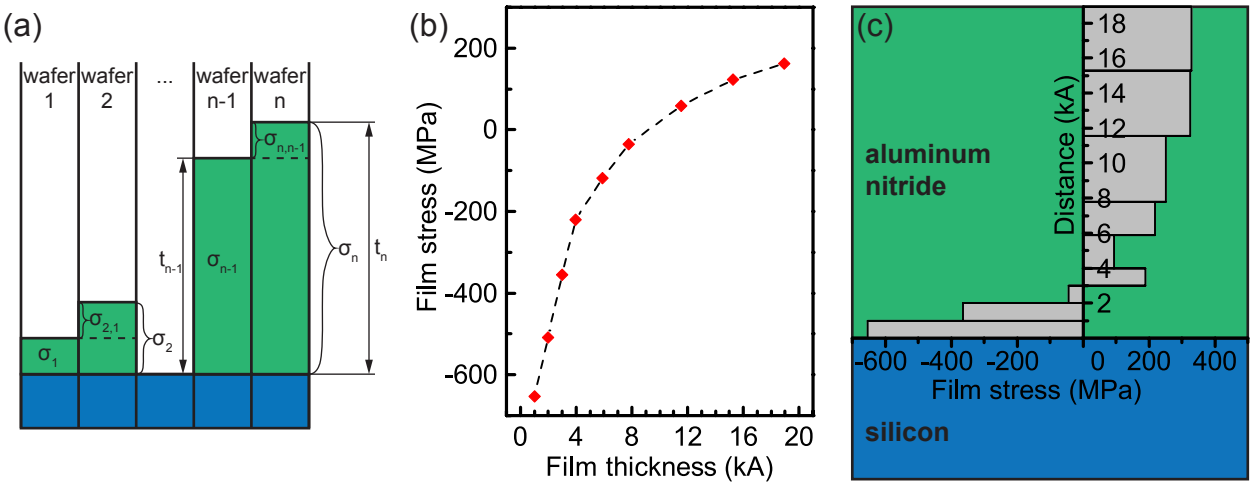

Figure 2.10. Results of AlN film stress gradient measurement by layer deposition on multiple wafers. (a): Definition of the film stresses and thicknesses in the wafers, (b): film stress over film thickness, (c): extracted film stress in the layers of a continuously deposited AlN film.

AlN film stress for each wafer is plotted over the overall film thickness in Fig. 2.10b. The resulting film stress in different layers of a 1.9 µm AlN layer can be extracted from this data and is shown in Fig. 2.10c. This result is expected to represent the true film stress gradient most accurately of

the three methods presented in this work. Several conclusions can be drawn from the data. The AlN film grows with high compressive stress at first and has a steep gradient for about 3000 Å. Any added film after about 1 μm of growth has an almost constant film stress. From this data, it is possible to predict the required deposition recipes if different thicknesses of near zero stress films are desired. Furthermore, it could be possible to develop deposition flows that consist of several recipes with different deposition parameters to compensate the stress during different times of the deposition. This process flow would be able to not only achieve a zero total stress film, but also minimize the stress gradient throughout the film thickness. One recommendation for future work would be to split the process flow up into three portions for the first 3000 Å of deposition, for the thickness between 3000 Å and 1 μm and for any added deposition beyond 1 μm. The effect of a metal bottom electrode or a SiO_2 layer on the film stress gradient would be another important aspect for future studies.

Chapter 3

Fabrication Processes

Micro-electromechanical system (MEMS) microfabrication processes were originally derived from the same technologies used for the fabrication of microelectronics. Many of the requirements of microelectronics and MEMS are the same, such as the precise alignment of features in different material layers to each other. There are some particular requirements of MEMS fabrication in order to achieve mechanical, movable features. One example of a process that was specifically designed for MEMS fabrication is the Bosch process[1], which allows the etching of deep trenches in silicon substrates with nearly vertical sidewalls. There are many good resources describing the basic, individual MEMS fabrication processes in great detail.[2] Here, an overview of several process flows is given. Details of individual processing steps are only described in the text if they are non-conventional and specific to this work. Complete processing details in tabular form are given in Appendixes A and B. The deposition of aluminum nitride (AlN) with very specific properties is so fundamental to this research that it is described separately in Chapter 2.

The process runs performed in this Ph.D. research include every step from blank silicon wafers to individual sensor chips wire-bonded to a secondary package and ready to be connected to external electronic circuits. Two types of process flows were utilized, one that relies entirely on surface-micromachining and one that combines surface-micromachining with bulk-micromachining process steps. Surface-micromachining is the deposition and modification of films on a substrate, e.g., a silicon wafer, without any modification to the substrate itself. Bulk-micromachining is the modification of the substrate, e.g., by etching, to locally give it added functionality beyond providing a structural base for the device layers. One example is the definition of large proof masses for accelerometers as utilized in the devices introduced in Chapter 4.

[1]The term "Bosch process" is commonly used for a deep reactive ion etching process that was developed at the German company Robert Bosch GmbH. This process uses alternating polymer deposition and etching steps to achieve a very anisotropic etch profile. The method is patented by Bosch [34, 35] and widely used in the MEMS industry.

[2]The interested reader is referred to the very good classic single-volume work on microfabrication by Madou [36] and its three-volume successor [37].

3.1 Surface-micromachined, bottom-up aluminum nitride fabrication

The process flow in this section describes the fabrication of devices that utilize AlN as structural material for the sensor elements. The underlying silicon substrate is merely a carrier for the devices and plays no active role in the sensor operation. The process flow presented here does not fall into the strict definition of surface-micromachining because localized cavities are etched into the silicon substrate to release the AlN structures. Nevertheless, the term surface-micromachined was chosen for this process flow to differentiate it from the combined surface- and bulk-micromachined process flow in which the silicon plays an active role for the sensor elements. A method that would convert the process flow into pure surface-micromachining is described in Section 3.4.

The first fabrication process that was used for this dissertation research was developed from a process previously used to make MEMS resonators for filters and frequency references [38, 39][3]. The complete process parameters for all fabrication steps are given in Appendix A. The key steps of the process are shown schematically in Fig. 3.1. The process is termed bottom-up approach

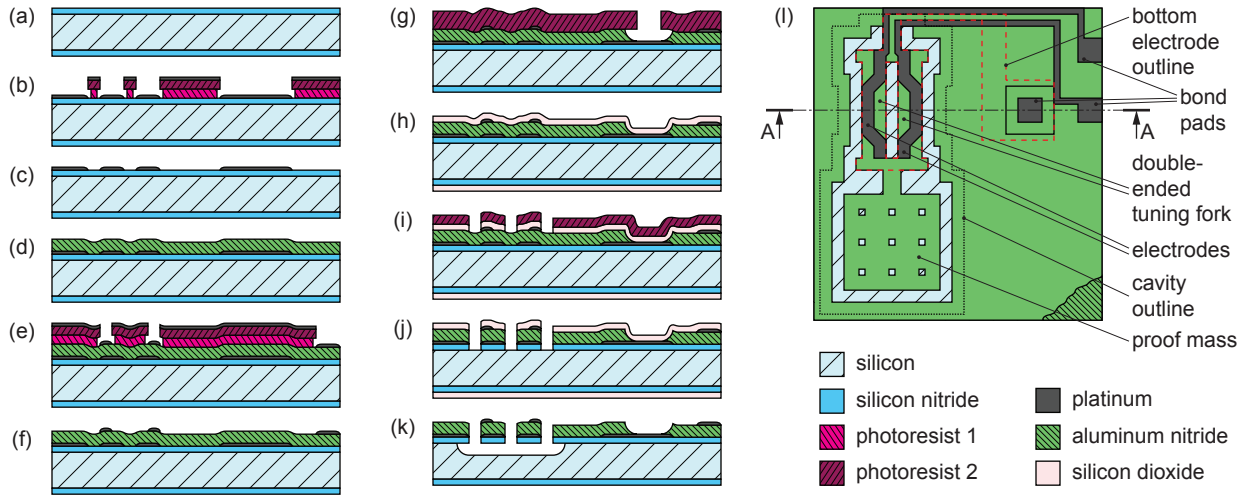

Figure 3.1. Schematic cross-sections of different stages during the surface-micromachined, bottom-up aluminum nitride fabrication process (a-k) taken at the line marked A-A in the schematic top-view of the final device (l).

here because each layer is individually deposited and patterned before the next layer is deposited. This approach allows for maximal design freedom for the three main layers of the sensors to be fabricated, i.e. the bottom electrode, the piezoelectric AlN layer and the top electrode. The disadvantages of this approach include the reduced control of stress and crystal orientation of the AlN layer on top of the already patterned bottom electrode. The film stress is measured by comparing the wafer curvature before and after AlN deposition as described in Section 2.3.3. However, the areas covered with bottom electrode will experience a different AlN growth than the areas that are not covered. Consequently, the global wafer stress measurement does not accurately reflect the

[3]The process presented in this section was developed in cooperation with Dr. Gabriele Vigevani.

stress in the areas of interest, i.e. on top of the bottom electrodes. Another disadvantage of this process is the repeated switching between deposition and lithography steps, which complicates the fabrication process. It also requires the usage of a special type of developer, *Shipley CD-30*, to be used for some of the lithography steps because standard photoresist developers contain tetramethylammonium hydroxide (TMAH), which chemically attacks AlN. Unlike the standard developers, which can be applied in an automated process in the Berkeley Nanolab, CD-30 has to be used in manual development. As a result, the repeatability of the process suffers and the fabrication process is more complex.

As shown in Fig. 3.1a, the fabrication of the 15 cm-silicon wafers begins with the deposition of a 300 nm layer of silicon nitride (Si_3N_4) using low temperature chemical vapor deposition (LPCVD). This layer electrically insulates the bottom electrodes from the silicon wafer and thus from each other. As shown in parts b and c, the bottom electrode is patterned using a photoresist bilayer of 1.1 μm *OiR 10i* on top of 1.3 μm *OCG 825*. As the latter photoresist type gets developed faster in the CD-30 developer, the former ends up with a slight overhang of a few tens of one μm thus improving the subsequent lift-off process by increasing the area exposed to the solvent. All lithographic exposures are performed in a wafer stepper with 5:1 reduction optics using a 10 cm-square mask with a 5 cm-square usable area to achieve the final die size of about 1 cm-square. In this lithography step, the exposure and development times are optimized for the top photoresist layer. The metal film consists of a 100 nm layer of platinum on a 10 nm layer of chromium, which helps the adhesion of platinum to the Si_3N_4 surface. After performing the lift-off of the photoresist in acetone a 2 μm layer of AlN is deposited. The details are described in Chapter 2. As mentioned above in this section, it is difficult to achieve and verify the target of close to 0 MPa of film stress in the AlN on top of the patterned bottom electrode. Next, the platinum top electrode is patterned using the identical lift-off process as for the bottom electrode (Fig. 3.1e and f). This photomask and the two subsequent masks are all aligned to the alignment marks created in the bottom electrode patterning step. The repeated alignment to the first layer avoids adding up alignment errors if each mask were aligned to the previous step and it is possible because the first alignment mark remains easily visible through the AlN layer.

As shown in part g of the process schematic, a photoresist mask is used for an AlN etching process that opens contact holes for electrical connection to the bottom electrode. Hot phosphoric acid is used to remove the AlN because of its high AlN etch rate and good selectivity to platinum and photoresist. LPCVD at a low temperature of 400 °C is used to deposit a silicon dioxide (SiO_2) layer (Fig. 3.1h). The SiO_2 is patterned with a photoresist mask using reactive ion etching (RIE) and a fluoroform (CHF_3)/tetrafluoromethane (CF_4) chemistry (Fig. 3.1i). The photoresist is then removed and the features are transferred from the SiO_2 into the underlying AlN using a second RIE step with chlorine (Cl_2)/boron tricholoride (BCl_3) chemistry (Fig. 3.1j). This two-step process is chosen to create the AlN pattern instead of using a photoresist mask directly because it has been shown to result in more vertical AlN sidewalls [40]. The second RIE step also etches Si_3N_4 and it is performed until silicon is exposed in all etched areas.

The remaining steps of the fabrication process are performed on the die-level. First, a protective layer of photoresist is coated on the front side of the wafer. The wafer is then diced along the outside of the individual device dies with a vertical and horizontal pitch of 10.16 mm. Due to the blade width of 45 μm, the size of the resulting dies is about 10.115 mm-square. Solvents are used

to remove the photoresist from individual dies and to clean them. The SiO_2 layer is then removed in 5:1 buffered hydrofluoric acid (BHF). The final step is the formation of cavities in the silicon to release the AlN devices. Gaseous xenon difluoride (XeF_2) is used to etch the silicon isotropically for a defined period of time until all desired structures have been fully released. Stiction problems that could arise from liquid silicon etchants can be avoided using the gaseous XeF_2. The final cross-section and a schematic top-view indicating the location of the cross-section (A-A) are shown in Fig. 3.1k and l, respectively. The device shown in the top view is a simplified accelerometer with a proof mass attached to a double-ended tuning fork (DETF).

3.2 Surface- and bulk-micromachined, top-down aluminum nitride fabrication

The second of the two major fabrication processes developed in this dissertation research differs in many key aspects from the process shown in the previous section.[4] Most notably, the silicon wafer is no longer merely the substrate upon which the AlN devices are built, but it becomes part of the devices in many cases. Thus, in addition to surface-micromachining steps, bulk micromachining, i.e. the etching of features into the silicon wafer from the backside, is performed. The second big difference to the first fabrication process is the top-down approach taken in this process. Instead of depositing individual layers and patterning them individually, all functional layers are deposited at the beginning of the process and patterned subsequently. This method results in improved AlN film quality and stress control. Although the fabrication process is compatible with a single structural AlN layer for in-plane motion, it is used here to make an AlN bilayer. The top layer is the piezoelectrically active AlN and the bottom AlN layer of identical thickness is used to shift the neutral axis of the system away from the center line of the active layer, thus allowing for out-of-plane actuation. As discussed in later chapters of this dissertation, out-of-plane actuation enables the usage of different types of sensors compared to in-plane actuation. Examples include membrane pressure sensors and triple-beam tuning fork (TBTF) accelerometers. A top view of both of these devices is shown schematically in Fig. 3.2m. The line marked A-A shows the location of the cross-section, which is shown at key points during the fabrication process in parts a-l of the figure.

For this process, double-sided polished 15 cm-silicon wafers are used because both sides of the wafer are photolithographically patterned during the process. The fabrication process begins with the deposition of the two AlN layers with a molybdenum layer in between and a molybdenum layer on top. If the exact deposition parameters have been determined all of these layers can be deposited in the Berkeley Nanolab's *Tegal Endeavor* multi-chamber sputtering tool without breaking vacuum between depositions resulting in the best possible film quality. For this dissertation research, the wafers were unloaded from the tool after each deposition step to determine the film stress level in order to modify the deposition parameters for the next batch of wafers. The contamination of the

[4]This process was developed in cooperation with Kansho Yamamoto of Murata Manufacturing Co., Ltd. and Dr. Gabriele Vigevani and Kirti Mansukhani of UC Berkeley.

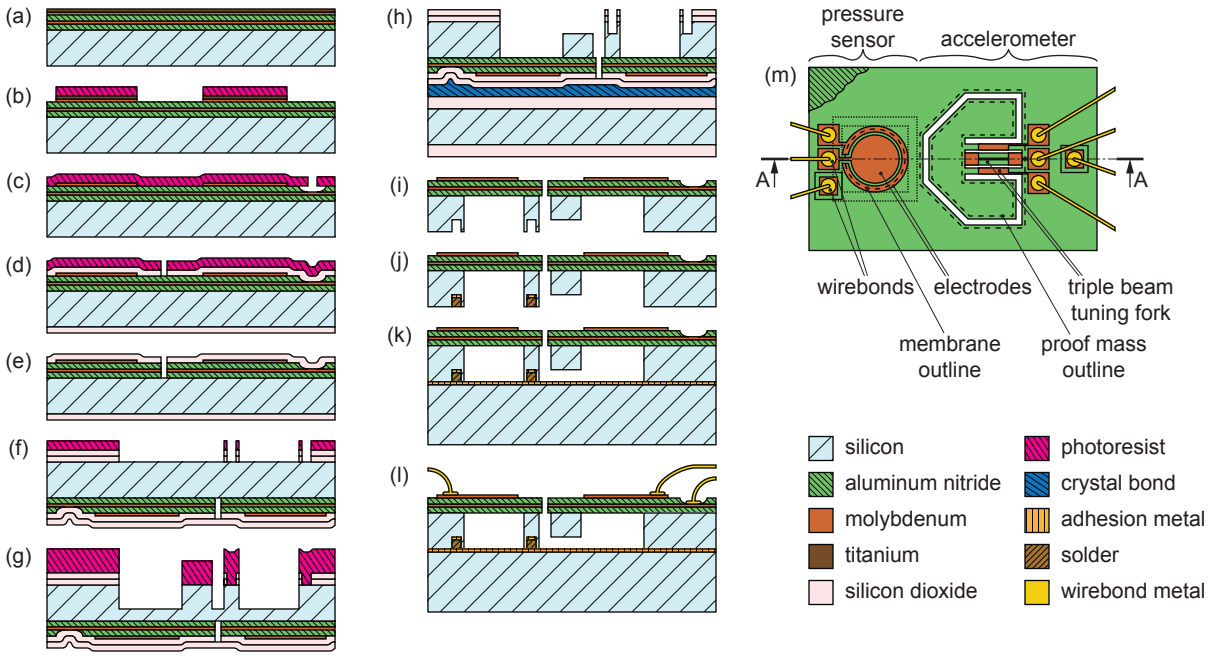

Figure 3.2. Schematic cross-sections of different stages during the surface- and bulk-micromachined, top-down aluminum nitride fabrication process (a-i) and during the packaging steps (j-l) taken at the line marked A-A in the schematic top-view of the final device (m).

wafer surface during the short optical measurement of the wafer curvature that is required for the film stress characterization is minimal and can be removed by a short sputter etching step in the Endeavor tool prior to deposition of the next film. The target thicknesses for each AlN layer and each molybdenum layer are 1 μm and 100 nm, respectively. The stress level in the molybdenum films can be adjusted by applying an RF bias to the wafer during the DC molybdenum sputtering similar to the stress control described for AlN in Chapter 2. However, it has been found that it is important to run about the first third of the molybdenum deposition without RF bias to achieve a good crystal structure and only turn on the RF bias for the remainder of the deposition to adjust the film stress. A good crystal orientation, i.e. a FWHM value of the molybdenum rocking curve smaller than 3°, is critical to achieve good c-axis orientation of the AlN layer grown on top of the molybdenum. The two-step process results in both adequate molybdenum crystal structure and good stress control, typically within ±50 MPa. After the functional layers have been deposited, a 7.5 nm adhesion layer of titanium is deposited using electron-beam evaporation (Fig. 3.2a). This layer has been found to be critical for good photoresist adhesion on the top molybdenum and thus optimal feature resolution of the top electrode.

The first three lithography processes, i.e. all of the surface micromachining on the wafer front side, are performed with the 5:1 wafer stepper as described in Section 3.1. After patterning a layer of photoresist with the top electrode mask the top molybdenum layer is transfered to the underlying titanium and molybdenum layers by subsequent RIE processes in Cl_2/BCl_3 and Cl_2 chemistries, respectively (Fig. 3.2b). Both etch steps can be performed consecutively in the metal etching chamber of the Berkeley Nanolab's *Applied Materials Centura* etching tool. After pho-

toresist removal, the remaining titanium film is removed by a short blanket etch with the same parameters as the for the titanium patterning. Then, a new photoresist layer is deposited and patterned with openings to contact the bottom molybdenum layer. The mask is aligned to the top electrode mask, but the alignment is not critical. The patterns are transfered into the top AlN layer by wet etching in hot phosphoric acid (Fig. 3.2c). After removal of the photoresist, a layer of SiO_2 as hardmask for the subsequent AlN and molybdenum etch steps is deposited using a low-temperature LPCVD process. The SiO_2 is patterned with photoresist using the mask for the structural device features and an RIE process with octafluorocyclobutane (C_4F_8) chemistry (Fig. 3.2d). The alignment of this mask to the top electrode features is the only critical alignment step in the surface-micromachining portion of this fabrication process. After photoresist removal, the features are transfered into the top AlN, bottom molybdenum and bottom AlN layers using RIE and alternating between Cl_2/BCl_3 and Cl_2 chemistries for the AlN and molybdenum portions, respectively. Similar to the titanium/molybdenum patterning, the wafer stays in the same chamber of the Centura tool for the whole duration of this process, which makes the patterning of the layer stack very efficient.

The remainder of the fabrication process is termed bulk-micromachining because it deals with the formation of openings and defined mass portions in the bulk material, i.e. the silicon substrate. The goals of the process are to create released masses that are thinner than the wafer thickness and thus do not contact the chip carrier and to create openings that extend through the entire silicon substrate. The former features are used as proof masses for accelerometers while the latter are important for the released tuning fork and membrane areas. In order to achieve these two different etch depths on the backside of the wafer, two separately removable mask layers are needed. The first layer is formed by SiO_2 that is already present from the previous deposition step and an additionally deposited layer of SiO_2. This layer stack is patterned using photoresist and a contact mask aligner in backside alignment mode. The alignment accuracy to the top electrode features that can be achieved in this mode is worse than that of the surface micromachining processes. However, due to the design of the tuning fork and membrane patterns it is also less critical and an alignment accuracy of ± 5 μm is typically sufficient. The features are transfered into the SiO_2 layer using the same RIE process as before (Fig. 3.2f). The second mask for the backside silicon etch is formed by thick, hard baked photoresist that is deposited on the wafer backside and aligned to the previously created oxide mask features. For the deep etching of the silicon a *Bosch* process, i.e. alternating cycles of polymer deposition in C_4F_8 chemistry and etching in sulfur hexafluoride (SF_6)/oxygen, is used. Practically vertical sidewalls can be achieved if the cycle times are adjusted correctly, which is important for the performance of the sensor structures. For the first portion of the silicon etching, only areas that are covered by neither SiO_2 nor photoresist masks are etched (Fig. 3.2g). The etch depth of this portion determines the thickness of the proof masses. When the desired etch depth is reached as measured optically or using a stylus-based surface profiler the photoresist mask is removed in an oxygen plasma. In preparation of the final silicon etch the wafer is bonded onto a SiO_2 coated carrier wafer with a special adhesive of type *Crystalbond 509*. This step is critical as the outer etch channels in this process are used to separate the individual dies, i.e. the wafer is no longer a single unit at the end of the silicon etching process. After the wafer bonding procedure the Bosch process is continued until all open areas are cleanly etched down to the bottom AlN layer of the front side wafer stack as verified visually (Fig. 3.2h). In this process, the AlN layer represents an excellent etch stop with an estimated selectivity to the silicon etch of

about 400:1. The final steps of the fabrication process are removal of the individual dies from the carrier wafer by dissolving the adhesive in acetone, solvent cleaning of the dies and removal of the SiO_2 layer in gaseous hydrofluoric acid (HF). In the final cross-section in Fig. 3.2i, the four types of features created in the backside silicon etching steps are apparent. On the left side, a membrane is formed by etching down to the AlN and it is bordered on either side by full thickness silicon. The membrane is surrounded by a partially etched channel that is later used for a die-bonding process. On the right side, the fourth type of feature is shown, the proof mass of the accelerometer, which is thinner than the full wafer thickness, completely detached from the substrate and only held by the AlN tuning fork. Parts j-l of the figure show one possible packaging scenario for the dies created with this fabrication process, which is described in Section 3.3.2.

3.3 Packaging

Packaging is not a major focus of this dissertation research. However, in order to test any MEMS prototype it needs to be interfaced mechanically and electrically to the outside world. In this section, the critical aspects of packaging the dies fabricated with the processes of the previous sections are discussed. The challenges that needed to be overcome to create electrical connections to the devices by wirebonding and three different methods of die attachment for the sensors chips are explained.

3.3.1 Wirebonding

Both the surface-micromachined and the surface- and bulk-micromachined devices are electrically connected to primary package, which is typically a ceramic carrier such as the one shown in Fig. 3.3a, by standard wedge-wedge wirebonds. Either aluminum or gold is used as wirebond material and the choice depends on maximum operating temperature, adhesion to the bond pads and tool availability. In general, aluminum is easier to use and has been shown to work reliably up to at least 600 °C. One problem that arose with the first generation of accelerometers created by the surface- and bulk-micromachining process was TBTFs breaking off during wirebonding. It is speculated that the ultrasonic excitation of the tool excited a mode shape of the device that led to its destruction. Three steps were taken to alleviate this problem. First, longer traces were used to spatially separate the TBTFs from the bond pads and thus dampen the excitation amplitude. Second, it was found that the TBTF devices would break at sharp concave corners, which would create stress concentration areas (Fig. 3.3b). These corners were rounded in the later generation devices, which led to a reduction in the number of failures. However, the corners at the connection of the TBTF base to the substrate were not rounded and they also create sites for crack intiation as shown in Fig. 3.3c. Finally, a special processing procedure was developed to reliably wirebond both the early devices and the improved devices. In this procedure, the device die is first bonded to the chip carrier using an epoxy that is not easily soluble in acetone. Then, a drop of photoresist is carefully placed close to the proof masses of the accelerometer device. The photoresist is pulled into the trenches around the proof masses by capillary action and creates enough damping to prevent

breakage of the TBTFs during the wirebonding procedure. Immediately following wirebonding the entire chip carrier with the now wirebonded accelerometer is immersed in acetone to remove the photoresist. It is important not to bake the photoresist or let it dry completely in this process as those steps would make complete removal virtually impossible.

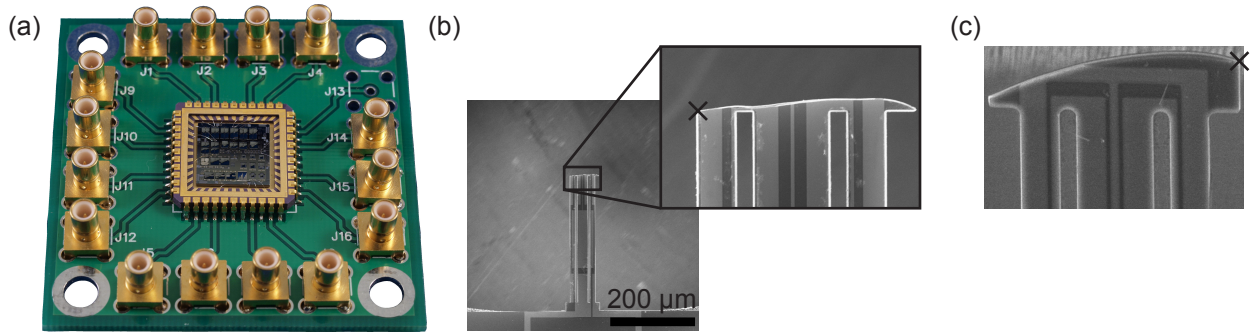

Figure 3.3. (a): AlN MEMS sensor die mounted on a ceramic chip carrier, which is soldered to a PCB with SMB connectors. The size of the MEMS die is 10 mm-square and the size of the PCB is 2 inch-square. (b): SEM overview and closeup images of a TBTF broken at a stress concentration area (black x). (c): SEM image of improved TBTF design with rounded concave corners to elminate stress concentration at the tines. Not rounded at the base which also creates a failure site (black x).

3.3.2 Chip attachment

Another aspect of the primary packaging procedure is the attachment of the sensor die to the primary package. If there are no special requirements for hermetic sealing, strain transfer from the substrate or high temperature operation a temporary attachment can be achieved by using double-sided adhesive tape. This method has the advantage that ceramic carriers as primary package are reusable for several sensor dies, which reduces the cost in a research environment. For the special wirebonding procedure described above the adhesive tape is replaced with epoxy, which is similarly easy to use, but not easily removable. In the following paragraphs three attachment methods are described that each perform a special function.

The first method is for force sensing with DETFs as described in Section 4.5.1. A defined force is applied to the DETF by creating a strong mechanical connection of the sensor chip to a thin steel parallel and applying an external bending force to the parallel. The required strong bond was formed by joining the chip to the steel surface using a layer of 96.5Sn-3Ag-0.5Cu lead-free solder paste. The heat to liquefy the solder was applied locally at the connection point using an induction coil. To achieve proper adhesion of the solder to the underside of the silicon sensor chip and to the steel parallel, both surfaces need to be prepared. On the steel surface it is sufficient to remove any oxide film using fine sandpaper. The silicon, however, will not wet with the solder directly, so an adhesion layer must be deposited. For this purpose, a layer stack starting with titanium followed by nickel and gold is electron-beam evaporated onto the backside of the device die. The thicknesses

of these layers are 25 nm, 400 nm and 10 nm, respectively.[5] An example of a sensor chip bonded to the steel parallel is shown in Fig. 3.4a.

The second type of die attachment method could be described as zero-level packaging. Here, the sensor die is not attached to a die carrier but to another silicon die. This method is used to create hermetically sealed cavities under membranes that can then be used as pressure sensors. The pressure difference between the cavity and the environmental pressure causes tension in the membrane, which changes its resonance frequency [42]. In preparation of the bonding process, both the backside of the sensor die and a blank silicon die are coated with an adhesion layer of titanium and a thicker layer (about 100 nm) of gold using electron-beam evaporation. The same lead-free solder paste as described above is manually applied into the trench on the backside of the device die and it is placed on the bare silicon die. The die stack is sandwiched between two glass slides and transfered onto a hotplate where it is heated above the solder's melting point of 217 °C. Removing the die stack from the hotplate and cooling to room temperature completes the bonding process. The resuling device die with hermetically sealed membranes can be attached to the primary package and wirebonded in the regular way.

Finally, for high temperature testing of the sensor chips special considerations have to be made. Using a regular printed circuit board (PCB) with coaxial connectors as shown in Fig. 3.3 and standard coaxial cables to connect the sensors to external electronics is not possible above about 150 °C. The adhesives that are used to connect the sensor die to the primary packaging and the solder used to connect the packaging to the PCB are also not compatible with high temperature operation. Instead, a high temperature compatible circuit board made of aluminum oxide was designed to mount the sensor die directly (Fig. 3.4b). High temperature wires are connected to this circuit board using screw connectors. The sensor chip is held in place using high temperature adhesive. Regular wirebonds can be used to establish the electrical connection from the bond pads of the sensor chip to the gold traces on the ceramic board.

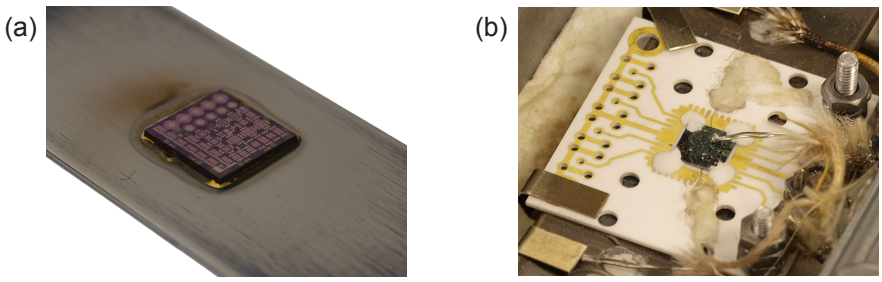

Figure 3.4. Methods of mounting the AlN MEMS sensor die. (a): Soldered to a steel parallel for strain transfer from the metal to the sensor die. (b): Glued to a ceramic board for high temperature testing.

[5]The bonding process was adapted for this sensor chip in cooperation with Matthew Chan based on previous work [41].

3.4 Summary and evaluation

It can be seen that the surface- and bulk-micromachining process evolved from the surface-micromachining process. The comparison of the processes' key aspects given in Table 3.1 show that both processes have advantages and disadvantages. The surface-micromachining process can easily be modified to be completely post-complementary metal-oxide-semiconductor (CMOS) compatible as discussed below. It is also much better suited for devices, in which the capacitance of electrical traces to the ground plane, i.e. the bottom electrode, must be minimized. The lift-off patterning of the bottom electrode metal can be used such that only the active device areas, such as the DETF tines, have both bottom and top electrode metal. 1-port resonators, such as some Lamb wave resonators and DETFs, exhibit much better performance with lower capacitance to ground. On the other hand, all of the sensors discussed in this dissertation research are 2-port devices, for which the capacitance between the input and output ports and not the capacitance to ground is critical. The main advantages of the surface- and bulk-micromachining process are the much bigger proof masses and the option to create sealed membranes. In Chapter 4, it will be shown that the former are critical components for high performance accelerometers. The sealed membranes are required for pressure sensors. Other specific advantages and disadvantages of the two fabrication processes regarding film deposition, lithography and general processing are listed in Table 3.1.

In Section 3.1, it was mentioned that none of the fabrication processes developed for this work are true surface-micromachining processes, i.e. without modification of the underlying silicon substrate. There are, however, scenarios in which the substrate should not be altered. One example

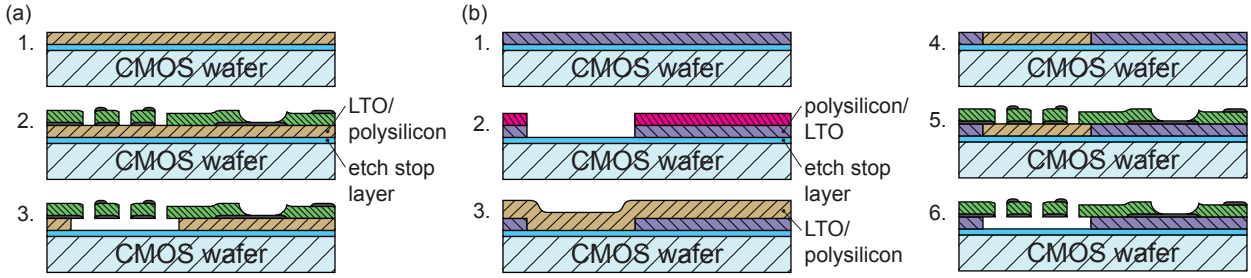

Figure 3.5. Process modifications to make the surface-micromachining process fully post-CMOS compatible. (a): Timed release using a sacrificial layer of low-temperature silicon dioxide or polysilicon and an etch stop layer. (b): Release using CMP to create islands of low-temperature silicon dioxide or polysilicon in the other material.

would be the placement of sensing elements directly on top of application-specific integrated circuits (ASICs) that are used to operate the sensing elements and read out the desired signals. None of the process steps required for the fabrication of the AlN sensors utilize temperatures above 400 °C. Therefore, it is possible to create the sensors in a post-CMOS fabrication flow directly on top of the CMOS electronics. A modification that would need to be made to the fabrication process described in Section 3.1 is to replace the formation of cavities in the silicon substrate with localized etching of a sacrificial layer. Polysilicon is a possible film layer that can be deposited in a low-temperature sputtering process [43]. XeF_2 can be used to etch the polysilicon release layer and the metal/AlN/metal film stack can be deposited directly on the polysilicon layer with good film quality [44]. An alternative to polysilicon as sacrificial layer is low-temperature deposited

Table 3.1. Comparison of the two fabrication processes. Advantageous property shown in boldface.

Category	Surface-micromachining process	Surface- and bulk-micromachining process
Capability	**Easy to convert to pure surface micromachining process → can be performed directly on CMOS electronics**	Impossible to use directly on CMOS because of back side etching
	Proof masses small and scale with area (fixed thickness)	**Proof masses large and scale with area and thickness**
	Release from front side and need for release holes make hermetically sealed membranes impossible	**Backside release means no need for release holes and results in easy packaging for hermetically sealed membranes**
	Patterned bottom electrode → reduced ground capacitance (important for 1-port devices)	Blanket bottom electrode → higher ground capacitance (bad for 1-port devices, but irrelevant for 2-port devices)
Film deposition	Films deposited at different times during process → contamination and reduction in film quality possible	**All films deposited in same tool without breaking vacuum at beginning of process → best possible film quality**
	Evaporative deposition of electrode metals → little stress control	**Sputter deposition of electrode metals → precise stress control**
	AlN layer deposited on mixed surface (metal/silicon nitride) → stress measurement difficult	**AlN deposited on blanket metal film** → stress measurement simple
Lithography	**All four exposure steps with same 5:1 projection tool on front side of wafer**	Three exposure steps with 5:1 projection tool on front side of wafer, one backside alignment step with contact tool on backside of wafer and one frontside alignment step with contact tool on backside of wafer
	Patterned bottom electrode adds a critical alignment step during surface-micromachining	**Self aligned bottom electrode**
	Exposed AlN during lithography steps makes manual development with CD-30 developer necessary → less repeatability and potentially lower resolution	**No exposed aluminum nitride during lithography steps means that automatic development with standard developers can be used → better repeatability and potentially higher resolution**
Processing	**XeF_2 release → fast and stable process**	Release by backside etching with Bosch process → slow and more difficult to control

SiO_2. This material has been demonstrated as an underlayer for AlN devices [**?**]. The final release is performed in gaseous HF. Avoiding the etch step in XeF_2 has the advantage that molybdenum can be used for the electrodes, which would otherwise be etched by the XeF_2 gas. Finally, combination processes of polysilicon and SiO_2 can be employed to avoid the need for a timed release step. In this case, one of the materials is deposited first and a cavity is etched. The other material is deposited and the substrate is smoothed by use of chemical-mechanical polishing (CMP). The AlN structure to be released is then formed on one of the materials that is finally etched away with good selectivity to the other material. The advantage of this process modification is precise control over the etch cavity dimensions compared to the timed release method. The proposed process modification options are shown in Fig. 3.5. Another material that has been demonstrated as sacrificial layer for AlN resonators and can be deposited at a temperature of less than 400 °C is amorphous silicon [45].

Chapter 4

Tuning Fork Sensors

In this chapter, sensors based on two types of tuning fork sensing elements are discussed. The first type is the double-ended tuning fork (DETF), which vibrates within the substrate plane. The second type is the triple-beam tuning fork (TBTF), which vibrates out of the substrate plane. In the first three sections, the details about each type of tuning fork structure are explained and it is shown that a simple equivalent circuit model can be used to analyze the electromechanical behavior of both. Sensing of external loads, such as accelerations and substrate strain, using stress- and deformation based approaches is explained in Sections 4.5.1 and 4.5.2.

4.1 Double-ended tuning forks vs. triple-beam tuning forks

The basic design for a micro-electromechanical system (MEMS) DETF is shown in Fig. 4.1a. The device consists of two tines that are connected to each other via an anchor on each end. One of the anchors is connected to the substrate via a tether, while the other anchor is connected to the mechanical load via an identical tether. MEMS DETFs are generally operated in their in-plane operation modes, i.e. the deformation of the tines takes place within the substrate plane. MEMS TBTFs, on the other hand, are used in out-of-plane vibration modes. A TBTF as shown in Fig. 4.1b consists of three tines, of which the center tine may have a different width than the two side tines. The three tines are connected to a common base portion on each end. One of the bases is attached to the substrate while the other one is attached to the mechanical load. The first twenty vibration mode shapes of MEMS DETFs and TBTFs with typical dimensions are shown in Fig. 4.2. MEMS DETFs have been used as sensing elements for many different applications. In almost all cases, silicon devices are used that can be manufactured with conventional fabrication processes. In such devices, the electromechanical transduction is achieved electrostatically using either parallel plates [46, 47] or comb drives [48, 49]. Such silicon devices have been used for sensing of mechanical signals such as force [46, 48, 50, 51], strain [49, 47, 52, 53, 54] and acceleration [55, 56, 57]. Silicon

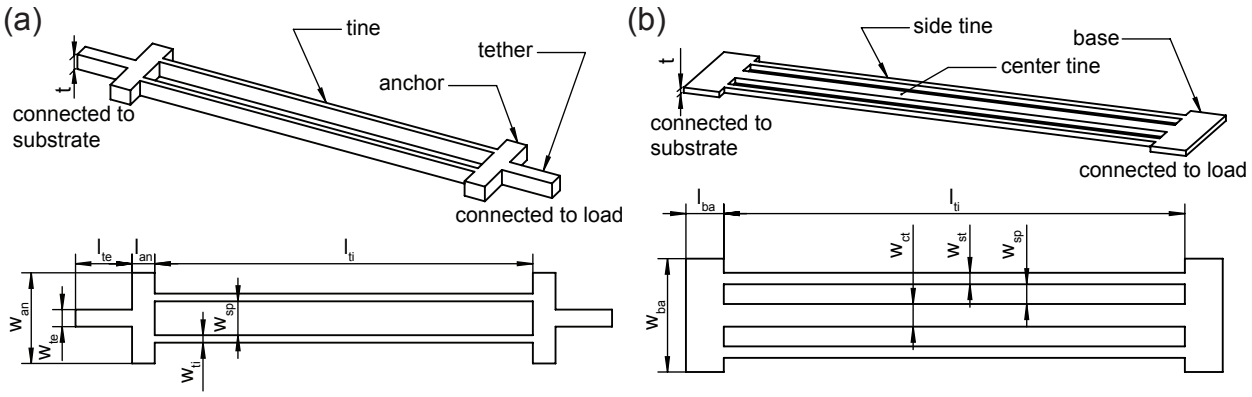

Figure 4.1. Schematic views with geometric dimensions for (a) double-ended tuning fork and (b) triple-beam tuning fork.

DETF have also been used for sensing environmental conditions such as temperature [58] and humidity [59] and as electrometers [60]. They have even been integrated directly with transistor elements [61, 62, 63]. Silicon carbide has been used as a material for electrostatic DETFs as an alternative to silicon for harsh environment applications [64, 65]. Piezoelectric DETFs have not been widely used. They do not rely on the electrostatic attraction between charged electrodes, but the electromechanical transduction is achieved in the material directly. Although quartz has been used in a few cases [66, 67, 68] it is not a promising material because of the need for unconventional fabrication steps. Aluminum nitride (AlN) is the material of choice for this doctoral research because of its advantages in fabrication, integration and high temperature operation. DETFs that use AlN as structural and piezoelectrically active material have been fabricated at the Berkeley Micromechanical Analysis and Design Laboratory (BMAD) [69] and used for strain sensing [70] and accelerometers [17]. The accelerometer concept was previously introduced in [6, 71]. One of the advantages of piezoelectric operation is that small gaps, as needed for electrostatic actuation, are not necessary. The ability to use TBTFs as sensing elements and utilize deformation-based sensing (see Section 4.5.2) are a direct result of this advantage and would not be possible with electrostatic actuation.

4.2 Admittance model

A common electromechanical coupling method for MEMS is electrostatic coupling with parallel plate or comb drive capacitors. In this work, piezoelectric coupling of the beams is investigated. Specifically, the beams are both the mechanical resonator and the actuation/sensing element. Unlike a beam with a comb drive attached to its center, the mechanical system and the electromechanical coupling cannot be designed independently here. Therefore, an analysis of geometric parameter variation on the device's electromechanical performance is crucial. In specific, the complex admittance Y_{21} of the tuning fork sensors is an important property for the prediction and optimization of the device behavior. The indices 1 and 2 represent the input and output ports of the 2-port tuning

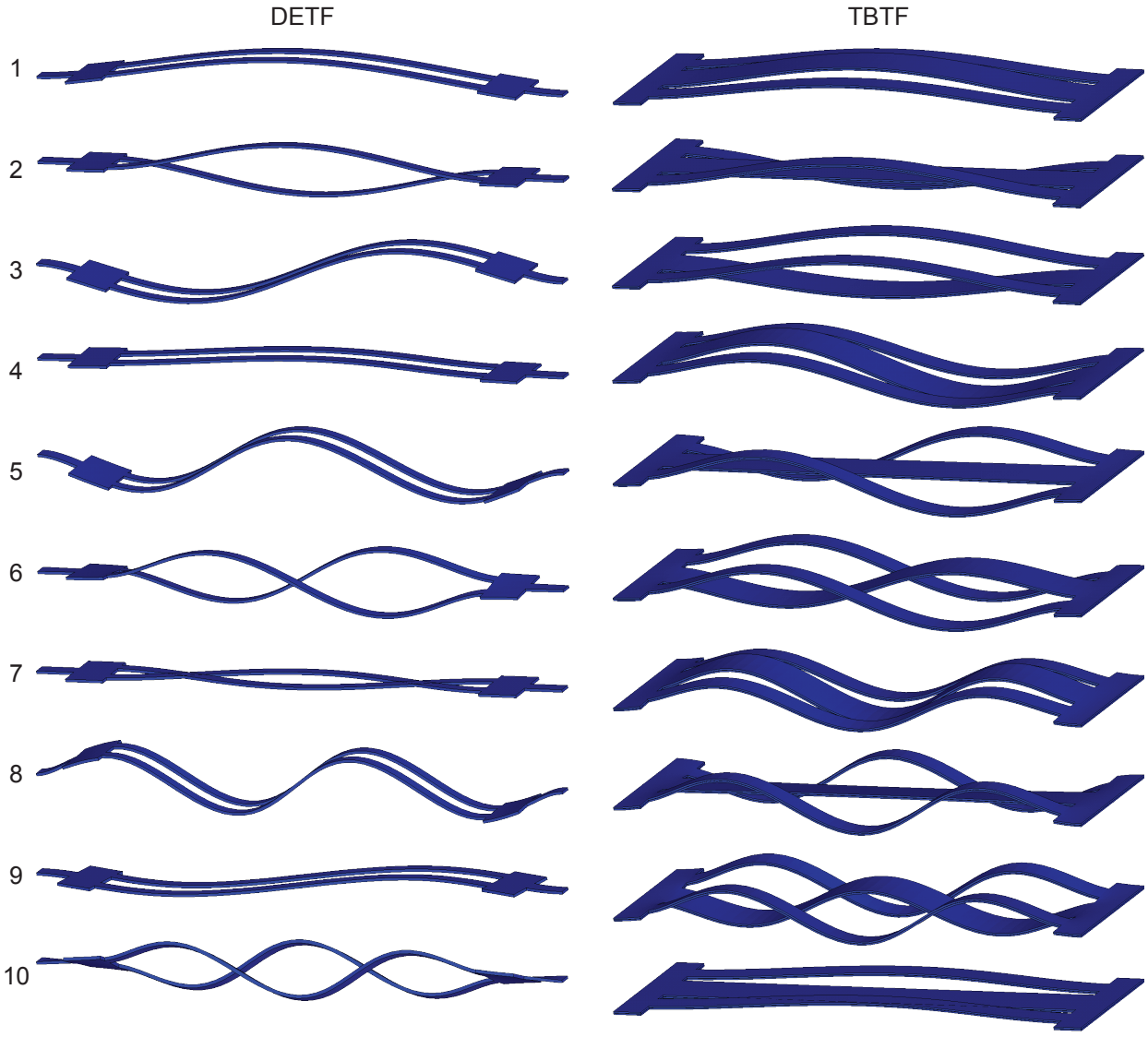

Figure 4.2. First ten resonance mode shapes of double-ended tuning fork (left) and triple-beam tuning fork (right).

fork, respectively. Therefore, the mentioned admittance is the ratio of complex current flowing from the output port to complex voltage applied at the input port:

$$Y_{21}(j\omega) = \frac{I_2(j\omega)}{V_1(j\omega)} \tag{4.1}$$

For individual beam resonators, the admittance can be written in a generalized form as the product of the generalized transfer function ${}^{Z(j\omega)}/_{F(j\omega)}$ and two electromechanical coupling parameters η_1 and η_2 [72]:

$$Y_{21}(j\omega) = j\omega \frac{Z(j\omega)}{F(j\omega)} \times \eta_1 \times \eta_2 \tag{4.2}$$

The generalized transfer function is the ratio of the generalized beam displacement $Z(j\omega)$ and the generalized beam force $F(j\omega)$. It can be written as [73]:

$$\frac{Z(j\omega)}{F(j\omega)} = \frac{1}{M\omega_1^2\left(1 - \left(\frac{\omega}{\omega_1}\right)^2 + j\left(\frac{\omega}{\omega_1}\right)\frac{1}{Q}\right)} \tag{4.3}$$

For the fundamental mode of a clamped-clamped beam, the generalized mass M, resonance frequency ω_1 and quality factor Q are given by the following equations:

$$M = 1.036\rho bhL \tag{4.4}$$

$$\omega_1 = 4.73^2 \sqrt{\frac{E_{AlN} I}{\rho bhL^4}} \tag{4.5}$$

$$Q = \omega_1 \frac{M}{c} \tag{4.6}$$

Here, ρ and E_{AlN} are the mass density and Young's modulus of the beam's material, respectively, b, h and L are the width, height and length of the beam, respecitively, and c is the generalized damping. The second moment of area I depends on the direction of the beam deformation and is a different expression for the DETF beams and the TBTF beams:

$$I_{DETF} = \frac{b^3 h}{12} \tag{4.7}$$

$$I_{TBTF} = \frac{bh^3}{12} \tag{4.8}$$

The electromechanical coupling coefficients η_1 and η_2 are dependent on the coupling mechanism and the device design. At the input port, η_1 is responsible for the conversion of applied voltage to generalized force and at the output port, η_2 is responsible for the conversion of generalized displacement to ouput current:

$$\eta_1 = \frac{F(j\omega)}{V_1(j\omega)} \tag{4.9}$$

$$\eta_2 = \frac{1}{j\omega} \frac{I_2(j\omega)}{Z(j\omega)} \tag{4.10}$$

Up to this point, the treatment of both DETF and TBTF beams is identical with the exception of the second moment of inertia. However, the derivation of the coupling coefficients is highly dependent on the type of device and its specific design. The electromechanical coupling is discussed for a DETF design and a TBTF design in sections 4.2.1 and 4.2.2, respectively. For both cases, the deformed shape of the vibrating beam at the resonance mode of interest must be described by a mathematical function. This mode shape can easily be derived from the Euler-Bernoulli beam bending equation[1]. The function $\phi(x)$ describing the distance from the undeformed shape along the length direction x of a clamped-clamped beam and its first derivative $\phi'(x)$, i.e. the angle of the beam, are:

$$\phi_n(x) = \sinh(\beta_n x) - \sin(\beta_n x) + \alpha_n\big(\cosh(\beta_n x) - \cos(\beta_n x)\big) \tag{4.11}$$

$$\phi_n'(x) = \beta\Big(\cosh(\beta_n x) - \cos(\beta_n x) + \alpha_n\big(\sinh(\beta_n x) + \sin(\beta_n x)\big)\Big) \tag{4.12}$$

$$\alpha_n = \frac{\sinh(\beta_n L) - \sin(\beta_n L)}{\cos(\beta_n L) - \cosh(\beta_n L)} \tag{4.13}$$

The parameter $\beta_n L$ has to be numerically determined and for the first three mode shapes of the clamped-clamped beam it is $\beta_1 L = 4.73$, $\beta_2 L = 7.80$ and $\beta_3 L = 10.99$. The resulting deformed shapes and first derivatives are shown in Fig. 4.3.

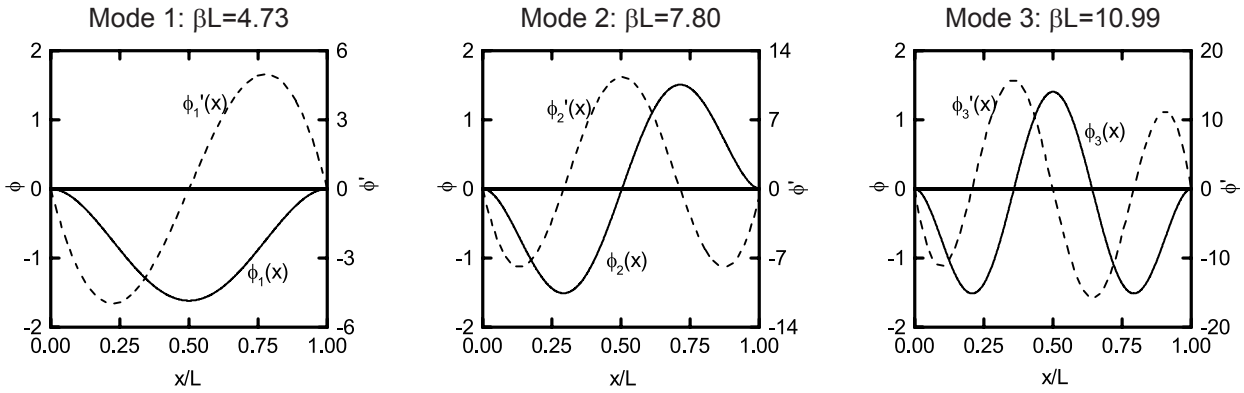

Figure 4.3. Mathematically predicted deformed shapes and first derivative for the first three resonance modes of a clamped-clamped beam.

4.2.1 Electromechanical coupling of DETF

A beam of length L, width b and height h as shown in Fig. 4.4 is considered for the determination of the coupling parameters η_1 and η_2. The electric field is applied by patterned electrodes across the height direction and drives the piezoelectric deformation in the width direction. For this purpose, the drive electrode areas are placed on one half of the beam. The generated charges from the mechanical deflection are picked up by patterned sense electrodes on the other half of the beam.

[1]This derivation is widely available and thus not specifically given in this dissertation. An excellent derivation can be found in Appendix A.1.2 of [74].

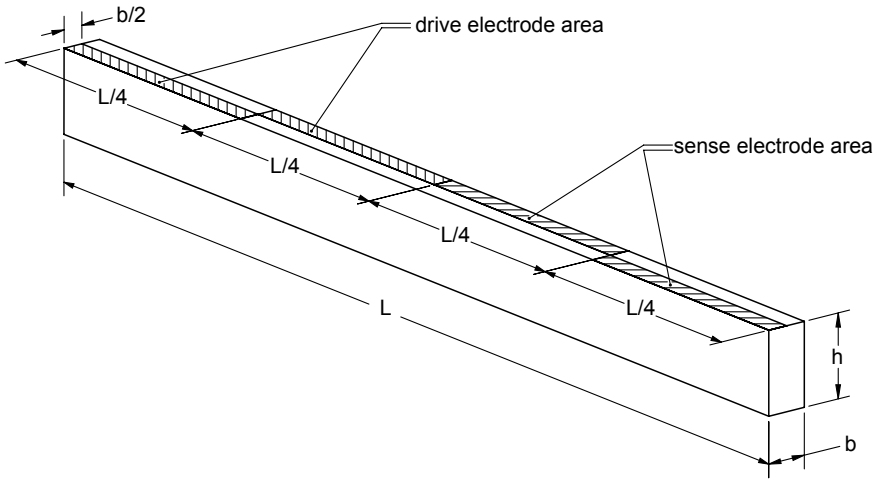

Figure 4.4. Schematic view of piezoelectrically actuated and sensed DETF beam with geometric dimensions and electrodes (areas with hatching).

The point at which the electrode areas switch from one side in the width direction to the other side is set at $L/4$, which is close to the inflection point for Mode 1 in Fig. 4.3.[2] The generalized force generated by the piezoelectric actuation can be calculated by integrating the product of distributed load and deformed shape function over the length of the beam:

$$F_1 = \int_0^L F(x)\,\phi(x)\,\mathrm{d}x \tag{4.14}$$

The distributed load can be calculated from the moment caused by the piezoelectric actuation. This moment is caused by the drive electrode in the half width below the neutral axis in the first $L/4$ of the beam and in half width above the neutral axis in the subsequent $L/4$ as shown in Fig. 4.4. The moment is defined as the integration of the product of line load and distance to neutral axis over the width. In this case, the line load is the product of piezoelectrically generated stress in the length direction T_1 and beam height h. These results can be summarized as:

$$M(x) = \begin{cases} h \int\limits_{-b/2}^{0} T_1 z\,\mathrm{d}z = \frac{-T_1 b^2 h}{8} & \text{for} \quad 0 < x < L/4 \\ h \int\limits_{0}^{-b/2} T_1 z\,\mathrm{d}z = \frac{T_1 b^2 h}{8} & \text{for} \quad L/4 < x < L/2 \end{cases} \tag{4.15}$$

$$M(x) = \frac{T_1 b^2 h}{8}\, f(x) \tag{4.16}$$

$$f(x) = \big(-1 + 2u(x - L/4) - u(x - L/2)\big) \tag{4.17}$$

$$u(x - x_0) = \begin{cases} 1 & \text{for} \quad x > x_0 \\ 0 & \text{for} \quad x < x_0 \end{cases} \tag{4.18}$$

[2] For a detailed discussion on the electrode geometry optimization for piezoelectric DETF see [75].

The conversion from applied voltage V_1 to piezoelectric stress T_1 can be done using Hooke's law, the piezoelectric constitutive equation with the assumption that no external stress is applied and the definition of the electric field in the height direction of the beam E_3 as it is applied with the patterned drive electrodes:

$$\text{Hooke's law:} \quad T_1 = E_{AlN}\, S_1 \Rightarrow M(x) = \frac{S_1 E_{AlN} b^2 h}{8} f(x) \tag{4.19}$$

$$\text{Constitutive equation:} \quad S_1 = \cancelto{0}{s_1 T_1} + d_{31} E_3 \Rightarrow M(x) = \frac{d_{31} E_3 E_{AlN} b^2 h}{8} f(x) \tag{4.20}$$

$$\text{Electric field definition:} \quad E_3 = \frac{V_1}{h} \Rightarrow M(x) = \frac{d_{31} V_1 E_{AlN} b^2}{8} f(x) \tag{4.21}$$

Where, d_{31} is the piezoelectric coefficient converting a voltage in the 3-direction (height of the beam) to a stress in the 1-direction (length of the beam). Using the definition of the distributed moment $m(x)$ and distributed load $F(x)$ the generalized force from Eq. (4.14) can be written as:

$$m(x) = \frac{\mathrm{d}M(x)}{\mathrm{d}x} = \frac{d_{31} V_1 E_{AlN} b^2}{8} f'(x) \tag{4.22a}$$

$$F(x) = \frac{\mathrm{d}m(x)}{\mathrm{d}x} = \frac{d_{31} V_1 E_{AlN} b^2}{8} f''(x) \tag{4.22b}$$

$$F_1 = \frac{d_{31} V_1 E_{AlN} b^2}{8} \int_0^L f''(x)\phi(x)\mathrm{d}x \tag{4.22c}$$

The first derivative of the function $u(x - x_0)$ is the Dirac-delta $\delta(x - x_0)$ and the second derivative is the unit-doublet $\delta_{-1}(x - x_0)$. Using an integration property of the unit-doublet the generalized force can be calculated:

$$F_1 = \frac{d_{31} V_1 E_{AlN} b^2}{8} \int_0^L \Big(2\delta_{-1}(x - {}^L\!/_4) - \delta_{-1}(x - {}^L\!/_2)\Big)\phi(x)\mathrm{d}x \tag{4.23a}$$

$$\int_{-\infty}^{\infty} g(\tau)\delta_{-1}(t - \tau)\mathrm{d}\tau = g'(t) \Rightarrow F_1 = \frac{d_{31} V_1 E_{AlN} b^2}{8}\Big(2\phi'({}^L\!/_4) - \phi'({}^L\!/_2)\Big) \tag{4.23b}$$

Finally, the input coupling coefficient can be determined:

$$\eta_1 = \frac{F_1}{V_1} = \frac{d_{31} E_{AlN} b^2}{8}\Big(2\phi'({}^L\!/_4) - \phi'({}^L\!/_2)\Big) = -1.23\frac{d_{31} E_{AlN} b^2}{L} \tag{4.24}$$

The derivation of the coupling coefficient η_2 at the output port of the DETF is similarly straight forward. It begins with the definition of the harmonic output current as the integration of the piezoelectric charges D_3 generated in the sense electrode areas multiplied by $j\omega$:

$$I_2 = j\omega \iint_{A_{se}} D_3\, \mathrm{d}A = j\omega\left(\int_{L/2}^{3L/4}\int_0^{b/2} D_3\, \mathrm{d}z\mathrm{d}x + \int_{3L/4}^{L}\int_{-b/2}^{0} D_3\, \mathrm{d}z\mathrm{d}x\right) \tag{4.25}$$

Using the second constitutive equation with the assumption of a zero impedance load (short circuit) at the output, Hooke's law and the definition of the local strain as the second derivative of the local displacement $d(x)$ multiplied by the distance from the neutral axis, the current can be written as:

$$\text{Constitutive equation:} \quad D_3 = d_{31} T_1 + \varepsilon \cancelto{0}{E_3} \Rightarrow I_2 = j\omega d_{31} \iint_{A_{se}} T_1 \, \mathrm{d}A \tag{4.26a}$$

$$\text{Hooke's law:} \quad T_1 = E_{AlN} S_1 \Rightarrow I_2 = j\omega d_{31} E_{AlN} \iint_{A_{se}} S_1 \, \mathrm{d}A \tag{4.26b}$$

$$\text{Local stress definition:} \quad S_1(x,z) = d''(x) z \Rightarrow I_2 = j\omega d_{31} E_{AlN} \iint_{A_{se}} d''(x) z \, \mathrm{d}A \tag{4.26c}$$

Performing the integration in the beam width direction according to Eq. (4.25) yields:

$$I_2 = j\omega \frac{d_{31} E_{AlN} b^2}{8} \left(\int_{L/2}^{3L/4} d''(x) \, \mathrm{d}x - \int_{3L/4}^{L} d''(x) \, \mathrm{d}x \right) \tag{4.27}$$

The local displacement is the product of general displacement and the deformed shape function. This result can be used to rewrite the current:

$$d(x) = Z\phi(x) \Rightarrow d'(x) = Z\phi'(x) \Rightarrow d''(x) = Z\phi''(x) \tag{4.28a}$$

$$I_2 = j\omega \frac{d_{31} E_{AlN} b^2 Z}{8} \left(\int_{L/2}^{3L/4} \phi''(x) \, \mathrm{d}x - \int_{3L/4}^{L} \phi''(x) \, \mathrm{d}x \right) = j\omega \frac{d_{31} E_{AlN} b^2 Z}{8} \Big(\left[\phi'(x)\right]_{L/2}^{3L/4} - \left[\phi'(x)\right]_{3L/4}^{L} \Big) \tag{4.28b}$$

The electromechanical coupling at the output axis using the definition in Eq. (4.10) can now be calculated:

$$\eta_2 = \frac{1}{j\omega} \frac{I_2}{Z} = \frac{d_{31} E_{AlN} b^2}{8} \Big(2\phi'(3L/4) - \phi'(L/2) - \phi'(L) \Big) = 1.23 \frac{d_{31} E_{AlN} b^2}{L} = -\eta_1 \tag{4.29}$$

It can be seen that due to the chosen configuration of the electrodes the coupling coefficients at the input and output are equal in magnitude and opposite in sign.

4.2.2 Electromechanical coupling of TBTF

The calculation of the electromechanical coupling coefficients η_1 and η_2 for the TBTF is similar to that of the DETF. The electrode design for a single beam of a TBTF is shown in Fig. 4.5. The outer two quarters of the beam are used for the drive electrodes and the center half is used for the sense electrode. The main difference to the case of the DETF is that in the TBTF the displacement of the beam is in the same direction as the applied electric field. In this case the moment necessary for a beam deflection cannot simply be achieved by a specific electrode pattern on the beam. Instead, a bimorph must be created by applying the electric field only across one half

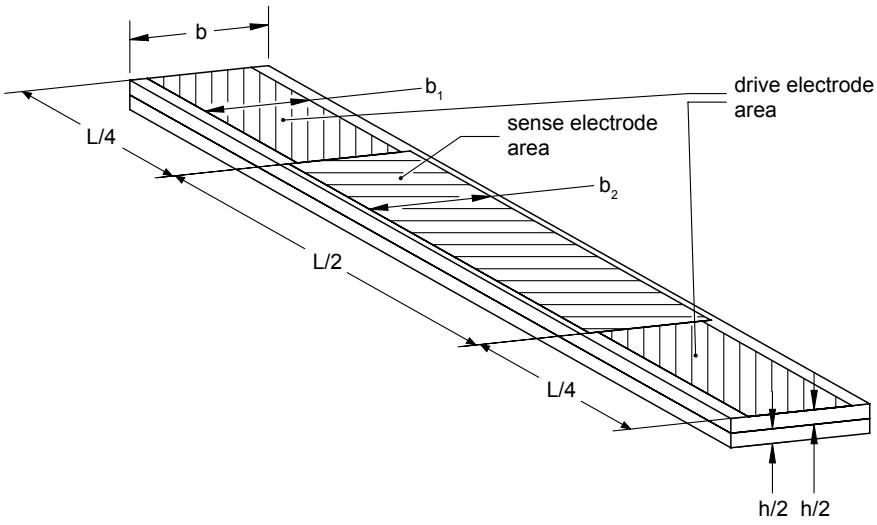

Figure 4.5. Schematic view of piezoelectrically actuated and sensed TBTF beam with geometric dimensions and electrodes (areas with hatching).

of the beam height. In the practical implementation this is done by placing a grounded electrode plane in between the two halves of the AlN layer. For this analysis, this center electrode is assumed to have zero thickness. The moment from piezoelectric strain in the upper half of the AlN caused by the drive electrode can be expressed as:

$$M(x) = b_1\, f(x) \int_0^{h/2} T_1 z \,\mathrm{d}z \tag{4.30a}$$

$$f(x) = 1 + u(x - {}^{3L}/_4) - u(x - {}^{L}/_4) \tag{4.30b}$$

Note that the width of the drive electrode b_1 is generally smaller than the beam width b. In the actual device the difference is caused by a small area that needs to be reserved for electrical connection to the sense electrode, which is bordered on both sides by the drive electrode areas. Using the same considerations as in Eq. (4.19)-(4.21) the moment can be rewritten as:

$$M(x) = \frac{b_1 h d_{31} V_1 E_{AlN}}{4} f(x) \tag{4.31}$$

Equations (4.22) and (4.23a) can be used to determine the generalized force generated by the TBTF drive electrodes:

$$F_1 = \frac{b_1 h d_{31} V_1 E_{AlN}}{4} \int_0^L f''(x)\phi(x)\,\mathrm{d}x = \frac{b_1 h d_{31} V_1 E_{AlN}}{4} \int_0^L \Big(\delta_{-1}(x - {}^{3L}/_4) - \delta_{-1}(x - {}^{L}/_4)\Big)\phi(x)\,\mathrm{d}x \tag{4.32}$$

The same identity as for Eq. (4.23b) can be used to get the input coupling coefficient for the TBTF:

$$\eta_1 = \frac{F_1}{V_1} = \frac{b_1 h d_{31} E_{AlN}}{4}\Big(\phi'({}^{3L}/_4) - \phi'({}^{L}/_4)\Big) = 2.46\frac{b_1 h d_{31} E_{AlN}}{L} \tag{4.33}$$

For the calculation of the electromechanical coupling at the output η_2, the piezoelectrically generated charge has to be integrated over the electrode area as it was done for the DETF:

$$I_2 = j\omega \int_{L/4}^{3L/4} \int_{0}^{b_2} D_3 \, \mathrm{d}z\mathrm{d}x \tag{4.34}$$

The same basic considerations are used as in Eq. (4.26) to rewrite the output current:

$$I_2 = j\omega d_{31} E_{AlN} \int_{L/4}^{3L/4} \int_{0}^{b_2} S_1 \, \mathrm{d}z\mathrm{d}x \tag{4.35}$$

In contrast to the DETF, the stress does not vary along the width direction of the beam, but it does vary linearly along the height direction. In order to achieve an averaged stress value that is only dependent on the length direction of the beam, the following calculation has to be made:

$$S_1(x) = \int_{0}^{h/2} d''(x) \frac{y}{h/2} \, \mathrm{d}y = \frac{h}{4} d''(x) = \frac{h}{4} Z\phi''(x) \tag{4.36}$$

Using this result and performing the trivial integration along the width direction of the beam the output current can be rewritten as:

$$I_2 = j\omega \frac{d_{31} E_{AlN} b_2 h Z}{4} \int_{L/4}^{3L/4} \phi''(x) \, \mathrm{d}x = j\omega \frac{d_{31} E_{AlN} b_2 h Z}{4} \left[\phi'(x)\right]_{L/4}^{3L/4} \tag{4.37}$$

Finally, using Eq. (4.10) the electromechanical coupling at the output port can be calculated:

$$\eta_2 = \frac{d_{31} E_{AlN} b_2 h}{4} \left(\phi'(3L/4) - \phi'(L/4)\right) = -2.46 \frac{d_{31} E_{AlN} b_2 h}{L} \tag{4.38}$$

It can be seen that for the case that the drive and sense electrodes are of the same width $b_1 = b_2$ the electromechanical coupling coefficients at the input and output have the same magnitude but opposite sign $\eta_1 = -\eta_2$.

4.2.3 Coupling comparison between DETF and TBTF

Design optimizations for DETF and TBTF sensors focus on maximizing coupling as well as sensitivity to the desired load while satisfying size and operating frequency constraints and ensuring sufficient robustness. In order to compare the coupling coefficients of DETFs and TBTFs they have to be expressed with the same parameters. Using the general definition for the resonance frequency, Eq. (4.6) and the expressions for the second moment of area, Eq. (4.7) and Eq. (4.8), geometric ratios for the DETF and TBTF can be calculated. For the DETF, the following ratio results:

$$\frac{b}{L} = \frac{\omega_1}{4.73^2} \sqrt{\frac{\rho}{E_{AlN}}} L \tag{4.39}$$

For the TBTF, the following ratio is calculated:

$$\frac{h}{L} = \frac{\omega_1}{4.73^2}\sqrt{\frac{\rho}{E_{AlN}}}L \tag{4.40}$$

These ratios can be inserted in the coupling expressions of the DETF, Eq. (4.24), and the TBTF, Eq. (4.33), respectively:

$$\eta_{1,DETF} = \frac{1.23}{4.73^2} d_{31}\sqrt{\rho E_{AlN}} bL\omega_1 \tag{4.41}$$

$$\eta_{1,TBTF} = \frac{2.46}{4.73^2} d_{31}\sqrt{\rho E_{AlN}} bL\omega_1 \tag{4.42}$$

It can be seen that the coupling for a TBTF with the same beam width and resonance frequency as a DETF is twice as strong.

4.2.4 Quality factor of tuning forks

One important parameter for the admittance calculation is the quality factor of the DETFs and TBTFs. The general definition of the quality factor Q of a system in resonance is:

$$Q = 2\pi \times \frac{\text{Energy stored}}{\text{Energy dissipated per cycle}} \tag{4.43}$$

The calculation of the amount of energy stored in the vibrating beam is straightforward if the mode shape, amplitude and frequency of vibration are known. However, the energy dissipation occurs in a multitude of ways and highly depends on the operating conditions. Examples of energy dissipation mechanisms in MEMS include air damping of a free vibrating structure and squeeze film damping if the structure is close to another surface. Furthermore, because of the elastic deformation energy is also dissipated in the structure itself in the form of thermoelastic damping [76]. Efforts have also been made to include the piezoelectric and pyroelectric contributions to the thermoelastic damping for materials such as AlN [77]. The overall Q can be calculated from the individual contributions Q_{air}, Q_{te}, etc. by:

$$\frac{1}{Q} = \frac{1}{Q_{air}} + \frac{1}{Q_{te}} + \dots \tag{4.44}$$

In many cases, the quality factor is dominated by one type of energy dissipation. For MEMS resonating beams at atmospheric pressure the air damping is typically the dominating effect. The analysis in this work will focus on this effect. A closed-form solution for the damping caused by air flow can be found for harmonically oscillating spheres. By modeling a rectangular beam as a chain of oscillating spheres, the generalized air damping can be written for the case of the DETF

and the TBTF [3]:

$$c_{DETF} = M\frac{3\pi\mu_{air}h + {}^{3}/_{4}\pi h^2\sqrt{2\rho_{air}\mu_{air}\omega_{1,DETF}}}{\rho_{AlN}h^2 b} \tag{4.45a}$$

$$c_{TBTF} = M\frac{3\pi\mu_{air}b + {}^{3}/_{4}\pi b^2\sqrt{2\rho_{air}\mu_{air}\omega_{1,TBTF}}}{\rho_{AlN}b^2 h} \tag{4.45b}$$

Where M is the generalized mass from Eq. (4.4), h is the AlN thickness, b is the width of the tine, ρ_{AlN} is the density of AlN, μ_{air} is the dynamic viscosity of air and ρ_{air} is the density of air. The resonance frequencies of the first mode of the DETF and the TBTF can be simplified from Eq. (4.5), Eq. (4.7) and Eq. (4.8):

$$\omega_{1,DETF} = 6.46\sqrt{\frac{E_{AlN}}{\rho_{AlN}}}\frac{b}{L^2} \tag{4.46a}$$

$$\omega_{1,TBTF} = 6.46\sqrt{\frac{E_{AlN}}{\rho_{AlN}}}\frac{h}{L^2} \tag{4.46b}$$

Equations (4.6), (4.45) and (4.46) can be combined to obtain Q_{air} expressions for the DETF and TBTF:

$$Q_{air,DETF} = 6.46\sqrt{E_{AlN}\rho_{AlN}}\frac{h^2b^2}{L^2}\frac{1}{3\pi\mu_{air}h + {}^{3}/_{4}\pi h^2\sqrt{2\rho_{air}\mu_{air}\omega_{1,DETF}}} \tag{4.47a}$$

$$Q_{air,TBTF} = 6.46\sqrt{E_{AlN}\rho_{AlN}}\frac{h^2b^2}{L^2}\frac{1}{3\pi\mu_{air}b + {}^{3}/_{4}\pi b^2\sqrt{2\rho_{air}\mu_{air}\omega_{1,TBTF}}} \tag{4.47b}$$

Note that the TBTF consists of one center beam and two side beams. The latter are typically half as wide as the former resulting in a higher Q for side beams individually. However, as a first estimate it suffices to use the width b of the center beam for the Q factor calculation, since the overall system Q is dominated by the worst individual contributor to the damping as discussed above. In Fig. 4.6, the effect of the beam length, width and thickness on Q_{air} for the DETF and TBTF is shown. The length is varied in the typical range of MEMS resonant beams of 200 to 400 µm. The thickness is varied between 0.5 and 4 µm, which is assumed to be the thickness range in which highly c-axis oriented AlN with controllable stress can be deposited in the current deposition tool (see Chapter 2). The width is varied as to achieve the desired frequency range of 100 kHz to 1 MHz. It can be seen that for a given frequency, Q_{air} for both the DETF and the TBTF can be improved by increasing the beam length. In order to optimize Q_{air} for the DETF, the thickness should also be increased, which does not affect the frequency. The beam width results from the chosen combination of resonance frequency and beam length. For the case of the TBTF, it is the the thickness that results from the chosen combination of resonance frequency and beam length. If the optimization of Q_{air} is the sole purpose, the width should be minimized for the TBTF case. In general it can be seen that the expected Q for the DETF at comparable resonance frequency, length and thickness is larger than for the TBTF. If, for example, an AlN film thickness of 2 µm and a resonance frequency of 500 kHz is chosen, the achievable Q_{air} is around 700 for the DETF and around 200 for the TBTF.

[3] The derivation of this result is outside of the scope of this dissertation. Very good discussions and experimental evaluations of this result can be found in [78] and [79].

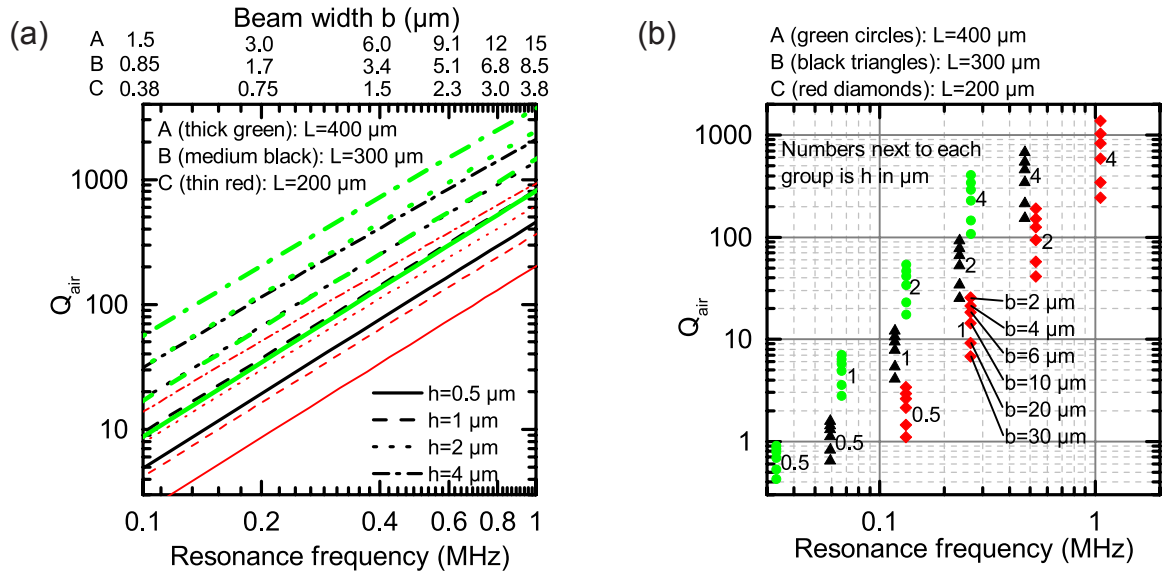

Figure 4.6. Calculated quality factor as a function of resonance frequency, beam width and beam length for (a) double-ended tuning forks and (b) triple-beam tuning forks.

4.3 Equivalent circuit model

The DETFs and TBTFs in this work are all 2-port devices, i.e. they have an input port at which the drive voltage is supplied and an output port at which the sense current is measured. The admittance calculated in Section 4.2 is the ratio between drive voltage and sense current. It is a complex number with amplitude and phase, both of which are functions of frequency. Besides the theoretically derived model it is also useful to have a model that employs circuit elements as equivalent parameters to the physical properties of the system. The resonators have both electrical and mechanical components with coupling in between the two domains. However, the behavior of the system can be described with a simple electrical circuit diagram using the conversion in Table 4.1. The 2-port resonator equivalent circuit can be expressed in two ways. The more intuitive

Table 4.1. Equivalent circuit parameters

Mechanical domain			Electrical domain		
force	F	N	voltage	v	V
displacement	x	m	charge	Q	C
velocity	$\dot{x}$	m/s	current	i	A
mass	m	kg	inductance	L	H
damping	b	kg/s	resistance	R	Ω
spring compliance	$\frac{1}{k}$	m/N	capacitance	C	F
elements (springs, dampers) in parallel			impedances in series	$Z_1 + Z_2 + \ldots$	
elements (springs, dampers) in series			impedances in parallel	$\left(Z_1^{-1} + Z_2^{-1} + \ldots\right)^{-1}$	

way is shown in Fig. 4.7a. Transformers are used for the electromechanical coupling from the

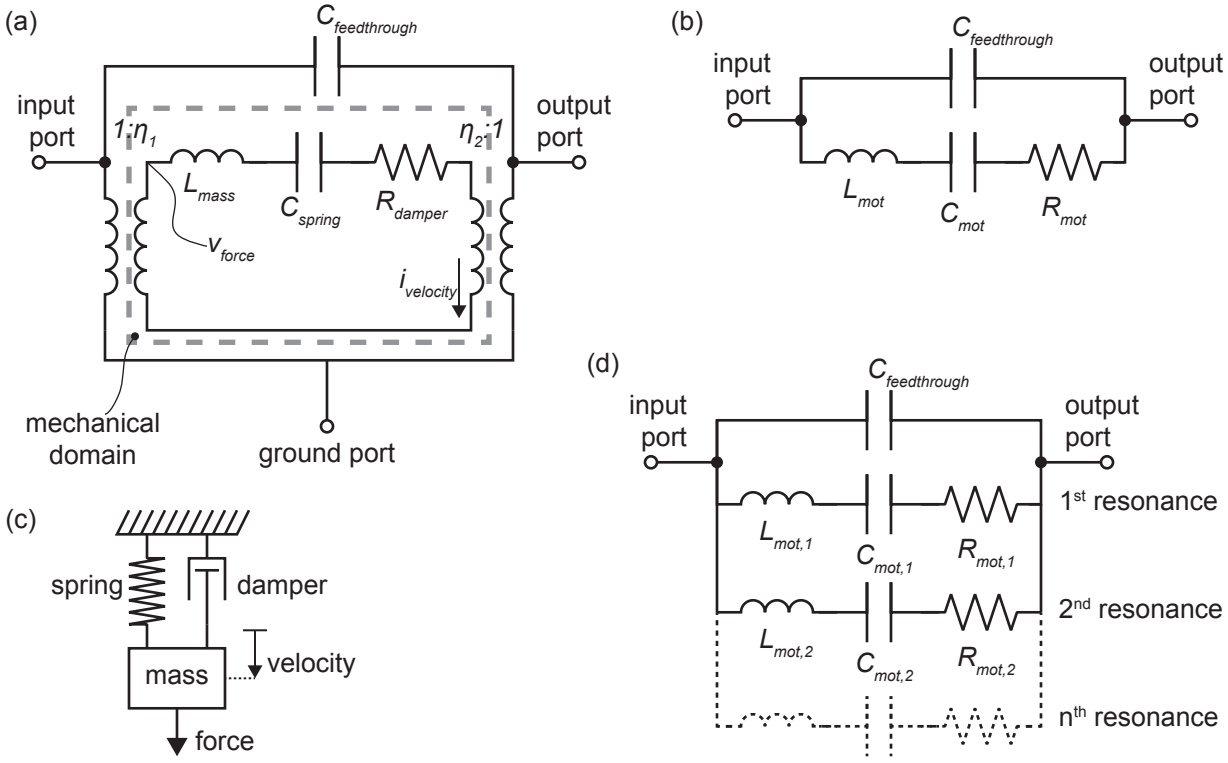

Figure 4.7. Equivalent circuit models of a piezoelectric tuning fork resonator. (a): Complete model including the transduction between electrical and mechanical domains. (b): Simplified model with motional inductance, capacitance and resistance. (c): Mechanical equivalent model. (d): Simplified model expanded to include any number of resonance modes.

input voltage to the drive force ($1 : \eta_1$) and from the velocity to the output current ($\eta_2 : 1$). In this case, the values of the circuit elements in the mechanical domain are the physical quantities, e.g., the inductance L_{mass} is the actual generalized mass of the vibrating beams as defined in Eq. 4.4. This model provides a good physical understanding of the resonator operation and the interplay between individual parameters. However, a simplified model is often preferred for deriving equivalent LCR-parameters from an experimental measurement and for comparing the parameters to those of different resonator types. The simplified model as shown in Fig. 4.7b consists of a series connection of motional inductance, motional capacitance and motional resistance in parallel to a feed through capacitance that directly connects the input and output ports. In this model the motional parameters do not directly represent physical properties in the resonator, but they are useful parameters to evaluate the resonator's performance. The parameters can easily be derived from a system's measured impedance behavior by means of curve-fitting with *Matlab*-code. DETFs and TBTFs have many resonance frequencies as shown in Section 4.2 and the equivalent circuits presented so far only represent the behavior in the frequency range close to a single resonance peak. By including several LCR-branches in parallel the model can be expanded to represent the system behavior in a wider frequency range as shown in Fig. 4.7d. This expansion is usually only helpful when the resonance frequencies are close together and the Q-factor is low enough to cause significant overlap of the resonance peaks. For the TBTF the 2nd, 3rd and 4th modes as shown in Fig. 4.2 have very similar resonance frequencies. The measured device impedance amplitude and phase for a TBTF are shown in Fig. 4.8. Two resonance peaks at 420.25 and 424.75 kHz can

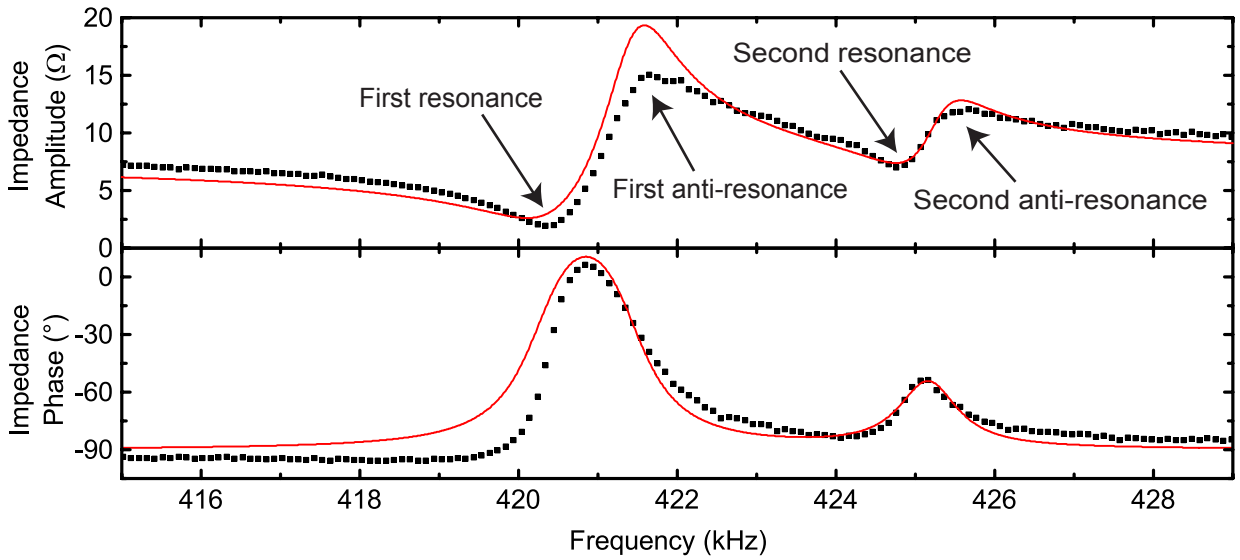

Figure 4.8. Impedance amplitude and phase for a TBTF. Black squares are experimental results and red line is fitted result of equivalent circuit simulation.

be observed. The free software tool *LTSpice IV* was used to simulate the equivalent circuit from Fig. 4.7d for two resonance peaks. The equivalent circuit parameters were modified until the best possible match between experimental results and simulation results was achieved. The resulting equivalent circuit parameters as shown in Table 4.2 can then be used to simulate the resonator

Table 4.2. Extracted motional parameters for the impedance simulation in Fig. 4.8

LCR-branch	Parameter	Symbol	Value
branch 1	motional inductance	$L_{mot,1}$	500 H
	motional capacitance	$C_{mot,1}$	287 aF
	motional resistance	$R_{mot,1}$	3 MΩ
branch 2	motional inductance	$L_{mot,2}$	3000 H
	motional capacitance	$C_{mot,2}$	46.7 aF
	motional resistance	$R_{mot,2}$	16 MΩ
both	feed through capacitance	$C_{feedthrough}$	50 fF

behavior as part of a more complex electrical circuit, for mechanical design optimization of the resonator and for performance prediction when the resonator is used as sensing element.

4.4 Characterization of MEMS tuning forks

The electrical characterization of the fabricated DETF and TBTF devices is the first and most critical testing step. The sensing mechanism is based on tracking resonance frequency changes due to the application of the mechanical signal. Therefore, it is critical to measure the resonance frequency reliably and with high accuracy.

4.4.1 Impedance measurement

The suitability of the resonator can be judged from the frequency-dependent complex admittance or impedance, which is typically plotted in the form of a Bode plot, i.e. with separate y-axes for amplitude and phase and a common x-axis for frequency. A typical instrument to measure the impedance of MEMS resonators is a network analyzer. This instrument has a drive port, which outputs a sinusoidal signal at discrete frequency steps that are swept over a desired range and compares the measured voltage at a sense port to a reference port, which is typically connected to the drive port. Since the piezoelectric output port of the DETF and TBTF devices can be seen as an alternating current (AC) source, a transimpedance amplifier must be used to convert the current to a voltage for the network analyzer input channel. The setup is shown schematically in Fig. 4.9a for the example of a TBTF. A photograph of the laboratory implementation is shown in Fig. 4.9b. The instrument on the upper left is a *Hewlett Packard 4195A* network analyzer. The device under test (DUT) is a TBTF packaged as shown in Fig. 3.3a. The printed circuit board (PCB) is mounted in the left of the two metal boxes on the table and the transimpedance amplifier is mounted in the box to the right. The insides of the two boxes are shown in Fig. 4.10a and b, respectively. The transimpedance amplifier is made with surface mount technology (SMT) components on a PCB that was developed as a universally configurable pre-amplifier board with up to four channels of two-stage amplifiers or up to two channels of four-stage amplifiers. Its circuit diagram is shown in

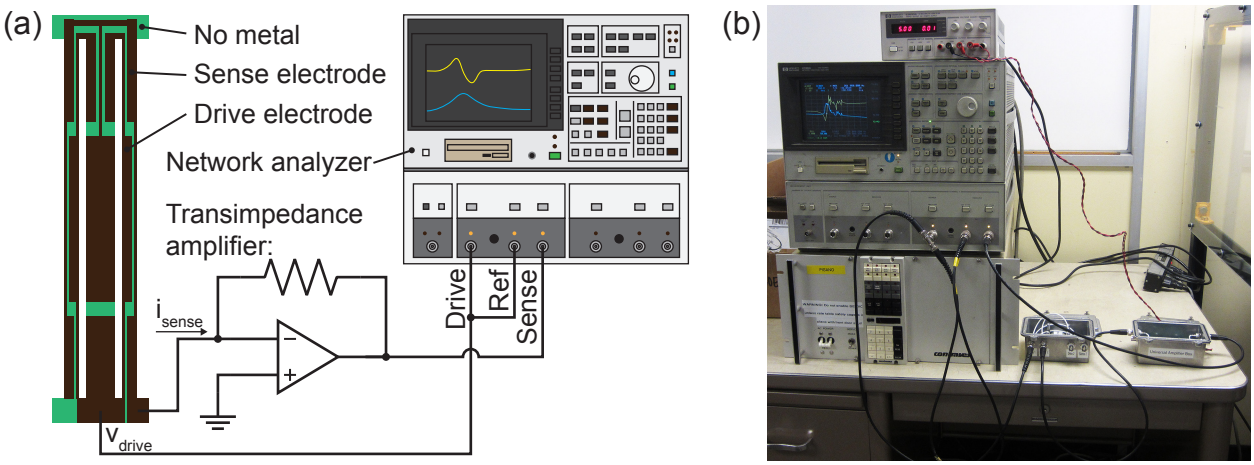

Figure 4.9. Experimental setup for electrical impedance characterization. (a): Schematic drawing of a TBTF with patterned electrodes connected through a transimpedance amplifier to a network analyzer. (b): Photograph of the network analyzer (left), test box for device (small box in middle) and amplifier box (small box on right).

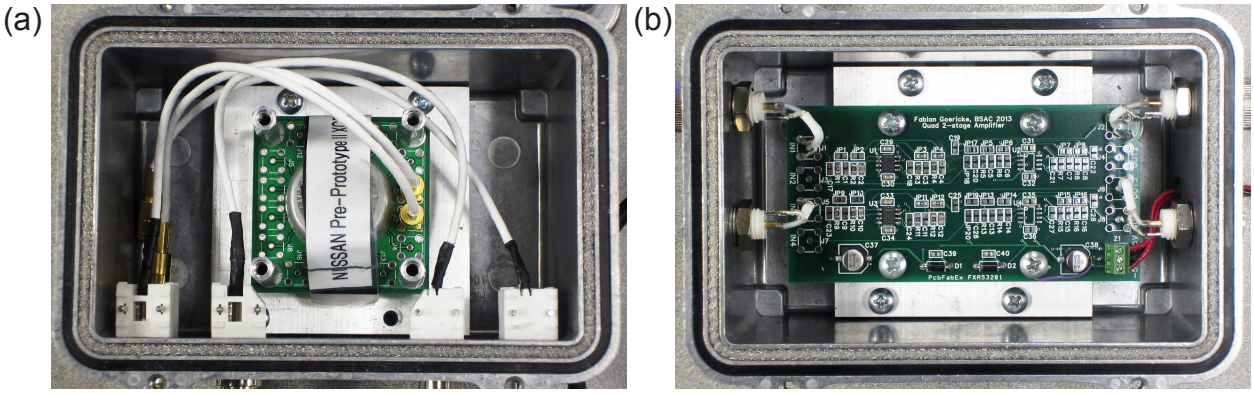

Figure 4.10. Top view of shielded boxes for device testing. (a): Box with tuning fork device mounted inside. (b): Box with configurable amplifier circuit set up for transimpedance amplification mounted inside.

Appendix C. During the impedance measurement the boxes are closed with lids to achieve optimal shielding against electromagnetic interference (EMI). A typical impedance spectrum of a TBTF is shown in Fig. 4.11. For some applications, oscillator circuits as described in the following sec-

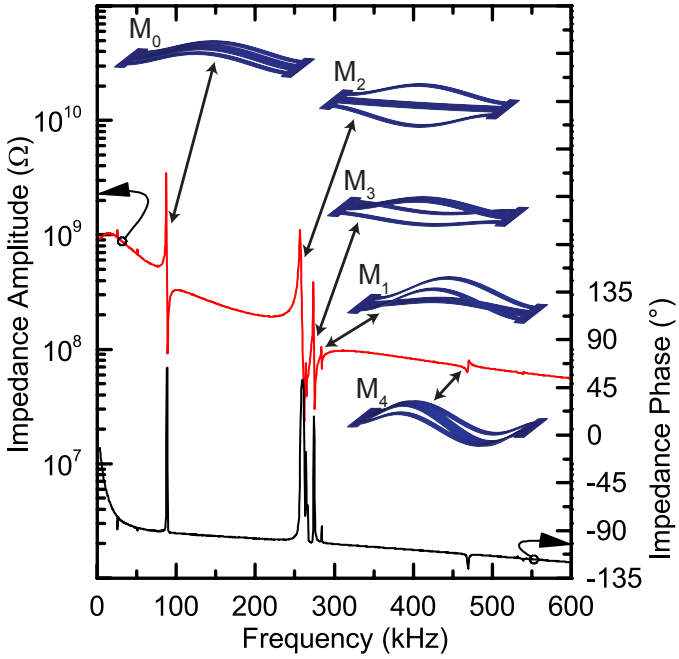

Figure 4.11. Measured impedance spectrum of a TBTF. Mode shapes from FEM analysis are shown next to their respective resonance peaks.

tion cannot be used. Instead the resonance frequencies have to be extracted from the impedance spectrum, e.g., using the *MATLAB* script in Appendix D.

4.4.2 Oscillator operation

In order to track the resonance frequency shift of the tuning fork devices an oscillating circuit has to be built. The block diagram of a simple linear oscillator is shown in Fig. 4.12a. The details about electric oscillators with frequency references such as quartz crystals, or in this case aluminum nitride tuning forks, can be found in many literature sources. The circuit is based on an amplifier, whose output if fed back into its input through some sort of feedback network. When the amplification A is chosen correctly the circuit oscillates at the frequency at which the feedback network has an admittance peak, e.g., the resonance peak of the MEMS tuning fork. Alternatively, a *Zurich Instruments HF2* lock-in amplifier can be used to operate the tuning forks at specific resonance peaks. For this purpose, the tool can first be used to measure the impedance spectrum of the MEMS device. Then, a built-in digital phase-locked loop (PLL) can be enabled to lock to a specific resonance peak. A simplified block diagram of this PLL is shown in Fig. 4.12b. The phase relation of the signal output from the tuning fork relative to the output of the oscillator gets measured by the phase detector. Then, a proportional-integral-derivative (PID) controller is used

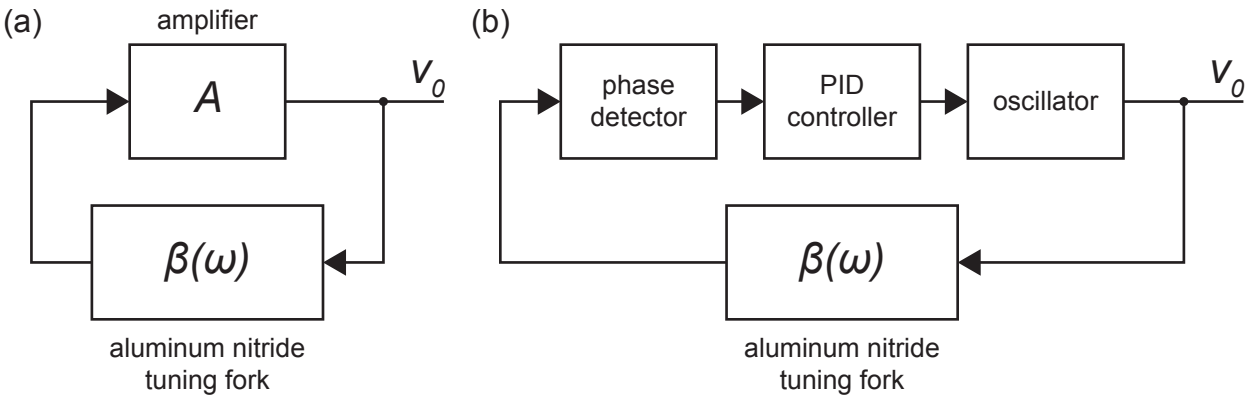

Figure 4.12. Block diagrams of drive circuits for aluminum nitride tuning forks. (a): Linear oscillator circuit. (b): Digital phase-locked loop.

to modify the oscillator frequency, such that the phase relation approaches the desired value. In this instrument, the phase relation and the parameters of the PID controller can be selected in the software interface. Since the same phase relation can occur at several different resonance peaks as shown in Fig. 4.11 the approximate resonance frequency and the range of allowed frequencies for the oscillator can also be configured. This measurement setup is very convenient for fast laboratory measurement of many MEMS resonators with very different impedance spectra. It is also possible to use two PLLs at the same time, e.g., for differential measurement in accelerometers as described in Section 4.5.3.

4.5 Mechanical sensing with MEMS tuning forks

The purpose of the DETF and TBTF devices discussed in this chapter is the detection of physical signals. In the following sections, two different approaches are shown to use these types of devices for the detection of acceleration. In section 4.5.1, the conventional approach for tuning fork sensors will be introduced, in which the detected change in resonance frequency is a direct result of the axial stress in the tuning fork beams from the inertial force of a proof mass. In section 4.5.2, a new approach developed in this doctoral research will be presented, which does not rely on the axial stresses in the beams, but on the geometric deformation of the beams due to an applied moment by a proof mass.

4.5.1 Stress-based sensing

The resonance frequency of an axially loaded beam differs from the unloaded resonance frequency. A tensile load increases the resonance frequency, which is the equivalent of the higher pitch of a guitar string when it is tightened. For the clamped-clamped MEMS beams of both the DETF and TBTF the conditions to apply the Euler-Bernoulli equation are satisfied, i.e. the length

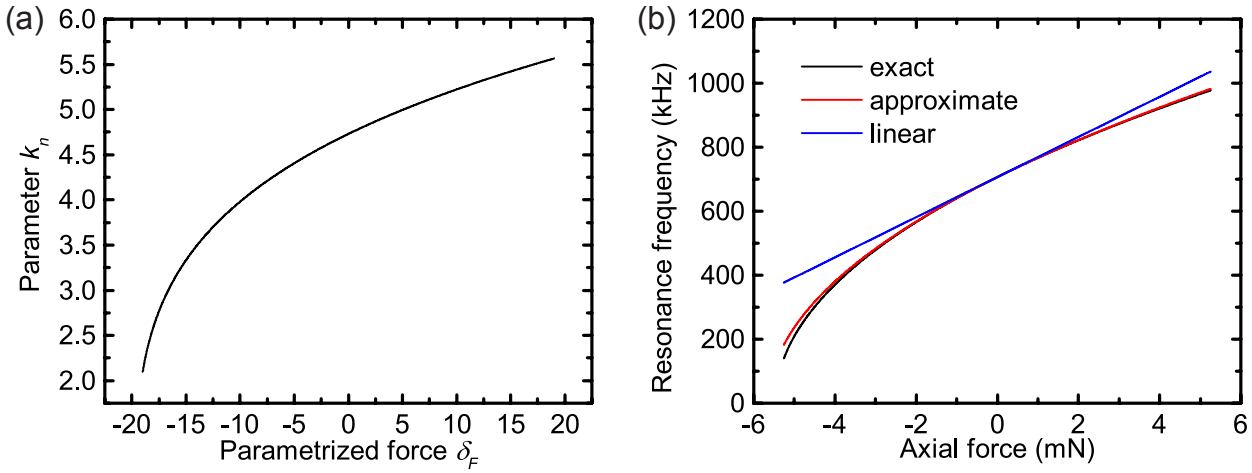

Figure 4.13. (a): Mathematically derived parameter k_n necessary for calculation of stress-based frequency shift in tuning forks over parametrized force δ_F. (b): Resonance frequency over axial force as calculated from the exact, approximate and linear equations.

is sufficiently greater than both the width and the thickness. For the dynamic, i.e. time-dependent, deflection $w(x,t)$ the inertial force has to be included and the Euler-Bernoulli equation can be written as:

$$\frac{\partial^2}{\partial x^2}\left(EI\frac{\partial^2 w(x,t)}{\partial x^2}\right) - F_N\frac{\partial^2 w(x,t)}{\partial x^2} + \rho A\frac{\partial^2 w(x,t)}{\partial t^2} = 0 \tag{4.48}$$

Here, the second and third terms represent the contributions to the distributed force by the applied axial force and the inertial force, respectively. Using the clamped-clamped boundary conditions $w(0,t) = w'(0,t) = w(L,t) = w'(L,t) = 0$, the resonance frequencies of the beam can be determined by finding the periodic solution of the corresponding homogeneous equation[4]. The resulting resonance frequencies are given by:

$$f_n(\delta_F) = \frac{1}{2\pi}\sqrt{\frac{EI}{\rho AL^4}}k_n^2(\delta_F) \tag{4.49}$$

Where $k_n(\delta_F)$ has to be determined numerically for the parametrized force δ_F given by:

$$\delta_F = \frac{L^2}{EI}\frac{F_N}{2} \tag{4.50}$$

Figure 4.13a shows the relationship between δ_F and k_1, which applies to the first resonance mode. Equation (4.49) is not very practical due to the nature of the parameter k_n. However, it has been shown that expanding the complicated expression for k_n at $\delta_F = 0$ the following simplified expression can be found, which is very accurate for $\delta_F < 6$ [81, 82]:

$$f_n(\delta_F) = \frac{1}{2\pi}\sqrt{\frac{EI}{\rho AL^4}}k_n^2(0) \times \sqrt{1 + \frac{1}{6}\gamma_n\delta_F} \tag{4.51}$$

[4]This derivation can be found in many references and is not reproduced in detail in this dissertation. A good treatment of the subject matter can be found in [80].

Where $\gamma_1 = 0.2949$. Further simplification can be achieved by linearizing Eq. (4.51) at $F_N = 0$ and the resonance frequency can be written as:

$$f_n(F_N) = \frac{1}{2\pi}\sqrt{\frac{EI}{\rho AL^4}}k_n^2(0) \times \left(1 + \frac{\gamma_n}{24}\frac{L^2}{EI}F_N\right) \tag{4.52}$$

The linearized relative frequency shift due to the stesses caused by an applied axial force for the first resonance mode of the clamped-clamped beam can then be expressed as:

$$\frac{\Delta f_1}{f_1} = \frac{f_1(F_N) - f_1(0)}{f_1} = 0.01229\frac{L^2}{EI}F_N \tag{4.53}$$

In Fig. 4.13b, the accuracy of the simplified expressions is compared to the exact equation for a typical in-plane vibrating MEMS beam with L, b and t of 300 µm, 6 µm and 2µm, respectively. For this case, the approximate solution is accurate to within 1% for a force range of -3.13 to +9.57 mN, which represents a resonance frequency range of 467 kHz to 1.15 MHz. For the linearized equation, 1% of accuracy is achieved for a force range of -1.33 to +1.75 mN or a frequency range of 617 to 808 kHz. Forces applied by a proof mass in response to an acceleration are generally much smaller than this range as will be shown later in this chapter. For DETFs and TBTFs, Eq (4.53) can be rewritten in terms of their geometric dimensions as defined in Fig. 4.4 and Fig. 4.5, respectively. Using the expression for the second moment of inertia from Eq. (4.7) and the fact that the axial force applied to a DETF gets transfered in equal parts in each tine the relative frequency shift for the DETF can be written as:

$$\left.\frac{\Delta f_1}{f_1}\right|_{DETF} = \frac{f_1(F_N) - f_1(0)}{f_1} = 0.07374\frac{L^2}{Eb^3h}F_N \tag{4.54}$$

For the TBTF case it is assumed that the outer tine width is half of the inner tine width b. In this case, the TBTF can be treated like two beams of width b vibrating out-of-plane as the effect of the outer tines is additive and the force gets transfered to each tine proportional to the tine width. Using the second moment of inertia equation from Eq. (4.8) the relative frequency shift for the TBTF can be written as:

$$\left.\frac{\Delta f_1}{f_1}\right|_{TBTF} = \frac{f_1(F_N) - f_1(0)}{f_1} = 0.07374\frac{L^2}{Ebh^3}F_N \tag{4.55}$$

For the experimental verification, a chip containing several AlN DETFs was solder-bonded to a steel parallel as described in Section 3.3.2. The steel parallel was clamped at one end and a defined deflection was applied at the other end. The deflection was measured using a dial indicator. For the calibration of the strain experienced at the MEMS chip's top surface a second steel parallel was prepared. A blank silicon dummy chip of the same dimensions as the MEMS chip was solder-bonded to this parallel and a commercially available metal foil strain gauge of type Vishnay CEA-06-062UW-350 was attached to this dummy chip using Vishay M-Bond 610 epoxy. Figure 4.14a shows the setup schematically, a scanning electron microscope (SEM) image of the AlN DETF with its placement on the MEMS die and a photograph of the commercial strain sensor with its placement on the dummy die. The metal foil strain gauge is made from the alloy constantan with a gauge factor (ratio of relative resistance change to mechanical strain) of 2.145±0.5%. The

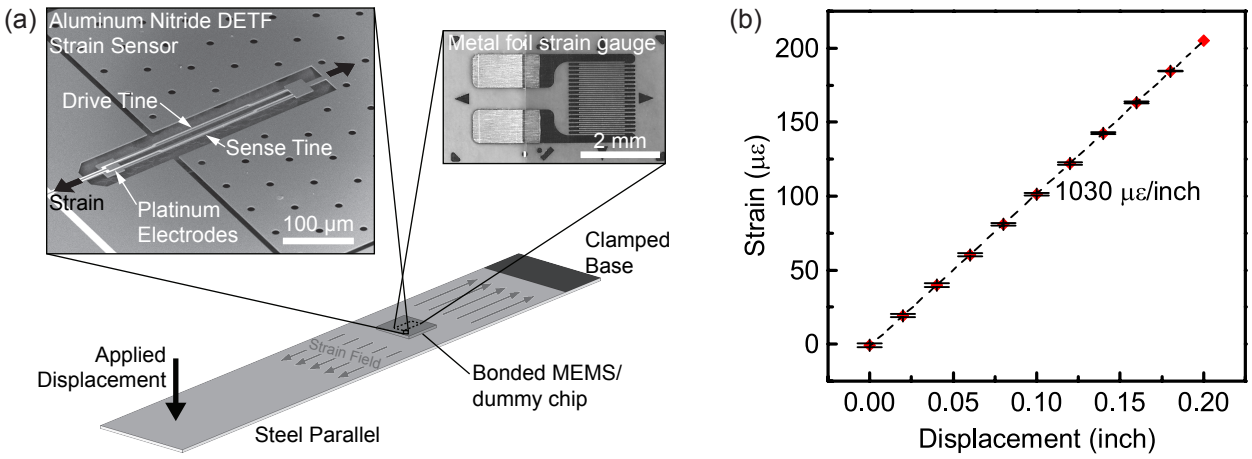

Figure 4.14. (a): Measurement setup for strain sensitivity characterization of a DETF bonded to a steel parallel; insets show an SEM image of the DETF (left) and a photograph of a metal foil strain gauge for a reference setup (right). (b): Strain measured by metal foil strain gauge over applied displacement, error bars show the range of measured values for four measurement runs.

resistance change of the strain sensor was mesaured using a Wheatstone bridge with three external resistors and a supply voltage of 2 V. The relationship of strain to applied displacement is shown in Fig. 4.14b and it can be seen that it is highly linear with a slope of 1030 $^{\mu\varepsilon}/_{\text{inch}}$ and repeatable[5]. The strain is measured at the top surface of the silicon chip and assuming that the thin AlN layer does not affect the mechanical behavior the same amount of strain is present in the released DETF. Since the deformations are small, the mechanical strain in this section is considered to be the engineering strain:

$$\varepsilon = {}^{\Delta L}/_{L} \tag{4.56}$$

For the conversion of strain to force in the tuning fork it is convenient to first determine the overall axial stiffness of the tuning fork consisting of the two tethers, two anchors and two tines. The tines are parallel which means that their stiffnesses add, while they are in series to the other parts of the DETF thus reducing the stiffness. The dimensions as defined in 4.1 are given in Table 4.3. The overall axial stiffness of the DETF is given by:

$$k_{DETF} = \left(\frac{1}{k_{te}} + \frac{1}{k_{an}} + \frac{1}{2}\frac{1}{k_{ti}} + \frac{1}{k_{an}} + \frac{1}{k_{te}} \right)^{-1} \tag{4.57}$$

$$k_{te} = \frac{w_{te}t}{l_{te}} E_{AlN} \quad k_{an} = \frac{w_{an}t}{l_{an}} E_{AlN} \quad k_{ti} = \frac{w_{ti}t}{l_{ti}} E_{AlN} \tag{4.58}$$

The force in the DETF can be expressed as a function of the DETF's dimensions and the applied strain by combining Equations (4.56), (4.57) and (4.58):

$$F_{DETF} = k_{DETF}\Delta L = \left(\frac{2w_{te}}{l_t e} + \frac{2w_{an}}{l_a n} + \frac{w_{ti}}{2l_t i} \right)^{-1} \frac{l_{DETF}}{tE_{AlN}} \varepsilon \tag{4.59}$$

[5]Strain is a dimensionless quantity. The unit $\mu\varepsilon$ (micro-strain) is commonly used for measurements with strain gauges and simply represents the number 10^{-6}.

Table 4.3. Dimensions of DETF used for strain sensing

Element	Dimension	Symbol	Value (μm)
DETF	length	l_{DETF}	420
	thickness	t	2
Tether	length	l_{te}	30
	width	w_{te}	8
Anchor	length	l_{an}	30
	width	w_{an}	32
Tine	length	l_{ti}	300
	width	w_{ti}	6

Each tine of the DETF experiences half of the total force:

$$F_{ti} = \frac{1}{2} F_{DETF} \tag{4.60}$$

For the dimensions from Table 4.3 the ratio of axial force in each tine to applied strain is 6.11 μN. A linear oscillator circuit as described in Section 4.4.2 is used in combination with a frequency counter to detect the frequency shift of the DETF while the deflection of the steel parallel is varied. The strain is increased in six steps from 0 $\mu\varepsilon$ to 30.9 $\mu\varepsilon$ and then decreased in the same step size back to 0 $\mu\varepsilon$. Data is averaged at a sampling rate of 0.5 Hz for five minutes at each step to improve the accuracy of the sensitivity calculation. The measurement raw data is shown in Fig. 4.15a and the frequency shift relative to the unloaded resonance frequency is shown as a function of the tine force in Fig. 4.15b. The data for part b of the figure is taken from the ramp up, i.e. the

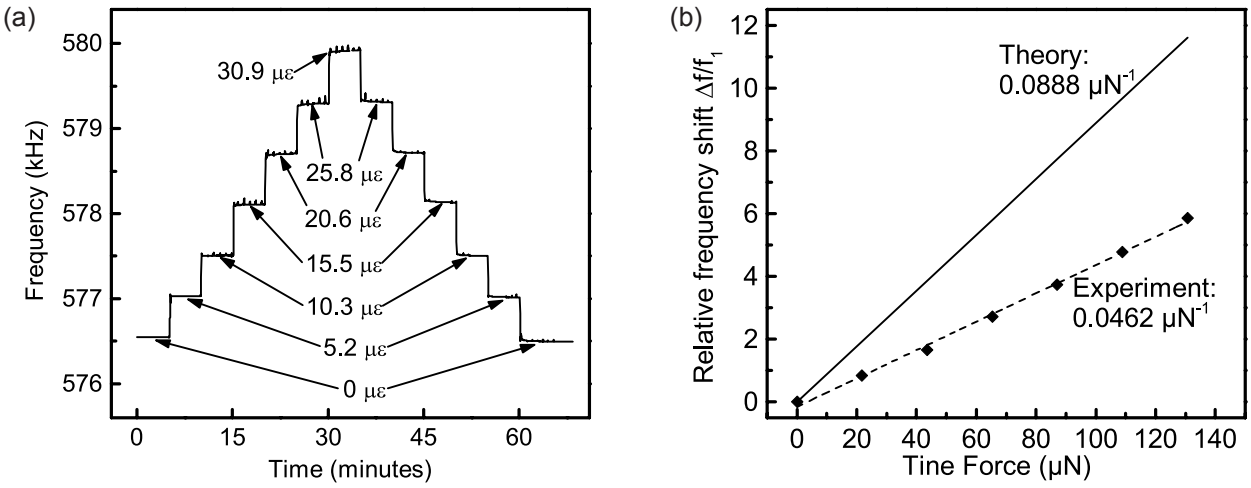

Figure 4.15. Results from strain sensitivity characterization. (a): Shift in resonance frequency of the DETF over time for the annotated values of applied strain. (b): Relative frequency shift over tine force calculated from the measurement results of the strain experiment compared to the theoretical behavior.

first 35 minutes of the experiment. The theoretical frequency shift based on Eq. (4.53) is also plotted in Fig. 4.15b. It can be seen that the experiemental sensitivity is about 48% lower than

the expected sensitivity. A possible reason for the error is the assumption that the strain in the top layer of AlN with etched cavities in the silicon chip underneath is identical to the strain at the top surface of the dummy silicon chip. Therefore, the actual axial force in the tine might be smaller than the calculated value. However, the experiment demonstrates the capability of the AlN DETFs as strain sensors bonded to steel parts with many potential industrial applications. An advantage over conventional strain sensors is the size of the sensing element that could allow very localized measurements of the strain or a strain distribution measurement with an array of such sensors.

Stress-based sensing of mechanical loads with DETFs works well if the applied axial forces are big as is the case for strain sensing applications. Due to the small deformations that are encountered in this method it can be very linear for a large sensing range. However, in many applications the applied forces are so small that the resulting frequency shifts are on the same order as the frequency variations in the DETF due to various noise sources, such as temperature variations and aging. In [74], accelerometers made with the surface-micromachining process are described. One device uses a proof mass with a surface area of 0.57 mm^2 clamped between two DETFs with tine length of 300 μm and tine width of 6 μm. This device achieved an acceleration sensitivity of only 3.5 Hz/g or 6.3 ppm/g. The temperature sensitivity, i.e. the unwanted frequency shift due to temperature fluctuations, of the same device is reported as 160 ppm/°C. The two DETFs of the accelerometer can be used in differential mode to reduce the temperature sensitivity because they react in the same way to a temperature change but with opposite signs to acceleration. However, even in this case, the temperature sensitivity could only be decreased to 2.5 ppm/°C, while the acceleration sensitivity doubles to 12.6 ppm/g. The resolution that can be expected from such devices is several orders of magnitude off from that of commercial MEMS accelerometers, which are currently able to resolve single mg-accelerations at bandwidths of 100 Hz[6]. Another AlN accelerometer reported in the same source achieves a factor of five increase in acceleration sensitivity by employing narrower tines and a leverage system to amplify the force applied by the proof mass. Even with these improvements the resolution is still several orders of magnitude off from a competitive level.

4.5.2 Theory for deformation-based sensing

The accelerometer described in the previous section consists of a proof mass, whose mass center is in line with the two DETFs that clamp it on either side to the substrate. This situation is shown schematically in Fig. 4.16a. Instead of the DETFs, TBTFs could equally be used as sensing elements. The axial force F caused by the proof mass m for the shown acceleration a follows from Newton's second law:

$$F = m \times a \tag{4.61}$$

As shown in the free-body diagram on the right hand side of the figure, one half of the force is applied to each of the DETFs/TBTFs with the left one being in compression and the right one being in tension for the described acceleration. One way to increase the acceleration sensitivity is by simply applying more force, i.e. creating a bigger proof mass. It is not desirable to significantly increase

[6]The Analog Devices ADXL103 is a single axis accelerometer with analog output, a measurement range of ±1.7 g, a packaged size of less than 5 mm^2 and a single unit price of US$ 16 at the time of printing. It has a typical noise floor of 110 $\mu g/\sqrt{Hz}$, i.e. a resolution of 1.1 mg at 100 Hz bandwidth [83].

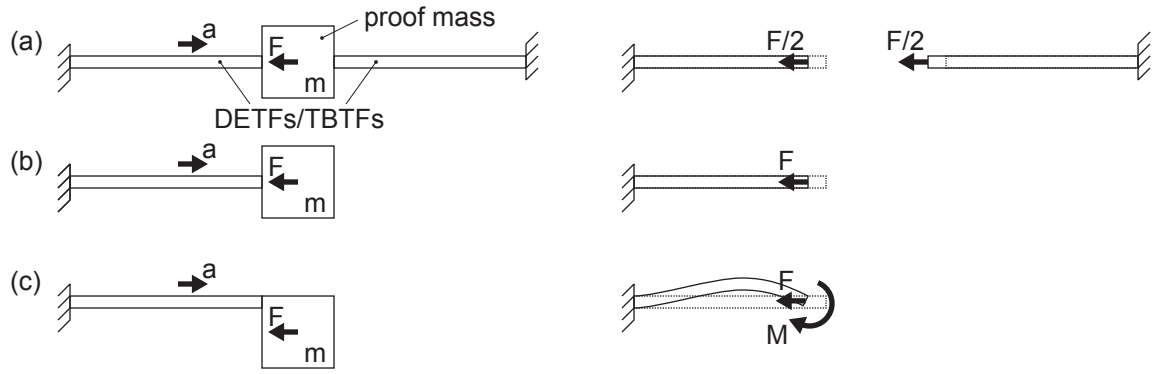

Figure 4.16. Free body diagram of accelerometers in (a) a clamped-clamped configuration with mass center in line with beams, (b) single clamped configuration with mass center in line with beam and (c) single clamped configuration with mass center offset from line of beam.

the footprint of the device because the cost per device would scale proportionally. Instead, the force can be increased by using the fabrication process from Section 3.2 to make the silicon substrate part of the proof mass. If the surface-micromachining process has to be used there are some advantages to creating a single-clamped device as shown in Fig. 4.16b. For a given proof mass the frequency change is equivalent to the differential frequency change of the two DETFs/TBTFs from part a. However, the effects of substrate strain, which can be caused by temperature change or external bending moments, are significantly reduced if the device is not clamped between two attachment points, but cantilevered freely. Therefore, the expected noise is lower and a better resolution can be achieved. The devices in Fig. 4.16a and b are essentially the same mechanical system in which stresses in the DETF/TBTF from the axial force of a proof mass cause a frequency change according to Eq. (4.53). By employing the surface- and bulk-micromachining process and using a cantilevered instead of a clamped-clamped device, a fundamentally different mechanical situation can be created as depicted in Fig. 4.16c. Since the center of mass of the proof mass is not in line with the DETF/TBTF and it is only attached on one side to the substrate, an acceleration causes both an axial force and a moment at the attachment point of the DETF/TBTF. It was discovered that the resulting bending of the DETF/TBTF beams, i.e. change in their geometries, causes a significantly larger shift in the resonance frequency than axial stresses in the beams resulting from the same proof mass and acceleration. This result termed deformation-based or bent-beam sensing is one of the major findings of this doctoral research. It is the subject of discussion for the rest of this section and preliminary results have been published in literature [84].

Due to the complicated, non-linear effect of beam-bending on the resonance frequency, finite element method (FEM) modeling with the software *ANSYS APDL Mechanical 14.0* is used to predict the device performance instead of developing a theoretical model. The FEM model of the chosen accelerometer design is shown in Fig. 4.17 using a DETF (a) and a TBTF (b). The specific shape of the proof mass is chosen such that four of these devices can be placed efficiently in a clover-like pattern with the proof masses pointing inwards allowing for a differential acceleration measurement in each of the two in-plane directions. For fabrication process reasons, the proof mass is designed to be smaller than the AlN area above it. This AlN-overhang of at least 10 μm as shown in the figure is necessary because of potential misalignment in the backside alignment

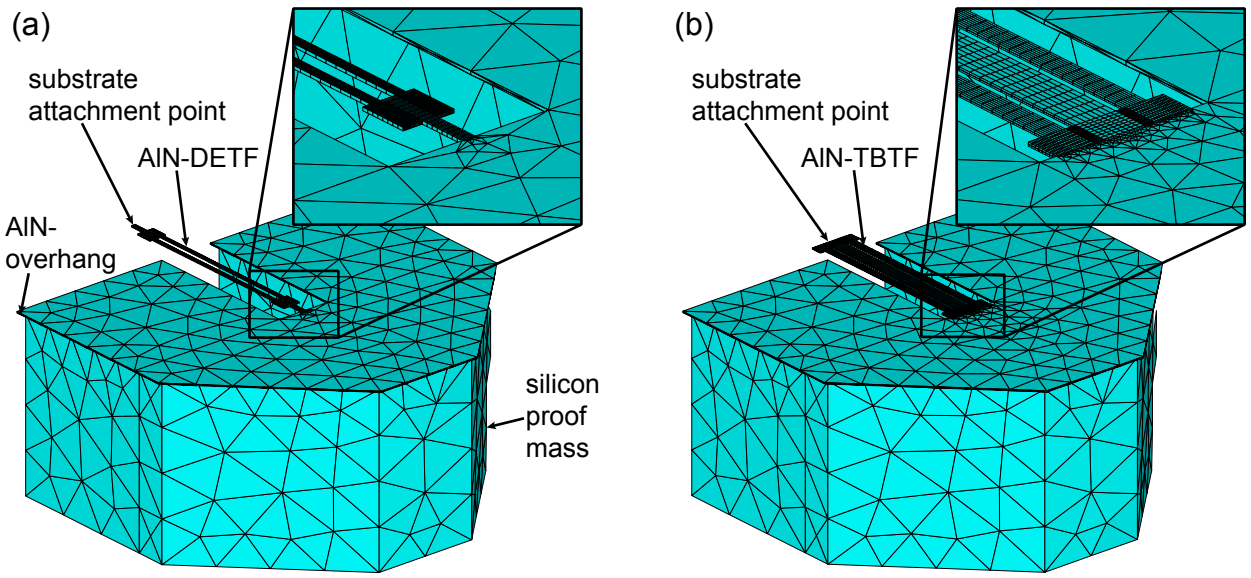

Figure 4.17. FE model of the accelerometer for bent-beam sensing with (a) DETF sensing element and (b) TBTF sensing element.

step of the surface- and bulk-micromachining process and not perfectly straight sidewalls during the Bosch process for the backside silicon etch. In the FEM model, only the DETF/TBTF is meshed with a fine mesh because the other elements are expected to have very little mechanical deformation and their main purpose is to create the forces and moments at the intersection of proof mass and DETF/TBTF. Since hexahedral (6-faced) brick-elements generally yield better results they are used for meshing the DETF/TBTF. The other areas, i.e. the proof mass and the AlN plate above it, are meshed with tetrahedral(4-faced) elements due to these elements' ability to create gradients from fine to coarse meshes and to easily mesh irregularly shaped volumes. Consequently, pyramid (5-faced) elements are used at the intersection of the DETF/TBTF and AlN plate to interface the hexahedrons with four nodes on each side to the tetrahedrons with three nodes on each side. Element type *solid186* is chosen for the entire model for several reasons. It is a higher order 3D-element with a mid-node on each edge, which is advantageous for elastic analyses. It can be used in the brick, tetrahedral and pyramid version and only uses the desired degrees of freedom for this mechanical analysis (the displacement in each of the three spatial coordinates), which is important to minimize analysis runtime. Most importantly, the element type supports definition of anisotropic material properties, which occur due to the wurzite-structure of the c-axis oriented AlN layer. The elastic constants for AlN are taken from literature [85]. For the proof mass, a thickness of 320 μm is chosen, which is a typical value for the surface- and bulk-micromachining process. The AlN thickness is set to 2 μm for both the DETF and TBTF case. In both cases, the tines are 300 μm long. The DETF tines are 6 μm wide and the center and side tines of the TBTF are 24 and 12 μm, respectively.

The FEM analysis is performed in two parts. First, an acceleration is applied to the entire model in the axial direction of the DETF/TBTF and the resulting internal stresses and deformations from the resulting inertial forces are calculated in an static, elastic analysis. In the second step, either the stresses or the deformations are transfered as input parameters for a modal analysis, which then

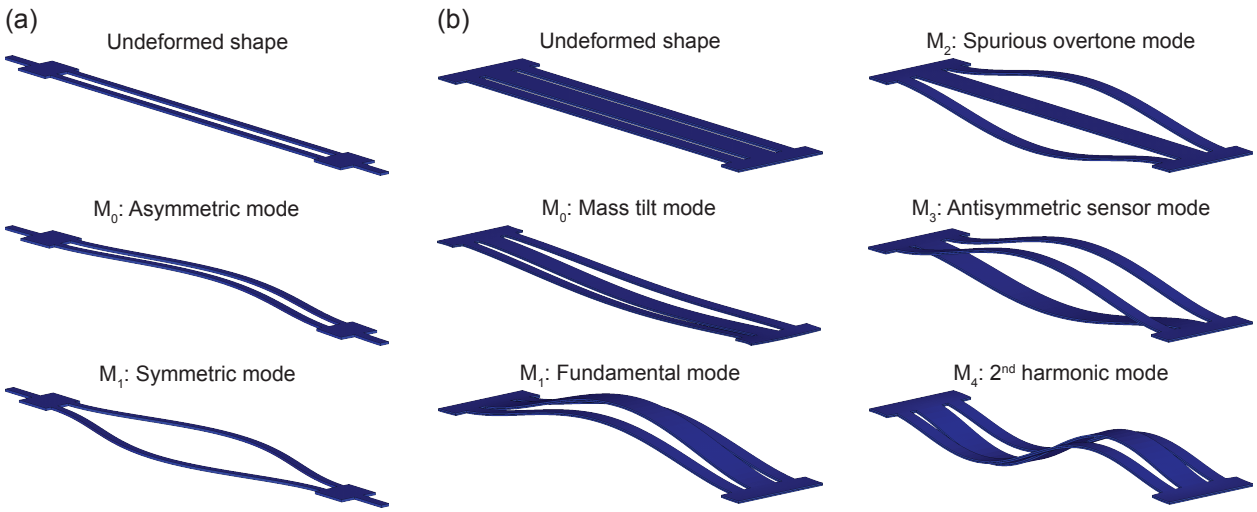

Figure 4.18. Mode shapes occurring in the accelerometer for bent-beam sensing with (a) DETF sensing element and (b) TBTF sensing element.

calculates the frequencies of several resonance modes of the structure. For this discussion, the relevant resonant modes of the DETF are the asymmetric and symmetric in-plane resonant modes shown in Fig. 4.18a. For the TBTF, the most likely resonant mode for sensor applications is the antisymmetric sensors mode, which is shown along with other mode shapes of similar frequencies in Fig. 4.18b[7]. By comparing the resonance frequency of the resonance mode that represents the driven mode shape of the DETF/TBTF to the frequency without applied acceleration the frequency shift and thus the acceleration sensitivity can be determined. For the first part of this procedure, two different cases are considered. In one case, the bottom side of the proof mass is confined to motions within its plane, thus preventing a reaction moment to be created and the DETF/TBTF from bending. The resulting internal stresses are transfered to the modal analysis using the *pstres* command. This case represents conventional stress-based sensing as in Fig. 4.16a and b. In the other case, the model is only clamped on the substrate side of the DETF/TBTF and thus free to deform including bending of the DETF/TBTF. The displacements at each node are added to the original nodal positions by using the command *upcoord* to create the new geometry of the model, which is then subject to the subsequent modal analysis. It was found that it is important for the static analysis that determines the deformation to include nonlinear geometry (command *nlgeom*) in order to yield the correct resonance frequencies in the modal analysis. As a consequence pre-stressed and pre-deformed results cannot be used at the same time because the software does not allow the usage of the *pstres* command with the results of a non-linear analysis. In practice, this limitation is not critical because the frequency shifts caused by beam bending are typically several

[7]All modes shown in the figure occur with very little or no movement of the proof mass. Other resonant modes with involvement of the large proof mass occur at much lower frequencies. These modes are not relevant for the actual sensing, but they do limit the bandwidth of the accelerometer. The names ”asymmetric” and ”symmetric” for the modes of the DETF are self-explanatory and taken from [74]. The names for the resonant modes of the TBTF are the same as used in [84]. In this paper, the author of this dissertation introduced the names for the ”mass tilt” and ”2nd harmonic” modes for TBTFs. The former name is given because a small tilting of the proof mass is actually part of the resonance mode and the latter name is self-explanatory. The names for the other three mode shapes were taken from [86].

orders of magnitude larger than those caused by axial stresses. The opposite case is true for the case of the confined proof mass motion. Here, the effect of the pre-stress significantly dominates the geometric effect, which is a very small change in length of the DETF/TBTF. Figure 4.19a shows the relative frequency shifts of the accelerometer based on deformation and stress using DETF and TBTF for an input acceleration range of -1 to +1 g. Several important observations about these results can be made. The frequency shift based on the axial stress varies linearly with input acceleration as expected. The simulation results for the frequency sensitivities of the DETF and TBTF are 9.80×10^{-4} and 2.00×10^{-4} g^{-1}, respectively. These results are in good agreement with the theoretical values of 9.86×10^{-4} and 1.92×10^{-4} g^{-1} from Eq. (4.54) and Eq. (4.55), respectively. In both cases, the deviation of the FEM solution from the analytical solution is smaller than 1 %, which is well within the accuracy expected for both models based on the simplifying assumptions. The second observation is that the frequency shift based on deformation is non-linear and for two cases significantly higher than the frequency shift based on stresses. Those two cases are the asymmetric mode of the DETF and the antisymmetric sensor mode of the TBTF. However, the symmetric mode of the DETF does not exhibit this very high change in resonance frequency. A closer inspection of the deformed mode shape for the bent beam due to the 1 g acceleration in comparison to the base mode shape reveals the reason for this phenomenon. Due to the nature of the deflection, the symmetric mode of the DETF remains completely within the (curved) plane as shown in Fig. 4.20a. For the asymmetric mode, the two tines of the DETF deflect out of the the curved plane in opposite directions, effectively converting the in-plane mode shape into a mixed in-plane and out-of-plane mode shape (Fig. 4.20b). Finally, the mode shape of the TBTF is naturally out-of-plane and thus does not undergo any significant change when the acceleration signal is applied (Fig. 4.20c). From these results, it can be concluded that resonating tuning forks can benefit from the large sensitivity of bent-beam sensing if the utilized mode shapes are either naturally out-of-plane mode shapes or become such as a result of the applied moment. However, it is conceivable that for a practical application the asymmetric mode of the DETF will be difficult to use. It can be expected that the fundamental change in the deformed mode shape has a profound effect on the electromechanical coupling and mechanical damping and thus make it difficult to integrate such a sensing element into an electromechanical system. Therefore, the TBTF is the most promising candidate to develop a mechanical sensor based on bent-beam sensing with large frequency sensitivity of the input signal, e.g., acceleration, and will thus be the subject of the remainder of this section.

Figure 4.19a showed that bent-beam sensing with a TBTF is non-linear. This fact in itself is not ideal, but it can be corrected with an appropriate circuit and/or software implementation. However, two problems remain, which cannot be easily accounted for. First, the relative frequency shift has a minimum at no applied acceleration, which means that the acceleration sensitivity goes to zero at this point. It is obvious that a usable accelerometer must maintain its sensing ability in the critical region when the acceleration goes to zero or changes its sign. The second problem is the y-axis symmetry of the frequency shift, which means that the magnitude of an axial acceleration, but not its sign can be sensed. This problem arises because bending the beam upwards has virtually the same effect as bending it downwards. It cannot be corrected for by using a second sensor pointing in the opposite direction and using the differential signal because both sensors would have the same output in either direction of the acceleration. The proposed solution to these problems is a deliberate shift of the frequency minimum away from the zero-acceleration point by applying

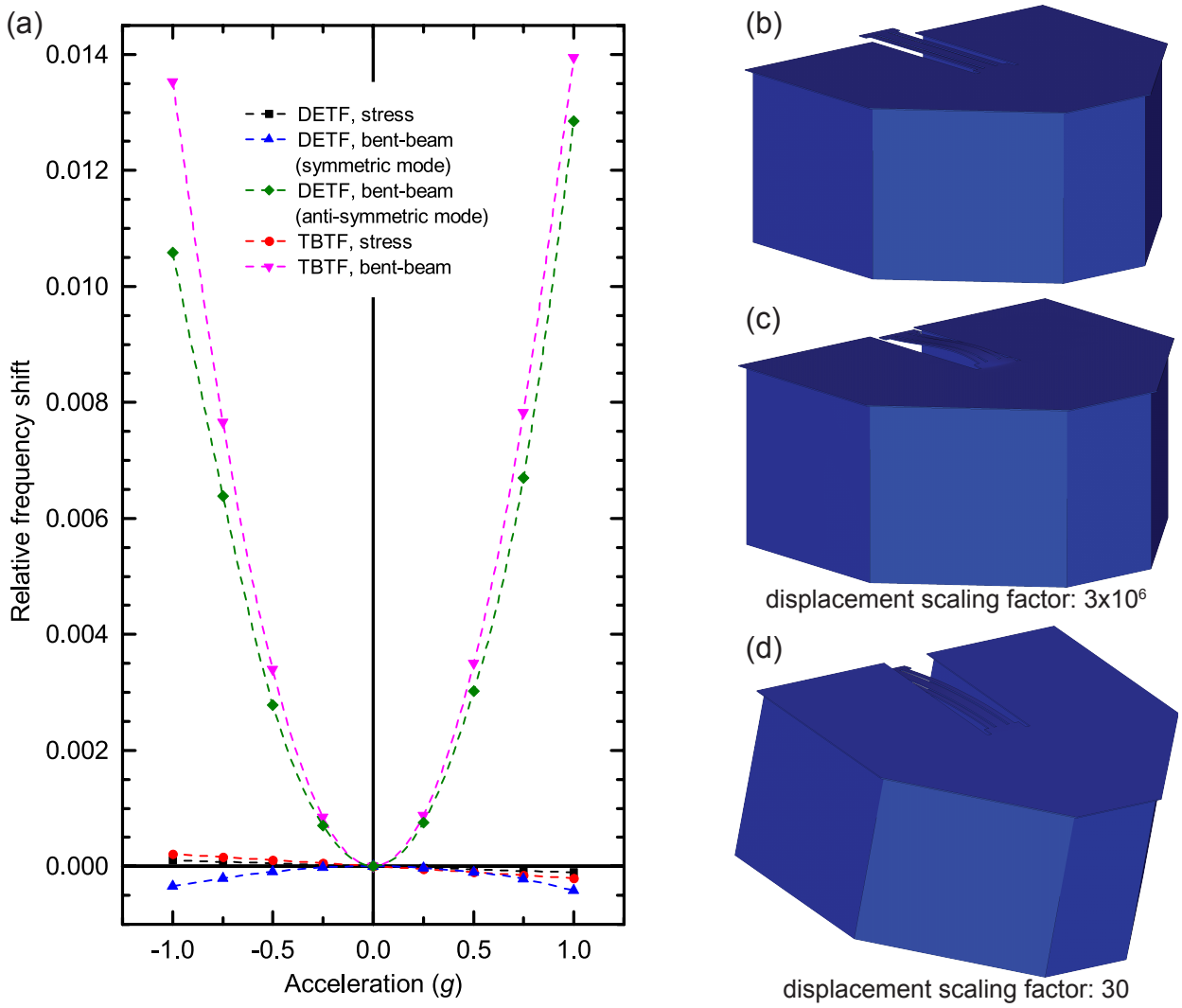

Figure 4.19. Results from FEM analysis of accelerometer. (a): Relative frequency shifts of different sensing elements operated in different sense modes over applied acceleration. (b): Undeformed shape of accelerometer. (c): Deformed shape for stress-based sensing case. (d): Deformed shape for bent-beam sensing case.

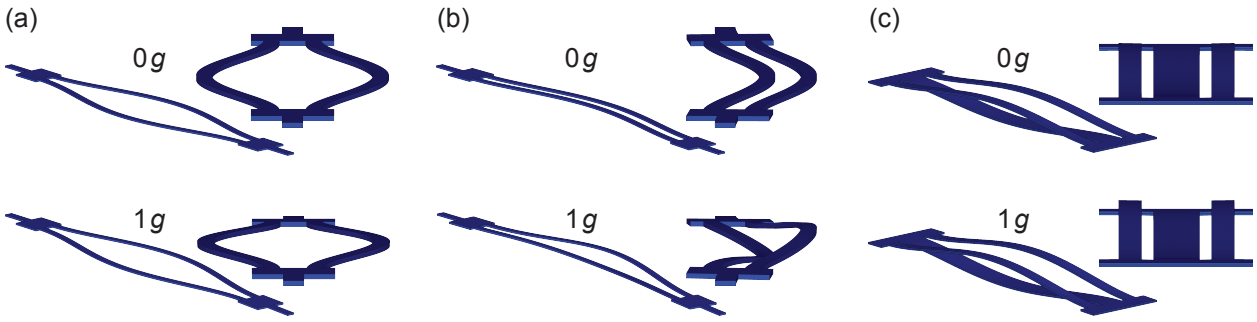

Figure 4.20. Deformed shapes at no acceleration and 1 *g* acceleration of (a) the DETF's symmetric mode, (b) the DETF's asymmetric mode and (c) the TBTF's antisymmetric sensor mode.

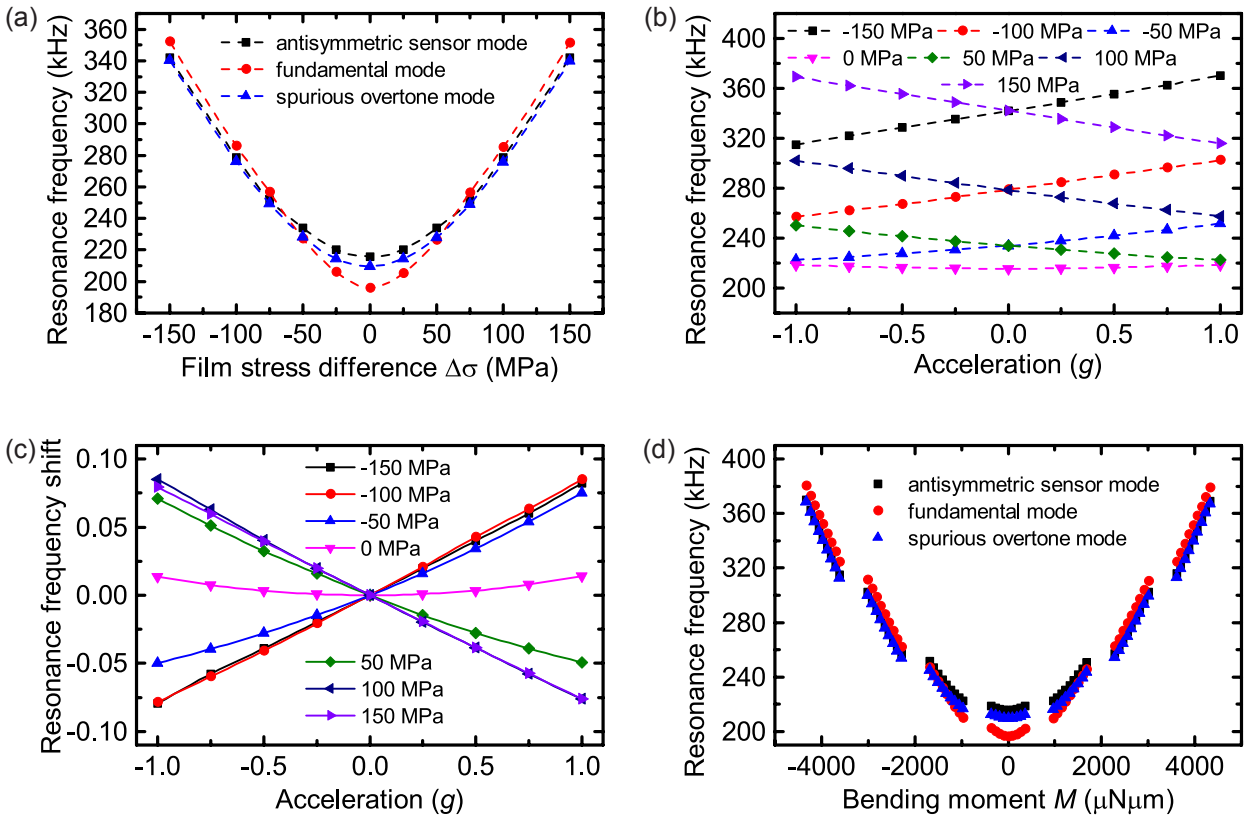

Figure 4.21. Results from FEM simulations with included stress difference between the two AlN layers. (a): Resonance frequency without applied acceleration over film stress difference for three modes of the TBTF. (b): Resonance frequency over acceleration for different film stresses. (c): Relative resonance frequency shift over acceleration at different stress differences. (d): Resonance frequency for three modes of the TBTF over bending moment calculated from stress difference and applied acceleration.

an offset moment that causes an initial deflection of the beam. Any subsequently applied moment from the acceleration signal would then either further bend the beam or act in the opposite direction to straighten the beam. As a result, the direction of the acceleration could be sensed and the acceleration sensitivity would not go to zero at the zero acceleration point but instead the zero crossing would happen outside of the desired range. An effective way to apply an offset moment controllably way is by tailoring the AlN deposition parameters as described in Chapter 2 such that the two AlN layers have different amounts of film stress. In order to predict the sensor behavior in this case, the film stresses are included in the first step of the FEM analysis, which calculates the deformed shape of the TBTF. The ANSYS command *inistate* is used to define two different stress values, equal in magnitude but opposite in sign, for the top and bottom AlN layers. The remainder of the FEM simulation is performed as described above. Figure 4.21a shows the effect of the applied stress difference $\Delta\sigma$ on the resonance frequencies of the TBTF without applied acceleration. The stress difference $\Delta\sigma$ is defined as the difference between applied film stress in the top AlN layer and the bottom AlN layer. When the top layer is under compression and the bottom layer is under tension, the value is negative and the beam is bending down. It can be seen that the beam moment

from the film stresses has a similar effect to the previously discussed moment from the proof mass under acceleration. In Fig. 4.21b, the resonance frequency shift for the antisymmetric sensor mode as a function of applied acceleration for different amounts of applied film stress is shown. A more clear picture emerges when the relative resonance frequency change due to acceleration is plotted (Fig. 4.21c). It can clearly be seen that pre-loading with the applied film stresses has the desired effect of shifting the frequency minimum away from the zero acceleration point. Furthermore, it can be seen that sensitivity and linearity of the sensor increase with increasing amount of applied film stress up to about $\Delta\sigma = 100$ MPa. Further increases of the film stress seem to have very little effect on the sensitivity. A simple theoretical model can be used to verify the assumption that the beam moment from either the proof mass or the film stresses is the driving force for the frequency change. The proof mass used in this simulation has a mass of 2.2695×10^{-7} kg and thus applies a force of 2.2256 µN for each g of acceleration assuming standard gravity of 9.80665 m/s^2. The vertical distance between the proof mass center and the center line of the beam is half of the proof mass thickness plus half of the beam thickness (161.25 µm). Consequently, the applied moment on the beam from the proof mass is equal to 2.2256 µN × 161.25 µm = 358.9 µNµm for each g of acceleration. Since a positive acceleration causes the beam to bend down and upward bending is defined as positive, the sign of this component of the total moment has to be negative. For the bending moment from the applied film stresses, the product of stress and distance to the neutral axis has to be integrated over the beam thickness and width. Since the film stresses are assumed to be constant in each half of the beam thickness, the integral can be split up and executed easily:

$$M_{\Delta\sigma} = b \int_{-h/2}^{h/2} \sigma(z) z \, \mathrm{d}z = b \int_{-h/2}^{0} \frac{-\Delta\sigma}{2} z \, \mathrm{d}z + b \int_{0}^{h/2} \frac{\Delta\sigma}{2} z \, \mathrm{d}z = b\Delta\sigma \frac{h^2}{8} \tag{4.62}$$

Here, the total width of all tines (48 µm) must be used for b and the thickness is 2.1 µm due to the two 1 µm-layers of AlN with the 0.1 µm electrode in between. Consequently, the total bending moment for the TBTF is:

$$M = -358.9 \, \frac{\mu\mathrm{N}\mu\mathrm{m}}{g} \times a + 26.46 \, \frac{\mu\mathrm{N}\mu\mathrm{m}}{\mathrm{MPa}} \times \Delta\sigma \tag{4.63}$$

where a is the applied acceleration and $\Delta\sigma$ is the applied film stress difference. In Fig. 4.21d, this conversion is done for the simulations introduced in the previous parts of the figure. It can be seen that the data is reasonably accurate and supports the model of offsetting the moment by applying film stresses. The reason for the data points not lying on perfect parabolas is most likely the limited accuracy of the theoretical equation for non-linear deformations. Equation (4.62) describes the bending moment from an axial acceleration and a film stress difference as the unifying factor to describe deformation-based sensing. This model is good to provide a fundamental understanding of the subject matter. In order to be useful for real applications, this model needs to be expanded to also account for the bending moment from the vertical component of the acceleration. Figure 4.22 shows a sideview of the beam with attached proof mass and the inertial forces acting on the mass center F_x and F_z resulting from the accelerations a_x and a_z, respectively. Note the definition of the right-hand coordinate system, the resulting positive direction of the moment and the definition of the beam deflection $w(x)$. The distances from the center of the clamped beam base to the mass center of the proof mass are shown as x_F and z_F for the x- and z-directions, respectively. The

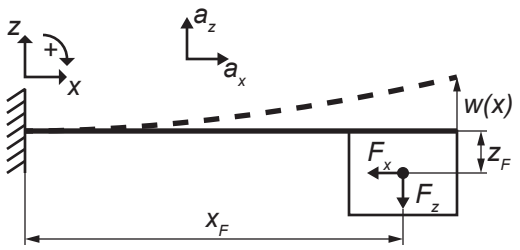

Figure 4.22. Geometric dimensions and axis definitions for the calculation of the bending moment from the applied film stress difference and acceleration.

total bending moment is the sum of the components from the applied stress difference $\Delta\sigma$ and the inertial forces $F_x = ma_x$ and $F_z = ma_z$:

$$M(x) = M_{\Delta\sigma} + M_{ax} + M_{az}(x) = -b\Delta\sigma\frac{h^2}{8} + ma_x z_F + ma_z(x_F - x) \tag{4.64}$$

The deflection $w(x)$ can be calculated using the Euler-Bernoulli beam equation:

$$-E^* I w''(x) = M \tag{4.65}$$

The customary way of writing the first derivative (angle) $w'(x) = \mathrm{d}w(x)/\mathrm{d}x$ and the second derivative $w''(x) = \mathrm{d}^2w(x)/\mathrm{d}x^2$ is used. The boundary conditions are zero deflection and zero angle at the clamping point $w(x = 0) = w'(x = 0) = 0$. The resulting deflection is:

$$w(x) = \frac{1}{E^* I}\left[\left(b\Delta\sigma\frac{h^2}{8} - m\left(a_x z_F + a_z x_F\right)\right)\frac{x^2}{2} + \frac{ma_z}{6}x^3\right] \tag{4.66}$$

Due to the geometry of the beams, the biaxial modulus $E^* = E/(1-\nu)$ must be used instead of the Young's modulus. The Young's modulus E and Poisson ratio ν were determined numerically from the elastic coefficients of AlN and their values are 346.1 GPa and 0.3193, respectively, resulting in a biaxial modulus E^* of 508.4 GPa.

4.5.3 Experimental results for deformation-based sensing

In the previous section, deformation-based sensing as a promising method for highly sensitive accelerometers was shown theoretically and with FEM simulation. However, experimental validation is critical to validate that the resonance modes of the bent TBTFs can be excited and to show how accurately the resonance frequency can be determined. A sensor with the same dimensions as used for the simulations in Fig. 4.19 was fabricated using the surface- and bulk-micromachining process described in Section 3.2. An SEM image of the sensor is shown in Fig. 4.23a. The dimensions of the sensor as defined in Fig. 4.1 and Fig. 4.22 are given in Table 4.4. The thickness of the proof mass was measured with an optical microscope by looking at the side of a proof mass that was removed from an adjacent sensor fabricated in the same process (Fig. 4.23b). A *Veeco Wyko NT 3300* white-light interferometer was used to measure the curvature of the actual sensor's TBTF

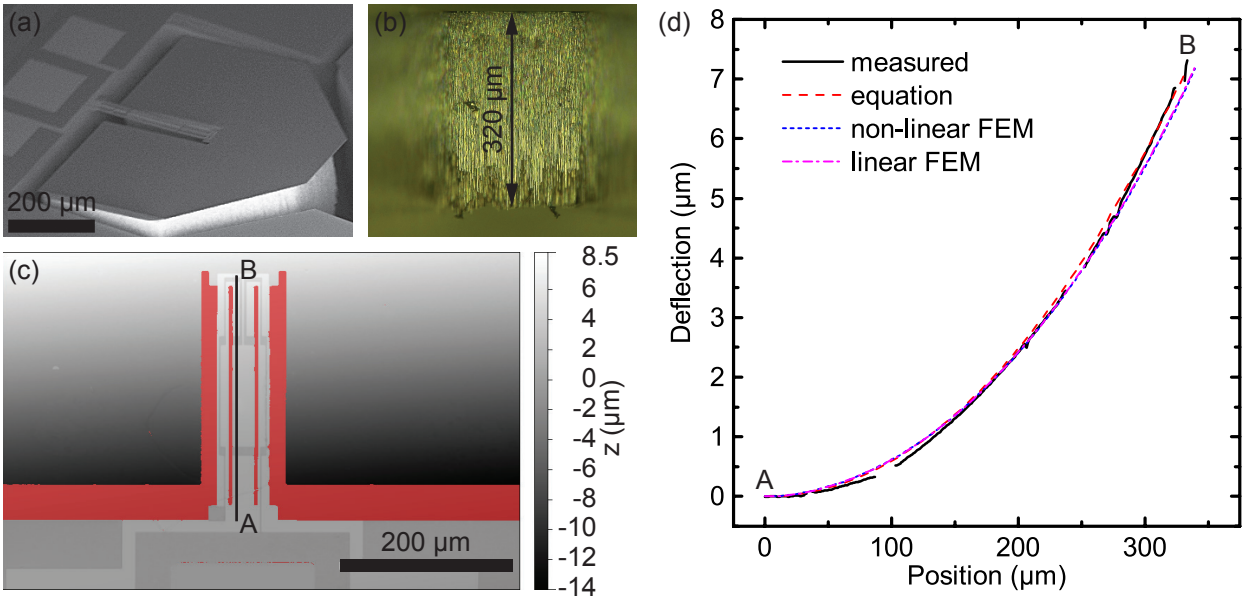

Figure 4.23. (a): SEM image of the accelerometer. (b): Optical micrograph of a proof mass (side view) for thickness measurement. (c): Contour plot of the z-axis displacement of the TBTF for characterization of the deformed shape along the path A-B. (d): Measured deformed shape of TBTF and fitted shapes from equation, non-linear FEM and linear FEM.

Table 4.4. Dimensions of TBTF used for accelerometer

Element	Dimension	Symbol	Value (μm)
TBTF	length	l_{TBTF}	340
	thickness	t	2.1
Base	length	l_{ba}	20
	width	w_{ba}	80
Center tine	length	l_{ct}	300
	width	w_{ct}	24
Side tine	length	l_{st}	300
	width	w_{st}	12
Distance base to proof mass center	x-direction	x_F	325.45
	z-direction	z_F	161.05
Proof mass	thickness	t_{pm}	320

along the center tine as shown in Fig. 4.23c. The measured profile is plotted in Fig. 4.23d. The device dimensions from Table 4.4 and the resulting proof mass of 2.2695×10^{-7} kg were used to fit Eq. (4.66) to the measured profile. Since the sensor was sitting flat on the tool during the measurement, a z-acceleration a_z of 1 g and no acceleration in x-direction were used. The only fitting parameter is the stress difference $\Delta\sigma$ and the best fit was achieved for a value of 110 MPa. The FEM model was used with the same accelerations and stress difference to verify the accuracy of the theoretical model and to compare nonlinear geometry and linear geometry FEM analyses. The figure shows that there is good agreement and for this portion of the analysis nonlinear effects do not have to be considered[8]. The film stresses for the bottom and top AlN layers were determined after each deposition using a *KLA Tencor FLX-2320* film stress measurement system as described in Section 2.3.3. For the wafer that yielded the accelerometer device under investigation the bottom and top AlN layers had tensile film stresses of 11.8 and 136.2 MPa, respectively, resulting in an expected stress difference $\Delta\sigma$ of 124.4 MPa. The many factors that can cause the deviation between the stress differences determined from the wafer curvature and the beam curvature include measurement uncertainties of the optical measurement methods, uncertainty in the the exact proof mass due to roughening of the backside, slight AlN layer thickness deviations and possible variations of the local film stresses compared to the global measurement. Furthermore, the model assumes that the stresses are uniform throughout each layer. As it was shown in Section 2.4.4, the actual AlN film stress has a complicated gradient in the thickness direction. Considering all of these uncertainties an error of only 14.4 MPa or 11.6 % between the measured stress difference on the wafer and the stress difference used in the equation and FEM analysis to obtain the accurate beam profile is a remarkably good result. For the following investigations, the value of 110 MPa determined from the actual beam profile is used in the FEM analyses as it most closely represents the sensor under investigation. The FEM simulation was performed with a guided proof mass, which results in stress-based sensing, and with free proof mass, which results in bent-beam sensing. Then, the sensor was mounted in the test setup shown in Fig. 4.24a and rotated around the axis perpendicular to the sense axis, such that the direction of the 1 g gravitational force was varied as illustrated in Fig. 4.24b. The tilt angle was increased in steps of 10° for one whole rotation. At each step, the resonance frequencies were determined for the three mode shapes M_1, M_2 and M_3 shown in Fig. 4.18 from the measured impedance spectrum using the method described in Section 4.4.1. Figure 4.25a shows the relative frequency shift of the antisymmetric sense mode compared to the bent-beam sensing FEM simulation results. It can be seen that the results are in very good agreement. The stress-based FEM results are also shown compared to the theoretical frequency shift from the y-component of the gravitational force as calculated from Eq. (4.55). Those results are also in good agreement with each other. By comparing the experimental results to the analytical solution it can be seen that several orders of magnitude of sensitivity improvement can be achieved by the novel approach of bent-beam sensing (note the difference in the left and right y-axes). Since only the y-component component of the gravitational force causes a frequency shift for the stress-based FEM and analytical calculation, the frequency shift is zero when the sensor is horizontal right side up or upside down and goes through extrema when the sensor is either pointing vertically up (90°) or vertically down (-90°). For the experimental results and the bent-beam case the situation is more complex. The zero-crossings and extrema occur at different angles because both

[8]However, usage of nonlinear geometry was found to be critical when the resonance frequencies of the deformed TBTF are to be determined because the results can otherwise be off by an order of magnitude.

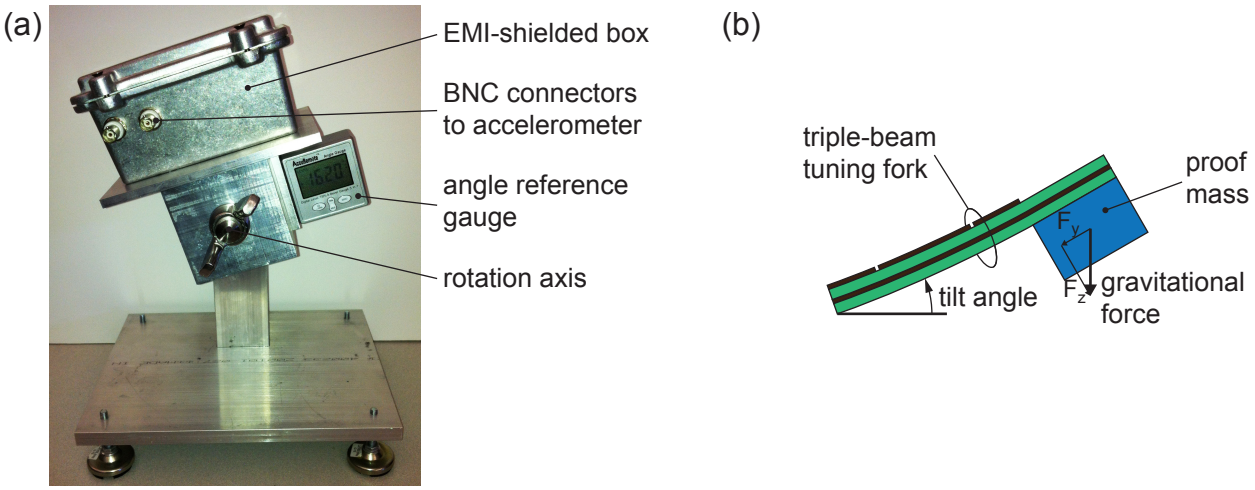

Figure 4.24. Test setup for accelerometer testing. (a): Photograph of tilt setup. (b): Schematic view of the accelometer during tilt testing.

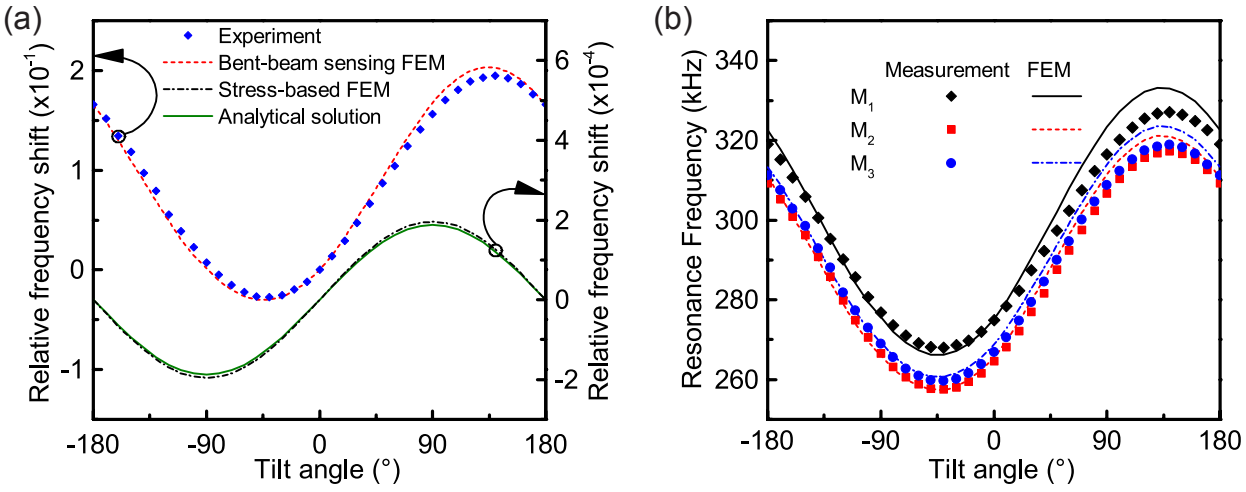

Figure 4.25. Results of accelerometer testing with tilt setup. (a): Comparison of experimental results to stress-based and bent-beam FEM results and analytical solution. (b): Comparison of three different mode shapes to FEM results.

the y- and the z-components of the gravitational force cause bending of the TBTF and because the device is pre-deformed due to the stress difference. In Fig. 4.25b, it can be seen that all three resonance modes under investigation follow the behavior predicted by the FEM analysis.

A more extensive performance evaluation was also done for another sensor. This device was tested for acceleration sensitivity but its other properties, such as initial bending and proof mass thickness, were not measured. However, the results are interesting because this device has two working sensing elements along one sense axis, such that differential signals can be evaluated simultaneously. These test can yield additional performance metrics such as linearity and cross-axis rejection. The device layout is shown in Fig. 4.26a and the two investigated sensing elements are marked as Channel A and Channel B. For these devices, it is expected that the differential

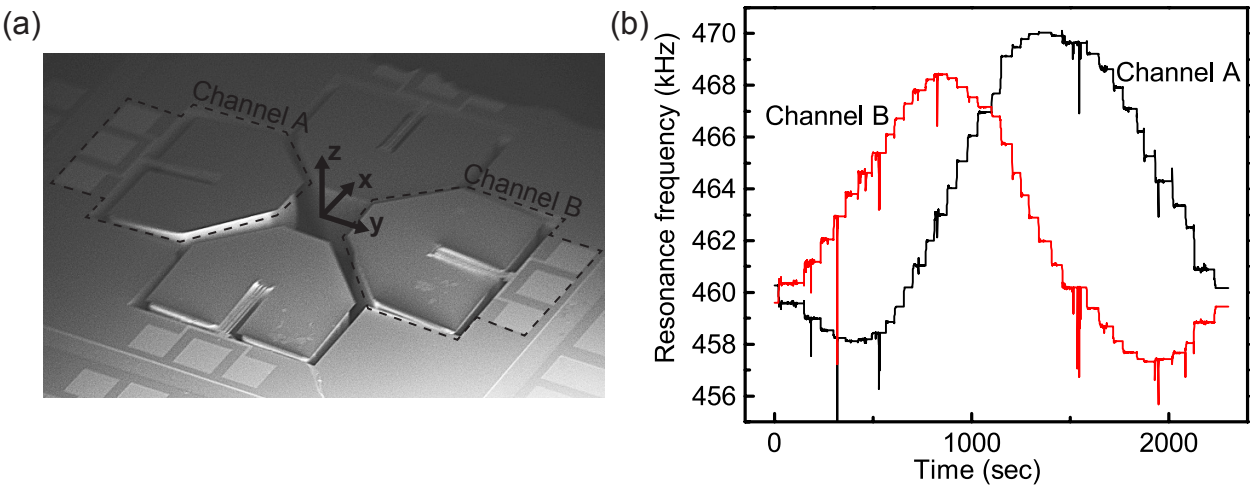

Figure 4.26. (a): SEM image of accelerometer for two-channel measurement with axis definition. (b): Resonance frequency of the accelerometer's two channels over time while the device is rotated about the x-axis in steps of 10°.

signal is sensitive to acceleration in the y-direction and the common mode signal is sensitive to acceleration in the z-direction. The device should not be sensitive to an acceleration in the x-direction. In Fig. 4.26b, the dominant resonance frequency of each channel is shown over time as the device is rotated around the x-axis and held at each 10°-increment for several seconds as described above. In this case, the resonance modes are locked in with a PLL as described in Section 4.4.2. It can be seen that the locking to the two resonance frequencies simultaneously is successful for the whole 360°-rotation of the sensor. The behavior of this device differs from that of the sensor used for Fig. 4.25. The initial resonance frequency of about 460 kHz is significantly higher than the 270 kHz for the previously measured device for the same resonance mode shape as determined from the impedance spectrum. Furthermore, the frequency shift range for the full rotation is only about 11 kHz compared to the previously measured 60 kHz. These findings indicate that the two devices have significant mechanical differences that could not be investigated further because the second device was shipped as a prototype chip to the industrial partner company for this project. The raw data from Fig. 4.26b is shown as resonance frequency over rotation angle around the x-axis in Fig. 4.27a. For the measurement results shown in Fig. 4.27b, the device was mounted perpendicular to its original orientation inside of the text box and thus rotated around the y-axis. In this case, the y-axis component of the gravitational force should be zero at all times

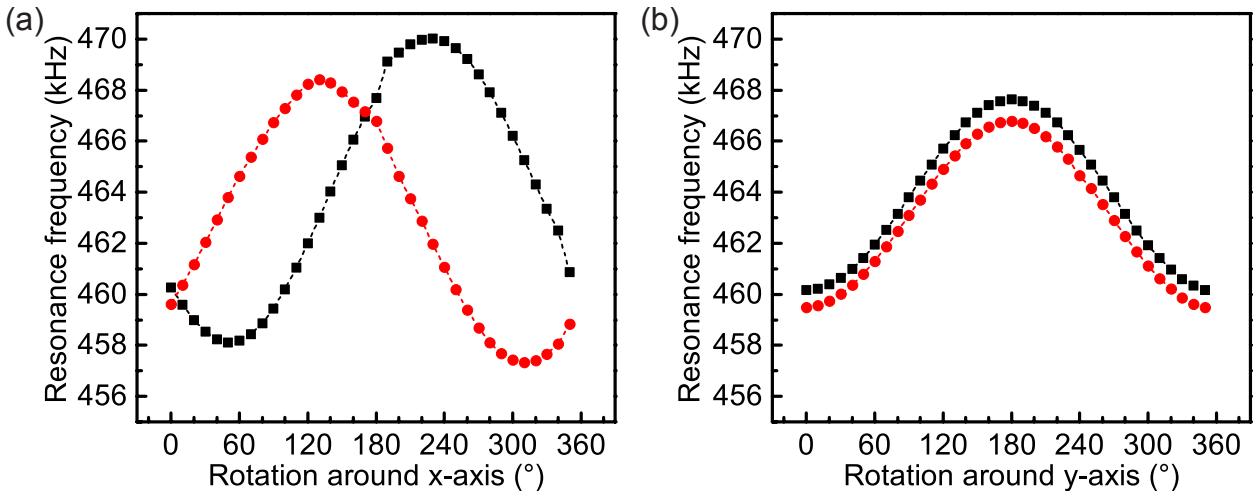

Figure 4.27. Results of tilt measurement with two-channel accelerometer for Channel A (black squares) and Channel B (red circles). (a): Resonance frequency over rotation angle around x-axis. (b): Resonance frequency over rotation angle around y-axis.

and only the z-axis component should vary with the angle. The x-, y- and z-components of the gravitational force acting on the device can be calculated with the following equations based on trigonometric considerations.

$$\begin{aligned} &\text{For rotation around x-axis:} && F_x = 0 \\ &&& F_y = 1g \times \sin(\text{angle}) \\ &&& F_z = 1g \times \cos(\text{angle}) \\ &\text{For rotation around y-axis:} && F_x = -1g \times \sin(\text{angle}) \\ &&& F_y = 0 \\ &&& F_z = 1g \times \cos(\text{angle}) \end{aligned} \tag{4.67}$$

In Fig. 4.28a, the differential signal between Channel A and Channel B is plotted over the calculated y- and x-accelerations from the tilt tests around the x- and y-axes, respectively. It can be seen that the behavior is linear for both cases. The y-axis acceleration sensitivity is -8.76 kHz/g and the parasitic cross-sensitivity for x-axis acceleration is 93.4 Hz/g, which results in a measured cross-axis rejection ratio of 93.8. The true cross-axis rejection might be better than this value because exact alignment of the device with respect to the rotation axes could not be verified. The common mode signal of the two channels, which is expected to be a measure of the z-axis acceleration, is plotted over the calculated z-acceleration for both rotation tests in Fig. 4.28b. It can be seen that the results for both tests are in good agreement with each other. The measured z-axis sensitivities are -7.30 kHz/g and -7.38 kHz/g for the rotation tests around the x-axis and the y-axis, respectively.

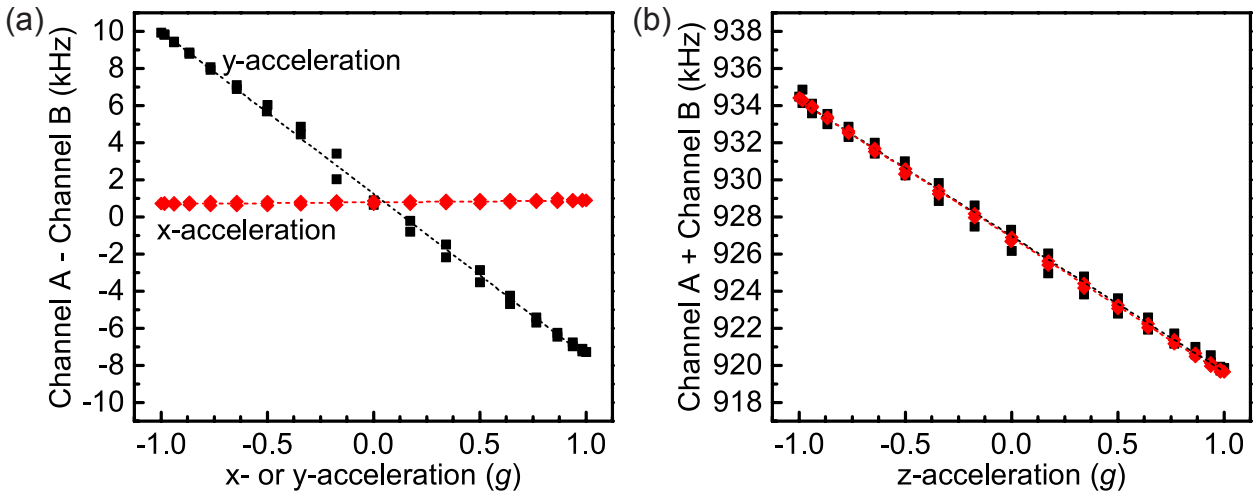

Figure 4.28. Acceleration sensitivity of a differential TBTF accelerometer. (a): Y-axis acceleration sensitivity from tilt test around x-axis (black squares) and x-axis cross-sensitivity from tilt test around y-axis (red diamonds). (b): Z-axis acceleration sensitivity from tilt test around x-axis (black squares) and from tilt test around y-axis (red diamonds).

Chapter 5

Rate Gyroscopes

Rate gyroscopes are amongst the most complicated of all micro-electromechanical system (MEMS) sensors because of their complex dynamic behavior and the necessity for carefully designed control circuits. Due to the limited amount of time and resources available for this doctoral research the aim is not to present a commercially competitive fully functional prototype of an aluminum nitride (AlN) rate gyroscope. Instead, the goal is to show a proof-of-concept demonstration that a rate gyroscope can be fabricated with the presented surface-micromachining fabrication process (Section 3.1) and that AlN can be used as both the structural material and to provide the piezoelectric drive and sense capabilities.[1]

5.1 Design concept

The design of the AlN rate gyroscope consists of a proof mass that is held by four pairs of symmetric suspension beams. Both the proof mass and the beams consist of a single layer of 2 μm thick AlN sandwiched between a continuous bottom electrode and a patterned top electrode. These 100 nm thick platinum electrodes have a negligible effect on the structural properties of the gyroscope and their purpose is to supply an electric field to the drive beams and pick of electric charges from the sense beams. A scanning electron micrograph of the gyroscope is shown in Fig. 5.1 with special emphasis on the patterned top electrodes of the suspension beams. This gyroscope relies fully on the piezoelectric properties of AlN instead of being electrostatically driven and capacitively sensed like most commercial devices. Consequently, there are no comb drives and the in-plane drive and sense motions have to be actuated and sensed in a different way as shown conceptually in Fig. 5.2. The top electrode is patterned in an s-shape on each long leg of

[1]The rate gyroscope was first presented at the Ultrasonics Symposium 2012 in Dresden, Germany [87]. In this chapter, the findings of this conference paper are reproduced in an expanded form to present a more thorough discussion of the results and the future direction of this research.

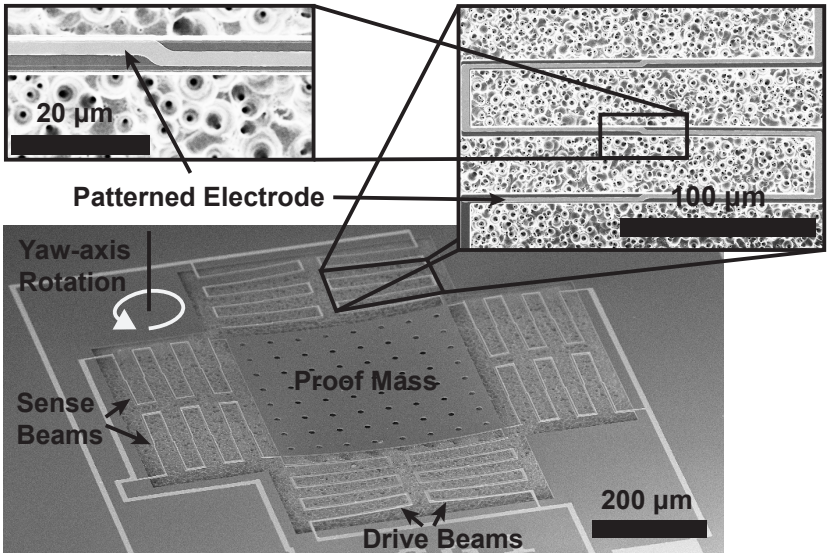

Figure 5.1. SEM image of the aluminum nitride gyroscope. Close-ups of a suspension beam show patterning of top electrode.

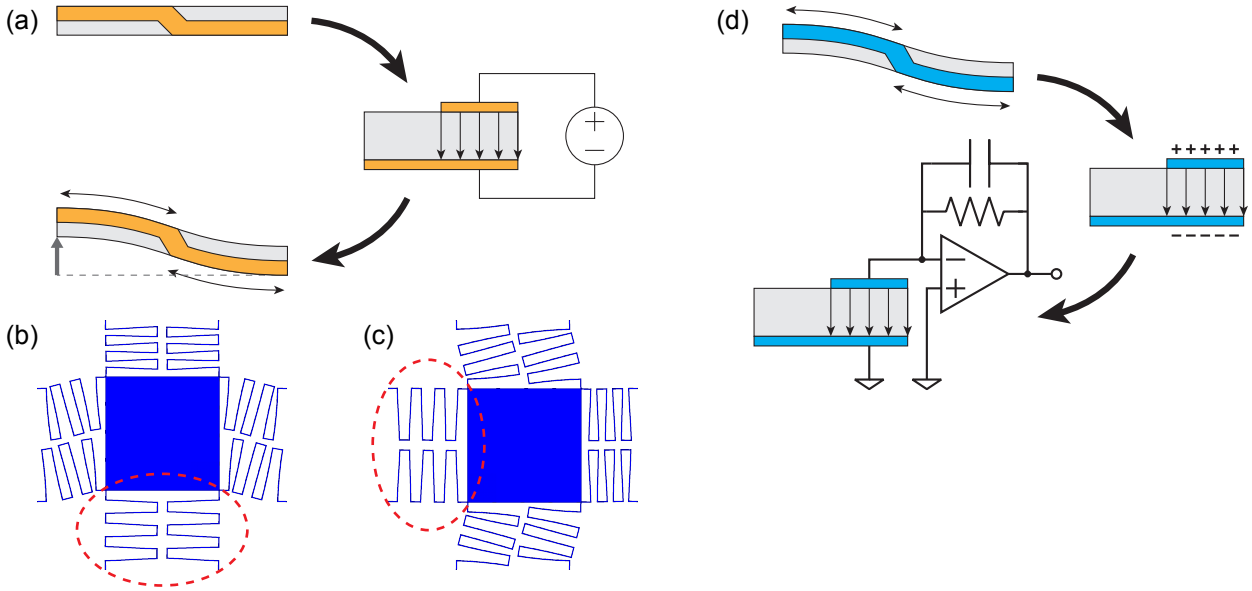

Figure 5.2. (a): Patterning of top electrode (orange) on drive beam enables localized electrical field across beam cross-section resulting in s-shaped beam deflection. (b): Mode shape driven by applying voltage to the drive beam (dashed line) electrodes. (c): Resulting mode shape from yaw-axis rotation, sense beams highlighted by dashed line. (d): Patterning of top electrode (blue) on sense beam results in charge collection upon s-shaped beam deflection that is sensed with transimpedance amplifier circuit.

the suspension beams resulting in local application of the electrical field in those areas and consequently an s-shaped beam deformation (Fig. 5.2a). This actuation method is very similar to the double-ended tuning fork (DETF) operation presented in Chapter 4. In the case of the gyroscope, the resulting overall deformation is shown in Fig. 5.2b and corresponds to the first fundamental in-plane resonance mode shape of the device. When excited at this drive mode, an external yaw axis[2] rotation causes a small component of vibration in the sense mode (Fig. 5.2c), which is theoretically at the same frequency and has the same deformed shape but rotated by 90°. The patterning on the sense beams allows for charges to be collected specifically when exciting the sense mode, which can be converted to a useable voltage signal with a transimpedance amplifier (Fig. 5.2d).

5.2 Electrical characterization

The electrical characterization of the device was performed in a vacuum chamber capable of varying the pressure in a wide range. The drive beams were actuated with a network analyzers output port, while the sense beams were connected to its input port via a transimpedance amplifier to convert the current signal into a voltage signal. Due to very significant quadrature coupling of the drive and sense axes, both resonance peaks can be observed in the resulting impedance plots (Fig. 5.3a). It can be seen that the modes are separated by 43.5 Hz, which is caused by manufacturing tolerances. Significant phase shift, which is required for operation of the gyroscope in any kind of oscillator circuit is only achieved for the lowest of the three measured pressures, i.e. at 900 mTorr. An equivalent circuit model consisting of a series connection of motional resistance, inductance and capacitance in parallel to a feed through capacitance as described for the tuning fork sensors in Section 4.3 was subsequently fitted to one of the peaks of the impedance plot. Figure 5.3b shows that an excellent fit was achieved, which verifies that this lumped parameter model is valid for the device. The extracted parameters are shown in Table 5.1. The motional

Table 5.1. Extracted parameters of rate gyroscope's resonance peak.

Symbol	Parameter	Value (μm)
R_m	motional resistance	495 Ω
L_m	motional inductance	17.5 MH
C_m	motional capacitance	6.67 aF
C_0	feedthrough capacitance	14.8 fF
f_0	resonance frequency	14.738 kHz
Q	mechanical quality factor	3275

resistance R_m is relatively high compared to other AlN resonators, which indicates that special care is required for the design of drive circuits. Due to the large R_m the small feed through capacitance C_0 has a significant effect on the effective impedance. This can be seen in the simulated data of the effective circuit with C_0 removed in Fig. 5.3b. The quality factor is lower than for other MEMS

[2]The yaw axis is defined as the axis normal to the substrate plane similar to the yaw axis of air or ground vehicles, which is defined to be vertical when the vehicle is upright and traveling horizontally.

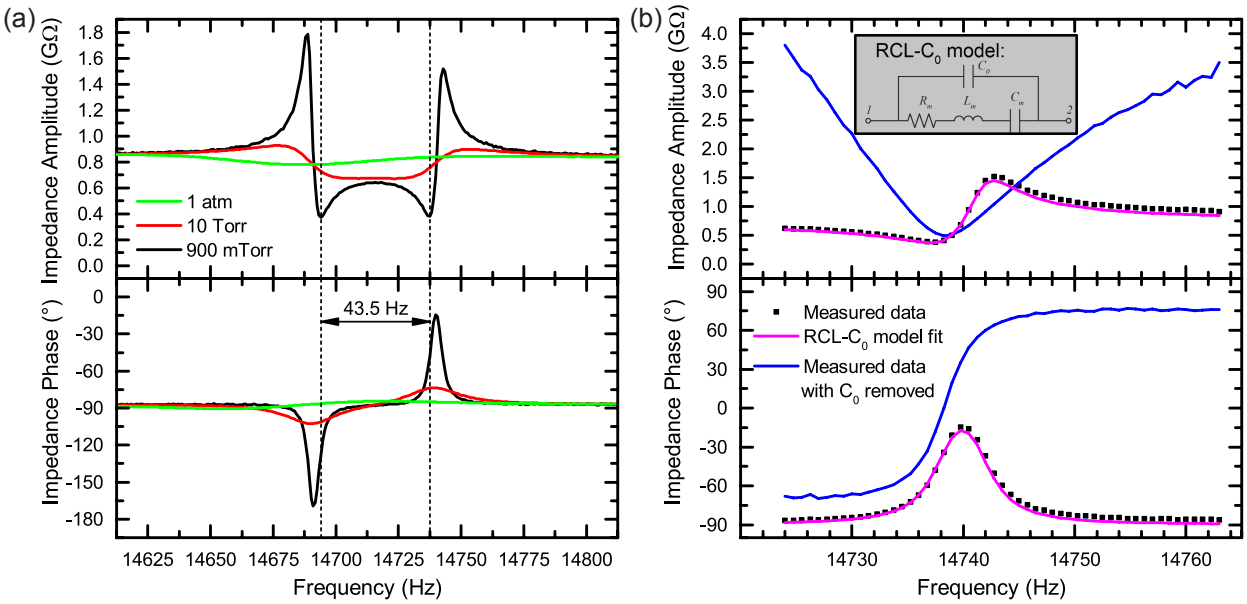

Figure 5.3. (a) Impedance defined as ratio of drive beam voltage and sense beam current vs. frequency at different pressures; drive and sense mode resonance peaks show clear separation and significant phase shift at 900 mTorr; (b) Impedance amplitude and phase of one of the resonance peaks, fitted data from equivalent circuit model and data with feed through capacitance C_0 removed; inset: equivalent circuit model with motional resistance R_m, motional inductance L_m, motional capacitance C_m and feed through capacitance C_0.

gyroscopes, which can be explained by both slide film damping due to the relatively high pressure level and by anchor losses because of the unbalanced, single mass design of the AlN gyroscope.

5.3 Rate sensing characterization

For the initial rate sensing characterization the same electrical setup as for the electrical characterization was used. However, the gyroscope was now mounted inside of a vacuum chamber, which is placed on a rate table as shown Fig. 5.4a. The vacuum chamber can be pumped down and disconnected in order to hold a vacuum during rotation. This approach is more flexible than traditional die level vacuum packaging as many different vacuum levels and devices can be tested with relatively little effort. A disadvantage of this approach is that the achieved pressures are not as low (about 1 Torr) and cannot be kept completely constant due to outgassing of materials and slow leaks in the chamber. For these first tests, the drive beams were operated at a constant root mean square (RMS) voltage at the previously measured resonance frequency, while the signal from the sense axis was measured. The sense signal is mainly comprised of quadrature from the drive axis with a small component caused by the Coriolis force. This small component is plotted as a function of rotation rate in Fig. 5.5. The linearity was found to have an adjusted coefficient of determination of 0.9918. A measure for the noise density was taken by varying the measurement bandwidth of the network analyzer, recording the signal at no applied rotation for an amount of

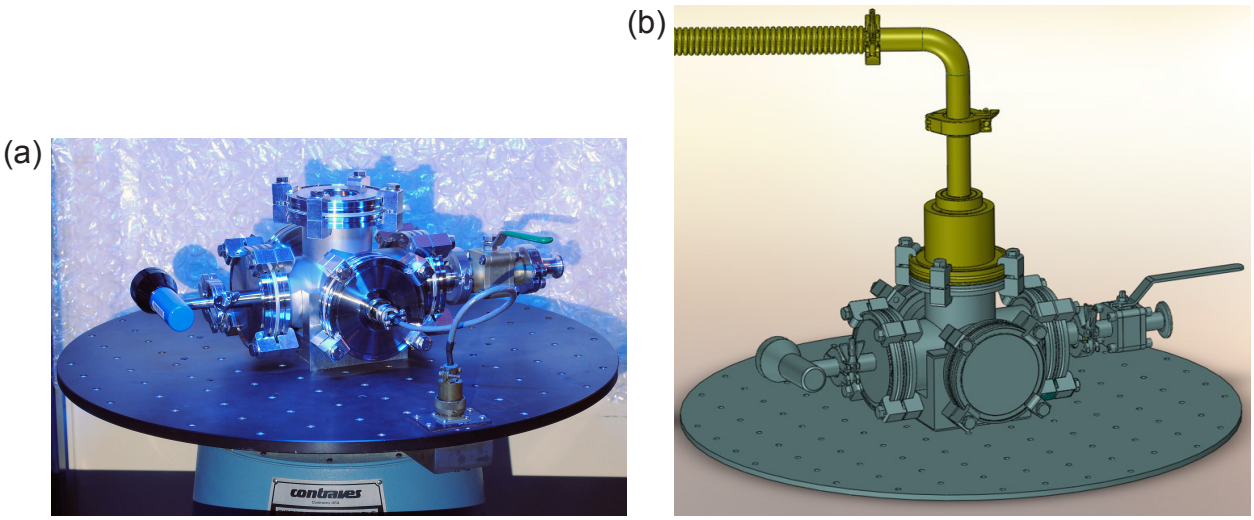

Figure 5.4. Vacuum chamber mounted on rate table shown (a) as a photograph of the existing system and (b) as a drawing of the improved system with rotating vacuum feedthrough for better and more constant vacuum level.

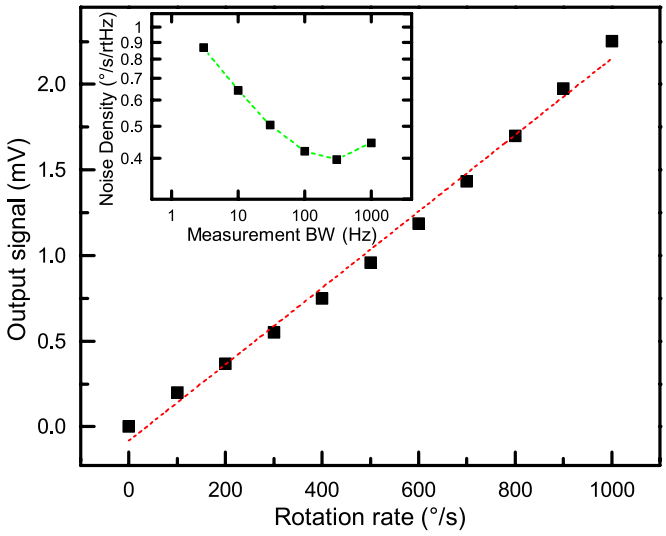

Figure 5.5. Measured output signal vs. rotation rate (black squares) and linear fit (dashed red line).

time and extracting RMS-value of the signal variation. The noise density as shown in the inset in Fig. 5.5 has a minimum of 0.396 °/s/ $\sqrt{\text{Hz}}$ at 300 Hz. It should be noted that these simple measurements of the sensitivity and noise density serve mostly as a proof-of-concept demonstration of the AlN gyroscope. A true characterization of the device's maximally achievable performance can only be obtained with an improved measurement setup as detailed in the following section.

5.4 Improved rate gyroscope testing

Due to the open loop drive axis operation in the first experiments any fluctuations in the device resonance frequencies, e.g., due to temperature or pressure variations, strongly impact the gyroscopes output signal. For a true performance characterization care must be taken to operate the drive axis vibration at constant physical amplitude. The necessary drive circuit includes a feedback loop that takes the signal from the pair of beams opposing the drive beams to adjust the drive voltage in order to keep the amplitude constant. A block diagram of the circuit is shown in Fig. 5.6. The oscillator loop of the circuit starts at the feedback branch from the drive axis (A) and the output alternating current (AC) signal is converted to an AC voltage. Then, two amplifier stages apply both a constant and a variable gain to the signal before a high-pass filter removes any unwanted direct current (DC) offset and the signal is fed back into the actuation branch of the drive axis (C). The variable gain is controlled by a proportional-integral (PI)-controller, such that the physical oscillation amplitude of the drive axis stays constant. For this purpose, the signal from the feedback branch is branched off after the initial gain stage and any DC offset is removed with a high-pass filter. Then, by combining a rectifier and a low-pass filter, the amplitude of the AC voltage is converted to a DC signal. The signal is compared to a set reference voltage and a PI-controller tries to minimize any deviation by modifying the variable gain of the drive signal.

In the initial testing only the total output signal including both quadrature and a component from the rotation was observed. A much better signal-to-noise ratio can be achieved by isolating the rate signal, which has a 90° phase shift to the drive oscillation. For this purpose, the differential signal of the output axis' two ports (B and D) is converted to a single-ended signal and fed into a lock-in amplifier. The feedback signal from the drive axis is used as a reference and the lock-in amplifier is configured to measure the RMS voltage of the sense axis signal 90° shifted from the reference signal with high rejection of the quadrature signal. The complete circuit has been developed and fabricated. The circuit diagram is shown in Appendix F. Any future work on this project should start with the fine-tuning of this circuit and full characterization of the existing rate gyroscope before any improvements to the system are attempted.

A way to achieve a lower pressure and keep it constant for a longer period of time has been developed and should also be included in any future work. A rotary feedthrough on the rotating vacuum chamber has been designed and built with the goal of keeping the chamber permanently connected to the vacuum pump. A computer-aided design (CAD) drawing of the setup is shown in Fig. 5.4b. Using this improved vacuum chamber setup in combination with the developed drive circuit should significantly improve the system and will allow the characterization of the rate gyroscope's true performance limits. If the performance specifications prove to be adequate there is

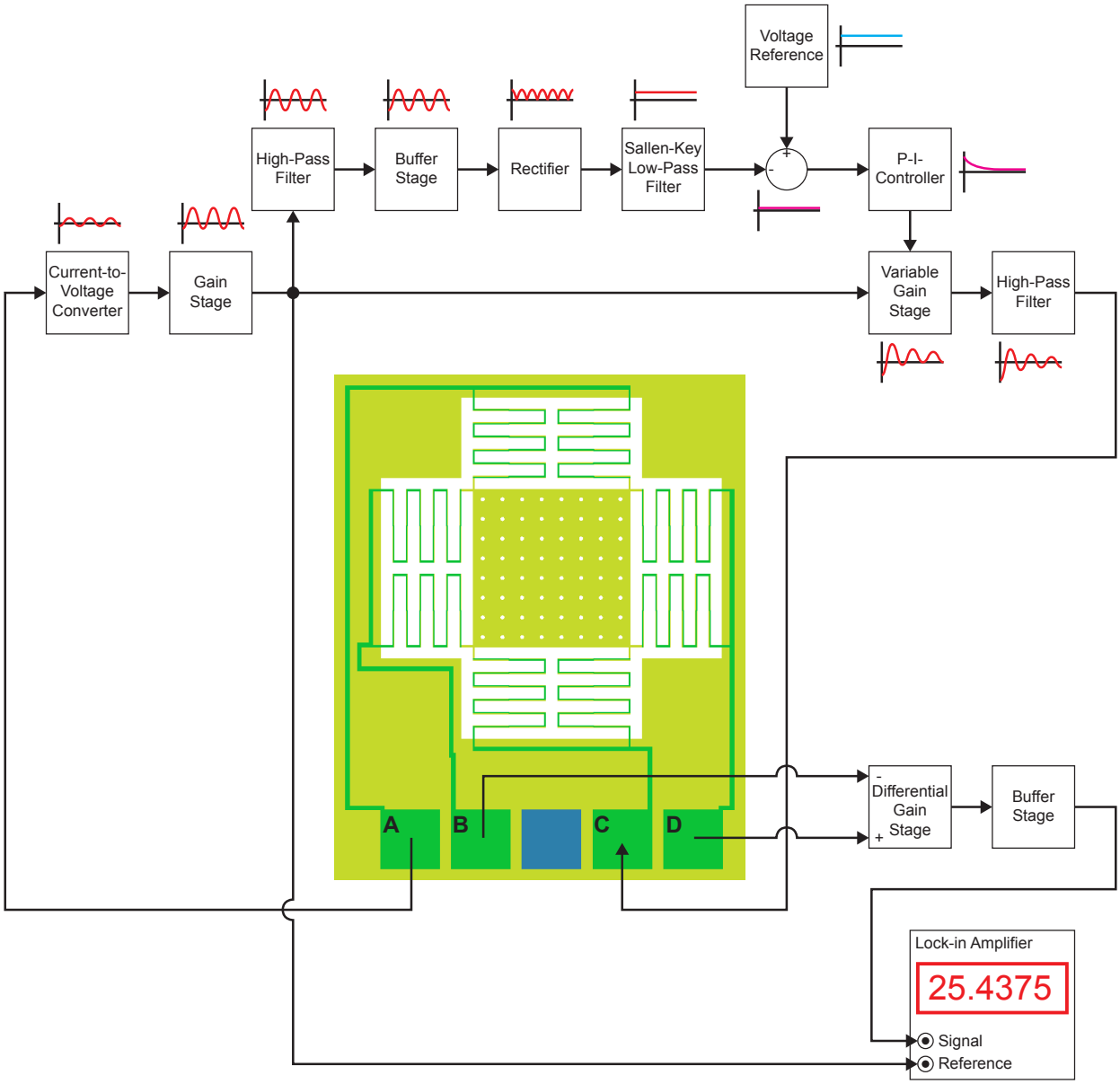

Figure 5.6. Block diagram of the developed gyroscope drive circuit.

a vast array of potential applications. The high temperature stability of AlN allows inertial sensors made in this process to penetrate new markets that are in need of inertial navigation at high temperatures such as deep oil well drilling, geothermal energy generation or space exploration.

Chapter 6

High Temperature Testing

One of the main reasons to explore the capability of thin-film aluminum nitride (AlN) as sensor material in this doctoral research is the potential application in high temperature environments. As mentioned in the beginning of Chapter 2, below 1000 °C, no significant oxidation or reduction occurs in air and vacuum environments, respectively. There is also published data that suggests that thin-film AlN retains its piezoelectric properties up to at least 1150 °C [88]. In this chapter, the choice of AlN as high temperature sensor material is explained by comparing its properties to silicon, the conventional micro-electromechanical system (MEMS) sensor material. Additionally, high temperature testing of tuning fork sensor elements by heating with infrared (IR) light is described. Finally, a setup capable of performing simultaneous high temperature and acceleration testing is introduced.

6.1 Mechanical properties of AlN at high temperature

The prevailing material for MEMS sensors today is silicon, which is used by virtually all commercial manufacturers as the structural layer of sensing elements. It is also the most common material for the actuation (electrostatic) and detection (capacitive) in MEMS sensors. Any attempt to introduce a novel material as both structural and active layer for MEMS sensors must therefore demonstrate a clear advantage in at least one area for the chosen application. In this case, the high temperature capability of thin-film AlN represents this advantage. In Fig. 6.1, an attempt is made at quantifying the benefit of AlN compared to silicon at high temperatures. Mechanical properties at high temperature for these materials have not been characterized extensively, so a direct comparison of thin-film silicon to thin-film AlN is difficult. In Fig. 6.1a, the yield strength of a bulk sample of single crystalline silicon [89] is compared to the 3-point bending strength of a bulk sample of hot-pressed polycrystalline AlN [90]. This data does not exist for thin-film AlN, but it is likely that the polycrystalline AlN films show a similar or better behavior than the hot-pressed

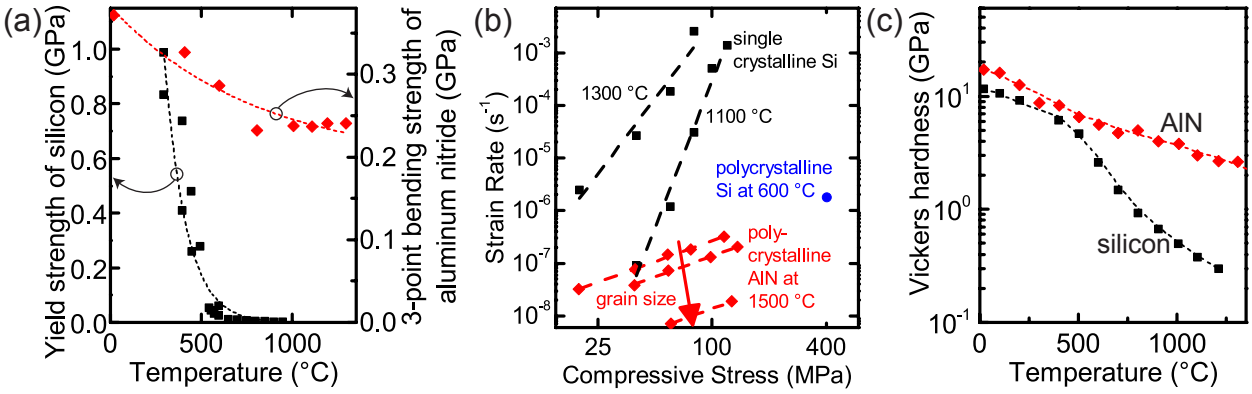

Figure 6.1. Comparison of high temperature properties of silicon and AlN. (a): Yield strength of silicon compared to 3-point bending strength of AlN over temperature. (b): Strain rate of single crystalline silicon, polycrystalline silicon and AlN at different temperatures over compressive stress. (c): Vickers indentation hardness of silicon and AlN over temperature.

bulk samples. Due to the non-homogeneous nature of the hot-pressed material, a 3-point bending test will naturally result in a lower strength value than a tensile test would. Nevertheless, it can be seen that the strength of the silicon sample diminishes rapidly above 500 °C, whereas the strength of AlN decreases only gradually with temperature. Figure 6.1b compares the creep rates of AlN to silicon at elevated temperatures. The bulk samples of AlN used in this study [91] were also hot-pressed polycrystalline material. The data for silicon was taken from two different creep studies. The data for single crystalline silicon was measured on an undoped <111>-wafer [92] and the polycrystalline datapoint was measured on a thin-film sample [93]. In Fig. 6.1c, the Vickers indentation hardness over temperature of bulk samples of single crystal silicon and AlN are compared [94, 95]. The dramatic drop that was observed for the yield strength of silicon around 500 °C can also be seen in the hardness measurement. Similar to its strength value, the hardness of AlN only decreases at a moderate rate with increasing temperature. These three pieces of material data clearly show that, unlike silicon, AlN has the potential of being a structurally usable material at temperatures above 600 °C, which is the target temperature for the sensors presented in this doctoral research.

6.2 High temperature testing of tuning forks

6.2.1 DETF high temperature testing

One aspect of this work is the demonstration of operating the AlN double-ended tuning fork (DETF) sensor at high temperature to prove usability for harsh environment sensing applications. For this purpose, a MEMS die is mounted in a ceramic package. The chip is temporarily held in place by carbon paste to connect the wire-bonds. During the high temperature experiment this

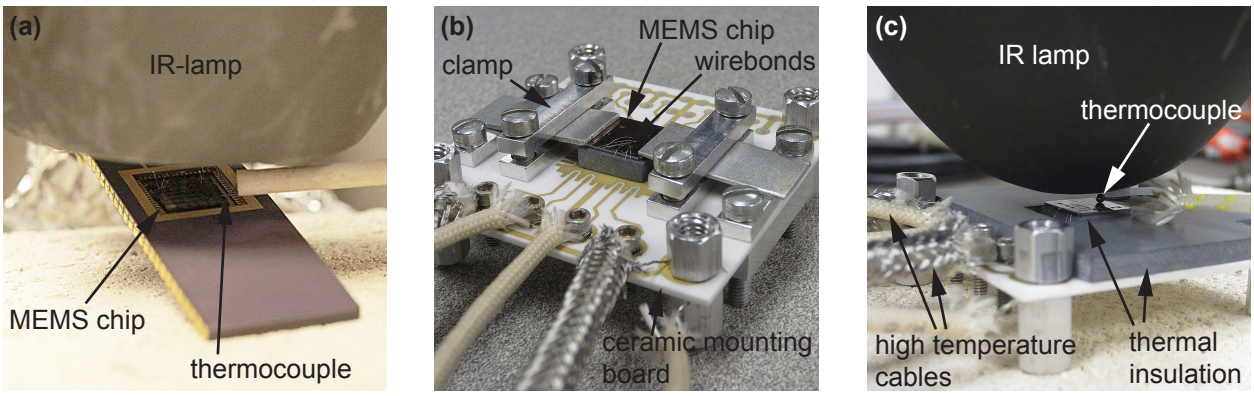

Figure 6.2. Setups for high temperature measurements of AlN MEMS devices. (a): MEMS chip on conventional ceramic package with IR lamp. (b): Mounting of MEMS chip on custom ceramic board with aluminum holders in place to keep the chip in place during wirebonding. (c): Custom ceramic board with MEMS chip in place, holders removed and additional thermal insulation added under IR lamp.

bond detaches and the die is held in place only by the bond wires. In this way, no thermal stresses from the ceramic package can be coupled into the DETF and the unaltered behavior of the MEMS die itself is tested. Prior to the experiment, the resistance of an on-chip platinum temperature sensor is calibrated in a temperature chamber. The signal from the platinum sensor is used to monitor the actual temperature on the MEMS die during the experiment. The temperature is increased by focusing a high power IR lamp on the surface of the MEMS die. Figure 6.2a shows the setup used for this testing and a more advanced setup is shown in Fig. 6.2b and c. The power is slowly increased until the on-chip temperature reaches 600 °C and then decreased back to near room temperature. The total time for each cycle is about 20 minutes and the experiment is repeated for a total of three cycles. The resonance frequency of the AlN DETF and the temperature measured by the on-chip sensor are shown in Fig. 6.3a. It can be seen that the AlN DETF is operational up to a temperature of 570 °C. For higher temperatures, the linear oscillator circuit was not able to lock to the DETFs resonance frequency. These areas are shown with dotted lines in the figure. This behavior is assumed to be caused by the increase in noise level at high temperatures in combination with the long cable connections required for the high temperature setup. An improved setup in which the circuit can be placed close to the device without getting damaged by the high temperature can be used to detect the true temperature limit of the DETF sensor in the future. The DETF's resonance frequency as a function of temperature during the cooling phases of all three cycles is shown in Fig. 6.3b. It can be seen that the temperature-dependent behavior of the resonance frequency is highly repeatable. With increasing temperature the resonance frequency initially decreases because of the compressive stress coupled into the DETF from the silicon substrate which has a lower coefficient of thermal expansion (CTE) than AlN. At a temperature of 315 °C, however, a minimum in the resonance frequency is observed. The reason for the turnover point in the frequency is still under investigation. Reported data for AlN [25] and silicon [96] indicate that the CTE of AlN perpendicular to the c-axis direction is always larger than the CTE of silicon in [110]-direction for the temperature range of this experiment. Since there is no crossover in CTEs a steadily increasing compressive stress in the DETF is expected with increasing temperature and thus the frequency should decrease steadily. The possibility of a change in resonance mode at the turnover point could

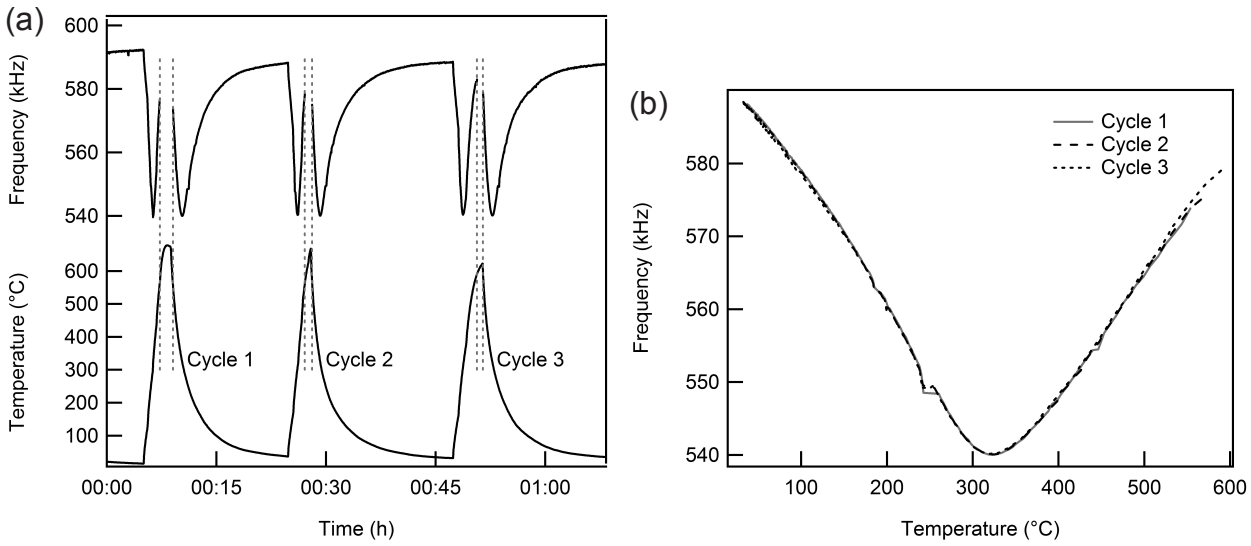

Figure 6.3. Results of DETF high temperature testing. (a): Resonance frequency of DETF and temperature measurement of on-chip temperature sensor over time. Dotted lines indicate limits of temperature range in which oscillating circuit was locked to resonance frequency. (b): Resonance frequency plotted over temperature for three cycles.

also be ruled out from FEM analysis. Finally, all relevant materials have negative thermal coefficients of elastic modulus, which should also result in a steady decrease in resonance frequency with increasing temperature. Further testing needs to be performed to investigate this unexpected behavior.

6.2.2 Strain sensor high temperature testing

In this section, two different types of AlN strain sensors are evaluated, DETFs, Fig. 6.4a and d, and triple-beam tuning forks (TBTFs), Fig. 6.4b and e. The DETFs have been published as strain sensors that can be operated at high temperature [70]. However, no characterization of the high-temperature strain sensitivity was performed as it was not clear whether the change in output signal was caused by change in material properties or change in the amount of applied strain from the mismatch of CTEs. Below, TBTFs are used as transduction elements. A clamped-clamped TBTF exposed to the strain caused by CTE mismatch of the AlN to the silicon substrate (Fig. 6.4b) is compared to an identical device, which is linked to the substrate by an AlN frame (Fig. 6.4c). The frame, which is only connected to the substrate at two center locations, is used to decouple the CTE mismatch strain of AlN and silicon from the TBTF. Consequently, changes in the frequency signal from this device upon heating are only caused by changes in the material properties and the CTE mismatch strain of AlN and electrode metal. Comparing the behavior of the two devices enables the prediction of pure strain sensitivity of the TBTF at elevated temperature. As shown in Section 4.5.1, the relative, stress-induced shift in the fundamental frequency $\Delta f_1/f_1$ of DETFs and

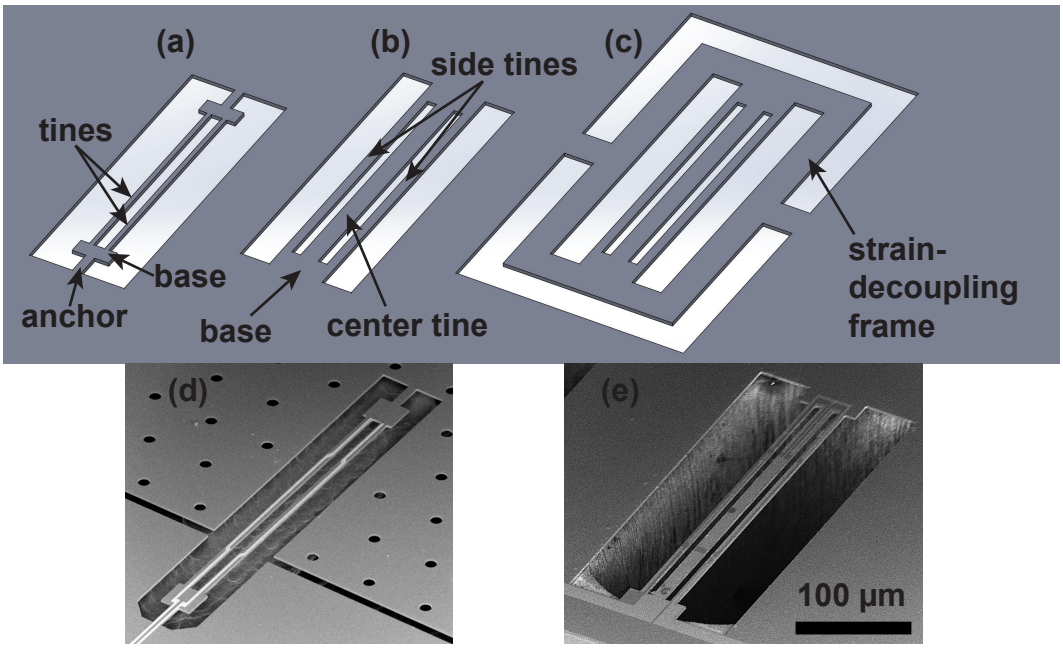

Figure 6.4. Schematic drawings of (a) double-ended tuning fork, (b) TBTF, (c) TBTF in strain-decoupling frame and SEM images of (d) DETF and (e) TBTF.

TBTFs is generally described by the relationship:

$$\frac{\Delta f_1}{f_1} = 0.07374 \frac{L^2}{Etw^3} F \tag{6.1}$$

Where L is the length of the DETF tines, E is the Young's modulus of the material and F is the applied axial force. The dimensions t and w are the widths perpendicular to the deformation and in the direction of the deformation, respectively. For the DETFs shown in Fig. 6.4a, t is the film thickness of the material and w is the width of each tine as viewed normal to the substrate. For the TBTFs shown in Fig. 6.4b and c, t is half the width of the center tine plus the width of one side tine and w is the total thickness of all films. From this equation it is expected that a purely stress-induced frequency shift will linearly correlate with the axial stress or strain, i.e. tensile straining of the device will cause the frequency to increase and compressive straining will cause the frequency to decrease. It will be shown that this relationship does not hold for the TBTF investigated in this work due to reasons that will be explained later. Equation 6.1 is valid for all fundamental modes of the tuning forks, i.e. modes in which all tines have a single inflection point. For this work, the strain generated by the CTE mismatch between AlN and silicon will be used to determine the high temperature strain sensing ability of the TBTF. The AlN is polycrystalline with c-axis orientation normal to the substrate plane and both the mechanical properties and CTE are anisotropic, i.e. they have different values in the direction out of the substrate plane compared to within that plane. Due to the design of the device, the properties within the substrate plane are used for this work. The equivalent Young's modulus and Poisson's ratio were determined numerically from the elastic constants published in literature [97] and their values are 346.1 GPa and 0.3193, respectively. The linear expansion coefficient for AlN perpendicular to the c-axis of AlN is calculated as the derivative of the lattice parameter in that direction with respect to temperature. The values for the

lattice parameter are taken from the literature [98] and the result is plotted over temperature in Fig. 6.5a. The linear expansion coefficient for single crystalline silicon α_{Si} is directly taken from

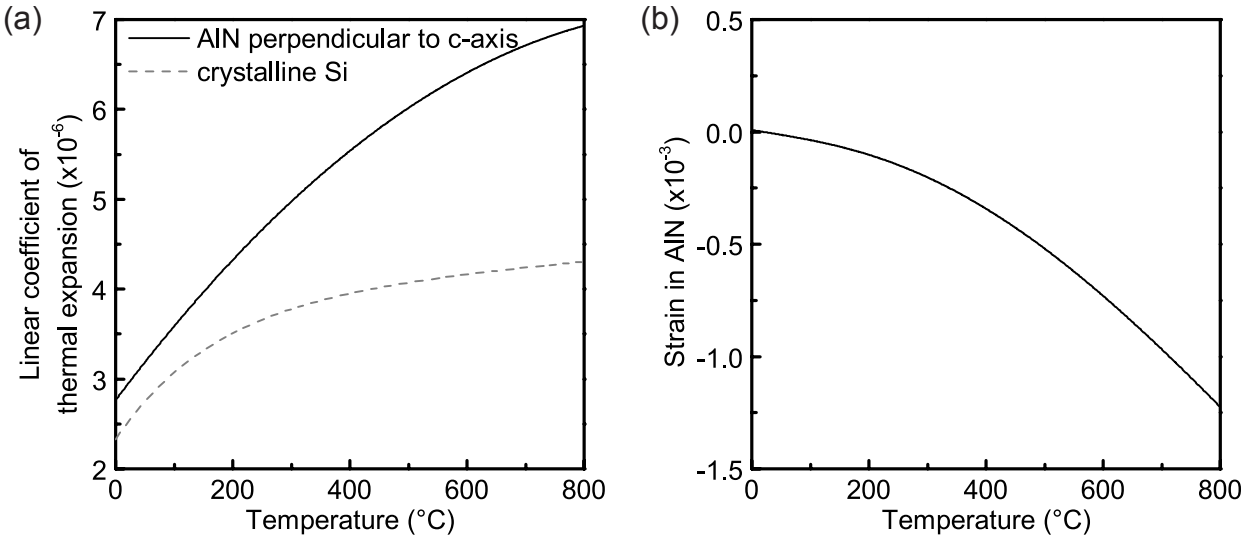

Figure 6.5. (a): Linear coefficients of thermal expansion for AlN perpendicular to c-axis and for single crystalline silicon. (b): Engineering strain in AlN layer calculated from Eq. (6.5).

literature and plotted in the same figure [92]. The following equations approximate the empirically determined coefficients:

$$\alpha_{AlN,a} = 7.658 \times 10^{-8} + 1.102 \times 10^{-8} T - 4.317 \times 10^{-12} T^2 \tag{6.2}$$

$$\alpha_{Si} = 3.725 \times 10^{-6} \left(1 - \exp\left(-5.88 \times 10^{-3} \times (T - 124)\right)\right) + 5.548 \times 10^{-10} T \tag{6.3}$$

The definition of the linear expansion coefficient is:

$$\alpha_L = \frac{1}{L}\frac{\mathrm{d}L}{\mathrm{d}T} \Leftrightarrow \int_{T_0}^{T_1} \alpha_L \mathrm{d}T = \ln\left(\frac{L_1}{L_0}\right) \tag{6.4}$$

Assuming the deformation is dominated by the very thick silicon the engineering strain in the AlN layer e_{AlN} can be expressed as the difference in theoretical deformed lengths of silicon and AlN due to the temperature change divided by the initial length:

$$e_{AlN} = \frac{L_{1,Si} - L_{1,AlN}}{L_0} = \exp\left(\int_{T_0}^{T_1} \alpha_{Si} \mathrm{d}T\right) - \exp\left(\int_{T_0}^{T_1} \alpha_{AlN} \mathrm{d}T\right) \tag{6.5}$$

Figure 6.5b shows the resulting engineering strain over temperature as calculated from Eq. (6.5) using Eq. (6.2) and Eq. (6.3) with T_0=293 K. The devices are tested at elevated temperature by exposing them to high intensity IR light. The testing procedure and detailed results for the DETFs have been reported previously [70]. It was shown that the DETFs can be operated at 570 °C, but the strain sensitivity at elevated temperature could not be tested. Here, the strain sensitivity can be decoupled from other high temperature effects by comparing the TBTF device without frame to

the device with frame. In contrast to the testing of the DETF, no oscillator circuit is used to lock to the devices' resonance frequencies while ramping the temperature. Instead, the temperature is held constant at several different values, while an impedance plot is taken. A *MATLAB* script is then used to extract the resonance frequency peaks as described in Section 4.4.1. This method allows to test for the temperature-dependent behavior of multiple mode shapes frequencies. The measured resonance frequencies over temperature are shown in Fig. 6.6 for all three devices. It can

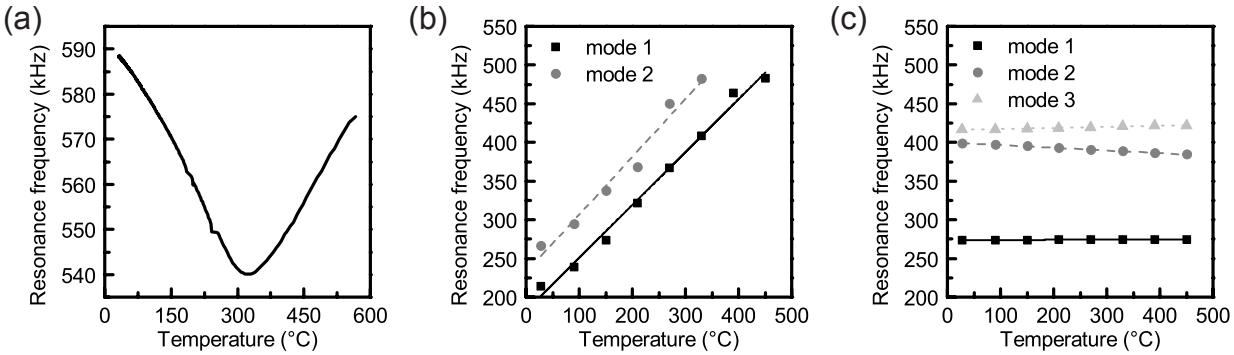

Figure 6.6. Measured resonance frequency over temperature for (a): DETF, (b): TBTF without frame and (c) TBTF with frame. For TBTFs, several resonance peaks are evaluated.

be seen that the TBTF with external frame shows several orders of magnitude smaller frequency shifts than the TBTF without frame. Since the devices are otherwise identical, this finding verifies that the frequency shift in the TBTF is dominated by the CTE mismatch strain between the silicon substrate and the AlN device. Therefore, it is possible to use the conversion from Fig. 6.5b to determine the strain sensitivity of the TBTF devices within the measured range of 28 to 450 °C. An interesting finding is the fact that the resonance frequencies of the TBTF increase as the strain becomes more compressive. This is contrary to the prediction from Eq. 6.1 and the generally expected behavior. It was speculated that an initial out-of-plane buckling of the beams, e.g., caused by residual pieces of substrate silicon, or silicon dioxide (SiO_2) or caused by intrinsic film stress in the AlN or molybdenum layers, could change the behavior of the TBTF upon application of compressive strain. Therefore, finite element method (FEM) modeling was performed in which both a small buckling force and a compressive strain were applied to the TBTF in a non-linear static analysis. The deformed shape of the device was used for a subsequent modal analysis to determine the resonance frequencies for each applied strain. The results of this analysis are shown in Fig. 6.7a. Buckling forces F_B of 85.5 and 171 μN were applied causing an initial maximum displacement of the center tine without applied strain of 0.97 and 1.58 μm, respectively. It can be seen that the experimentally observed behavior of the TBTF can indeed be explained by initial beam buckling. In Fig. 6.7b, the strain sensitivity estimated from the experimental data as the ratio of frequency change to strain change at each temperature step.

It was shown that TBTFs can be used as strain sensing elements at elevated temperatures. Furthermore, a decoupling frame can be employed to create devices that are not sensitive to strain and can thus be used as reference sensors. The sensitivity of the device is around 600 Hz/μstrain, which is about an order of magnitude higher than silicon carbide harsh environment strain sensors that were previously reported [64]. The reduction of strain sensitivity at higher temperature is

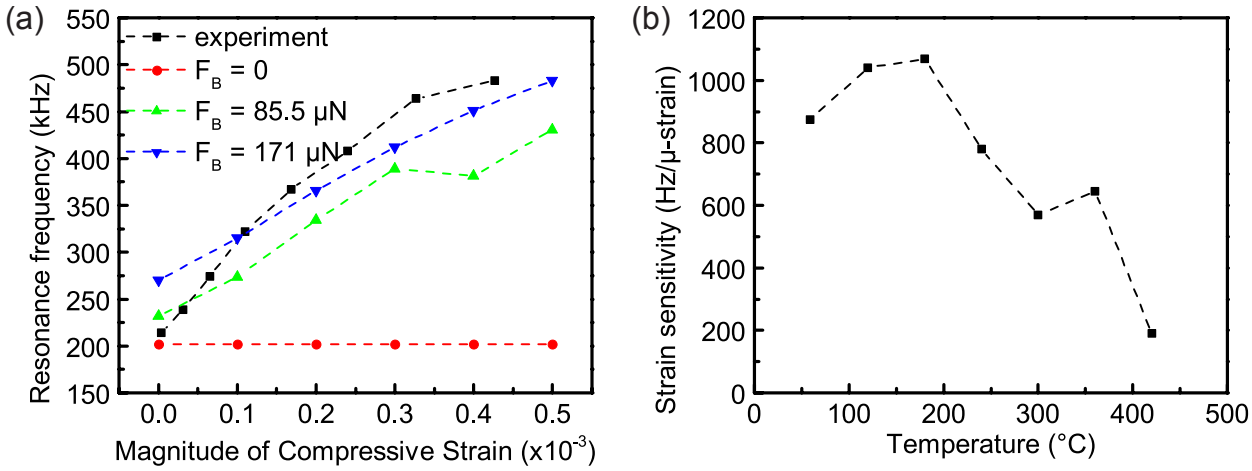

Figure 6.7. (a): Resonance frequency over applied strain as predicted by FEM modeling with different amounts of initial buckling force and as measured for the TBTF. (b): Experimentally determined strain sensitivity over temperature.

presumably caused by the non-linear behavior of the TBTF due to the extreme change in resonance frequency, which more than doubles over the tested range. Better linearity and thus more constant strain sensitivity in a larger temperature range could be achieved by geometric optimization of the tuning fork, e.g., by making the device thicker and wider and thus reducing the overall frequency change. This sensor could find applications in the field of structural health monitoring in industrial applications that require elevated temperature environments or in buildings during emergencies, e.g., for the monitoring of critical structural elements during fires.

6.3 High temperature testing of accelerometers

The next logical step towards the goal of harsh environment inertial sensors is the testing of functioning devices at high temperature. Since the accelerometer technology is at a more mature level than the rate gyroscope technology a test stand for the evaluation of accelerometers was built. For this purpose, the box connecting to the tilt angle setup described in Section 4.5.3 and shown in Fig. 4.24a was modified. The modified box is shown in Fig. 6.8. A strip heater, whose temperature can be controlled with temperature control module, was installed inside the box. The thermocouple for the controller's temperature feedback is clamped directly to the strip heater. Thermocouples are also installed on the MEMS chip's surface, on the ceramic mounting board, on the strip heater, on top of the lid and in the back of the box to monitor the temperatures in different locations during accelerometer testing. Figure 6.9 shows the temperature at some of the thermocouple locations (see numbering in Fig. 6.8) when the heater is set to the maximum output power. The temperatures on the MEMS chip and on the ceramic board next to the chip are almost identical. Therefore, the thermocouple does not have to be placed on the actual device under test (DUT), which reduces the risk of damaging it during the test. The temperature at the edge of the heater appears to be lower than in the center, but it is possible that the clip holding Thermocouple 4 in place was

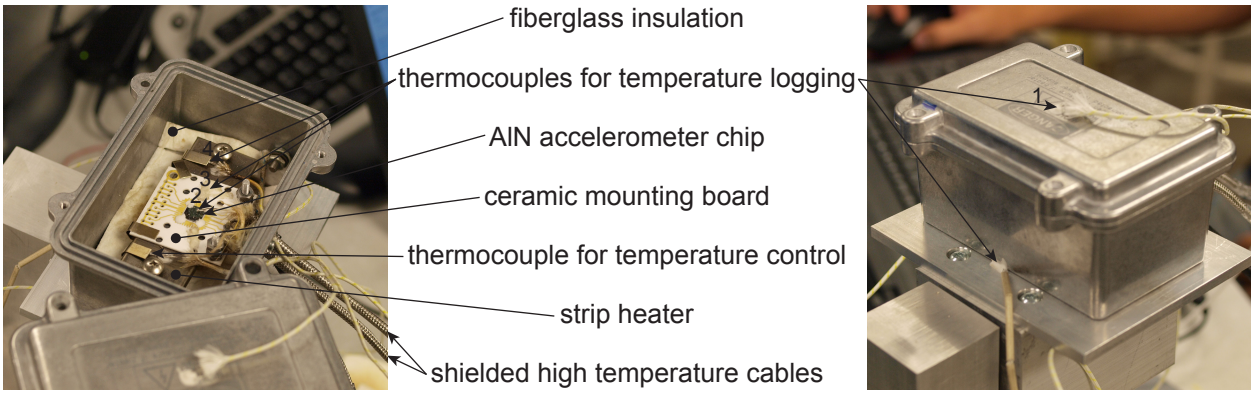

Figure 6.8. Photograph of setup to test accelerometer chips with simultaneous tilt and temperature control. Top view (left) and back view (right).

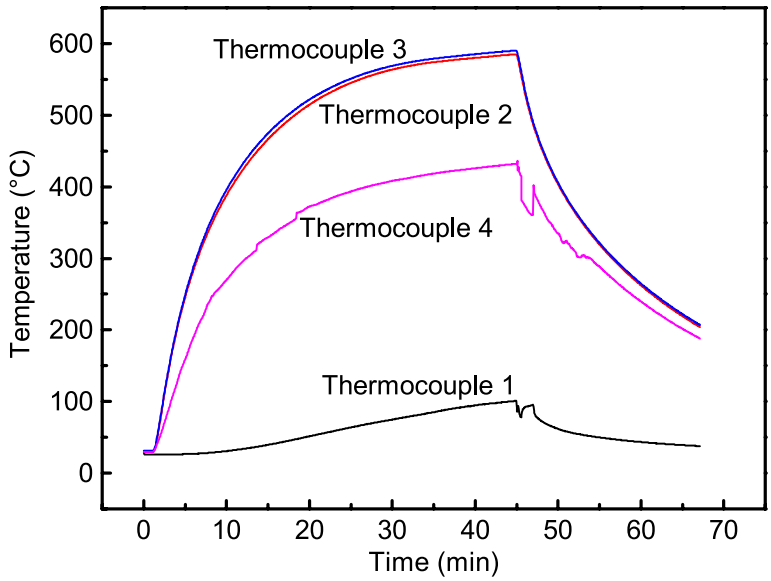

Figure 6.9. Temperature of different thermocouples (see numbering in Fig. 6.8) over time with heater output set to maximum power.

loosened during the experiment and the loss of contact resulted in an erroneous low reading. Most importantly, it can be seen that the MEMS chip can be heated to a temperature of 600 °C, which is the target temperature for testing of the AlN sensors. At this point the temperature of the lid only reaches 100 °C making it save to use with some precautions. More insulation material inside the box can be used to reduce the ramp-up time of 45 minutes and to achieve higher sensor and lower outside temperatures.

Chapter 7

Conclusions and Future Work

7.1 Conclusions

The purpose of this doctoral research was to lay the foundation for advancements in harsh environment sensing technology using aluminum nitride (AlN) as the base material. Several new discoveries were made and several new sensor concepts were developed, fabricated and tested. In the following paragraphs, the most important achievements are summarized. In Chapter 2, the effect of sputtering parameters on the AlN crystal quality, thickness non-uniformity and residual stress were investigated. Furthermore, three new methods to characterize the stress gradient in the thickness direction of thin AlN films were introduced and evaluated. Two different fabrication processes for AlN sensor chips were discussed in Chapter 3. The second process uses both surface- and bulk-micromachining as well as a bilayer of AlN. This innovative process can be used to fabricate both accelerometers with very large silicon proof masses and membrane devices such as pressure sensors on the same chip. It also allows the use of piezoelectric out-of-plane actuation, which enables the usage of triple-beam tuning forks (TBTFs). The advantages of TBTF sensing elements compared to double-ended tuning forks (DETFs) are discussed in Chapter 4 with an in-depth theoretical derivation of the electromechanical behaviors of both devices. In the same chapter, the concept of bent-beam sensing, which uses geometric deformation of the sensing element rather than axial stresses, is introduced. It is experimentally and numerically shown that this new approach results in several orders of magnitude improvement in the accuracy of piezoelectric AlN accelerometers compared to previous technology. Chapter 5 presents a functioning prototype for a novel type of rate gyroscope in which AlN is exclusively used as the structural material as well as for actuation and sensing. In Chapter 6, the capability of AlN as a sensor material for high temperature strain sensors is demonstrated. Operation of a DETF up to 570 °C is demonstrated. By comparing the behavior of a TBTF with a strain-decoupling frame to a regular device strain sensing at high temperature is verified. It is also numerically and experimentally shown that an initial buckling force in the beams affects the sensing behavior and improves the strain sensitivity. A

setup for applying tilt to an accelerometer chip while keeping it heated to a temperature of 600 °C was presented.

7.2 Future Work

AlN sensor research at the Berkeley Micromechanical Analysis and Design Laboratory (BMAD) was started with Gabriele Vigevani's doctoral work [74] and continued with this dissertation. Although significant progress has been made there are many interesting directions in which the research can be taken. The AlN deposition process needs to be optimized, especially in respect to the film stress gradient in the thickness direction of thin AlN films. Better control of this parameter would be beneficial for better and more predictable performance of accelerometers that utilize deformation-based sensing and of devices that require extreme planarity to avoid out-of-plane motions. Better fabrication yield for the deformation-based accelerometers needs to be achieved by optimizing both the surface- and bulk-micromachining fabrication process and the device layout. Optimized design of the devices is also necessary to improve the performance of the accelerometers, especially in respect to shock resilience and cross-axis rejection. The proposed improvements for the AlN rate gyroscope project have been discussed in detail in Chapter 5. The main task is the testing and optimization of the developed drive circuit for the gyroscope. Furthermore, improvements to the experimental setup and finally redesign of the device would be logical next steps. The high temperature testing setup for the AlN accelerometers should be used to verify that the devices are indeed capable of measuring acceleration with good sensitivity at temperatures as high as 600 °C. This achievement would be a major success for the developed AlN technology and a milestone towards a new class of micro-electromechanical system (MEMS) harsh environment sensors.

Bibliography

[1] Nuo Zhang and Albert P. Pisano. Harsh environment temperature sensor based on 4h-silicon carbide pn diode. In *17th International Solid-State Sensors, Actuators and Microsystems Conference (Transducers)*, pages 1016–1019, 2013.

[2] Jeff Perkins. Mems everywhere: Sensing the world around you.... and more. In *Semicon West*, San Francisco, 2012.

[3] T sensors summit for trillion sensor roadmap. Stanford Univerisity, 2013.

[4] Peter H. Diamandis and Steven Kotier. *Abundance: The future is better than you think*. Free Press, New York, 2012.

[5] Gianluca Piazza, Valeriy Felmetsger, Paul Muralt, Roy H. Olsson III, and Richard Ruby. Piezoelectric aluminum nitride thin films for microelectromechanical systems. *MRS Bulletin*, 37(11):1051–1061, 2012.

[6] R. H. Olsson, J. G. Fleming, K. E. Wojciechowski, M. S. Baker, and M. R. Tuck. Post-cmos compatible aluminum nitride mems filters and resonant sensors. In *IEEE International Frequency Control Symposium*, pages 412–419, 2007.

[7] G. H. Kroetz, M. H. Eickhoff, and H. Moeller. Silicon compatible materials for harsh environment sensors. *Sensors and Actuators A - Physical*, 74(1-3):182–189, 1999.

[8] Stefn Arnrsson. Geothermal systems in iceland: Structure and conceptual modelsi. high-temperature areas. *Geothermics*, 24(56):561–602, 1995.

[9] Gudmundur O. Fridleifsson and Wilfred A. Elders. The iceland deep drilling project: a search for deep unconventional geothermal resources. *Geothermics*, 34(3):269–285, 2005.

[10] Clair Soares. *Gas turbines: a handbook of air, land, and sea applications*. Elsevier, Burlington, 2008.

[11] W. Challener, S. Palit, R. Jones, L. Airey, R. Craddock, and A. Knobloch. Optical mems pressure sensors for geothermal well monitoring. In *International Workshop on Structural Health Monitoring*, 2013.

[12] Cyril Buttay, Dominique Planson, Bruno Allard, Dominique Bergogne, Pascal Bevilacqua, Charles Joubert, Mihai Lazar, Christian Martin, Herv Morel, Dominique Tournier, and

Christophe Raynaud. State of the art of high temperature power electronics. *Materials Science and Engineering: B*, 176(4):283–288, 2011.

[13] A. C. Patil, Fu Xiao-An, C. Anupongongarch, M. Mehregany, and S. L. Garverick. 6h-sic jfets for 450 degc differential sensing applications. *Journal of Microelectromechanical Systems*, 18(4):950–961, 2009.

[14] N. G. Wright and A. B. Horsfall. Sic sensors: a review. *Journal of Physics D: Applied Physics*, 40(20):6345, 2007.

[15] Roya Maboudian, Carlo Carraro, Debbie G. Senesky, and Christopher S. Roper. Advances in silicon carbide science and technology at the micro- and nanoscales. *Journal of Vacuum Science & Technology A*, 31(5):–, 2013.

[16] M. Mehregany, C. A. Zorman, N. Rajan, and Wu Chien-Hung. Silicon carbide mems for harsh environments. *Proceedings of the IEEE*, 86(8):1594–1609, 1998.

[17] G. Vigevani, F. T. Goericke, A. P. Pisano, I. I. Izyumin, and B. E. Boser. Microleverage detf aluminum nitride resonating accelerometer. In *IEEE International Frequency Control Symposium*, 2012.

[18] Amir Heidari, Yong-Jin Yoon, Man I. Lee, Lynn Khine, Mi Kyoung Park, and Julius Ming Lin Tsai. A novel checker-patterned aln mems resonator as gravimetric sensor. *Sensors and Actuators A: Physical*, 189(0):298–306, 2013.

[19] P Ivaldi, J Abergel, M H Matheny, L G Villanueva, R B Karabalin, M L Roukes, P Andreucci, S Hentz, and E Defa. 50 nm thick aln film-based piezoelectric cantilevers for gravimetric detection. *Journal of Micromechanics and Microengineering*, 21(8):085023, 2011.

[20] M. D. Williams, B. A. Griffin, T. N. Reagan, J. R. Underbrink, and M. Sheplak. An aln mems piezoelectric microphone for aeroacoustic applications. *Microelectromechanical Systems, Journal of*, 21(2):270–283, 2012.

[21] A. Guedes, G. Jaramillo, C. Buffa, G. Vigevani, S. Cardoso, D. C. Leitao, P. P. Freitas, and D. A. Horsley. Towards picotesla magnetic field detection using a gmr-mems hybrid device. *Magnetics, IEEE Transactions on*, 48(11):4115–4118, 2012.

[22] R. J. Przybyla, S. E. Shelton, A. Guedes, I. I. Izyumin, M. H. Kline, D. A. Horsley, and B. E. Boser. In-air rangefinding with an aln piezoelectric micromachined ultrasound transducer. *Sensors Journal, IEEE*, 11(11):2690–2697, 2011.

[23] P Kropelnicki, K-M Muckensturm, X J Mu, A B Randles, H Cai, W C Ang, J M Tsai, and H Vogt. Cmos-compatible ruggedized high-temperature lamb wave pressure sensor. *Journal of Micromechanics and Microengineering*, 23(8):085018, 2013.

[24] J. G. Rodriguez-Madrid, G. F. Iriarte, O. A. Williams, and F. Calle. High precision pressure sensors based on saw devices in the ghz range. *Sensors and Actuators A: Physical*, 189(0):364–369, 2013.

[25] Lev I. Berger. *Semiconductor Materials*. CRC Press, Boca Raton, 1996.

[26] Glen A. Slack, R. A. Tanzilli, R. O. Pohl, and J. W. Vandersande. The intrinsic thermal conductivity of ain. *Journal of Physics and Chemistry of Solids*, 48(7):641–647, 1987.

[27] P. K. Kuo, G. W. Auner, and Z. L. Wu. Microstructure and thermal conductivity of epitaxial aln thin films. *Thin Solid Films*, 253(12):223–227, 1994.

[28] SunRock Choi, Dongsik Kim, Sung-Hoon Choa, Sung-Hoon Lee, and Jong-Kuk Kim. Thermal conductivity of aln and sic thin films. *International Journal of Thermophysics*, 27(3):896–905, 2006.

[29] Gabriele Vigevani. Ph.d. exit talk - mems aluminum nitride technology for inertial sensors. 2011.

[30] V. Felmetsger and P. Laptev. Dual cathode dcrf and mfrf coupled s-guns for reactive sputtering. *Vacuum*, 74(34):403–408, 2004.

[31] W. J. Bartels. Characterization of thin layers on perfect crystals with a multipurpose high resolution x-ray diffractometer. *Journal of Vacuum Science & Technology B*, 1(2):338–345, 1983.

[32] John A. Thornton. The microstructure of sputter-deposited coatings. *Journal of Vacuum Science & Technology A*, 4(6):3059–3065, 1986.

[33] V. V. Felmetsger, P. N. Laptev, and S. M. Tanner. Innovative technique for tailoring intrinsic stress in reactively sputtered piezoelectric aluminum nitride films. *Journal of Vacuum Science & Technology A*, 27(3):417–422, 2009.

[34] Franz Laermer and Andrea Schilp. *Method of anisotropically etching silicon*. Patent, US 5501893, 1996.

[35] Franz Laermer and Andrea Schilp. *Method of anisotropic etching of silicon*. Patent, US 6531068, 2003.

[36] Marc J. Madou. *Fundamentals of microfabrication : the science of miniaturization*. CRC Press, Boca Raton, Fla., 2nd edition, 2002.

[37] Marc J. Madou. *Fundamentals of microfabrication and nanotechnology*. CRC Press, Boca Raton, FL, 3rd edition, 2012.

[38] Gianluca Piazza. *Piezoelectric Aluminum Nitride Vibrating RF MEMS for Radio Front-End Technology*. dissertation, 2005.

[39] Philip Jason Stephanou. *Piezoelectric Aluminum Nitride MEMS Resonators for RF Signal Processing*. dissertation, 2006.

[40] Xu Zhao. *Development of Piezoelectric Aluminum Nitride Anisotropic RIE with 90-degree Sidewall Profile*. Master's thesis, 2008.

[41] B. D. Sosnowchik, R. G. Azevedo, D. R. Myers, M. W. Chan, A. P. Pisano, and Lin Liwei. Rapid silicon-to-steel bonding by induction heating for mems strain sensors. *Journal of Microelectromechanical Systems*, 21(2):497–506, 2012.

[42] Fabian Goericke, Kirti Mansukhani, Kansho Yamamoto, and Albert Pisano. Experimentally validated aluminum nitride based pressure, temperature and 3-axis acceleration sensors integrated on a single chip. In *27th International Conference on Micro Electro Mechanical Systems (MEMS) (accepted)*, 2014.

[43] T. Serikawa, S. Shirai, A. Okamoto, and S. Suyama. Low-temperature fabrication of high-mobility poly-si tfts for large-area lcds. *IEEE Transactions on Electron Devices*, 36(9):1929–1933, 1989.

[44] S. Saravanan, E. Berenschot, G. Krijnen, and M. Elwenspoek. A novel surface micromachining process to fabricate aln unimorph suspensions and its application for rf resonators. *Sensors and Actuators A - Physical*, 130131(0):340–345, 2006.

[45] K. E. Wojciechowski, R. H. Olsson, M. R. Tuck, E. Roherty-Osmun, and T. A. Hill. Single-chip precision oscillators based on multi-frequency, high-q aluminum nitride mems resonators. In *15th International Solid-State Sensors, Actuators and Microsystems Conference (Transducers)*, pages 2126–2130, 2009.

[46] K. Azgin, T. Akin, and L. Valdevit. Ultrahigh-dynamic-range resonant mems load cells for micromechanical test frames. *Journal of Microelectromechanical Systems*, 21(6):1519–1529, 2012.

[47] M. Ferri, L. Belsito, F. Mancarella, L. Masini, A. Roncaglia, J. Yan, A. A. Seshia, J. Zalesky, and K. Soga. Fabrication and testing of a high resolution extensometer based on resonant mems strain sensors. In *16th International Solid-State Sensors, Actuators and Microsystems Conference (Transducers)*, pages 1056–1059, 2011.

[48] S. Jiang, D. Zhang, L. Lin, Z. Yang, and G. Yan. Silicon probe for micromachined surface profilers. *IET Micro & Nano Letters*, 6(7):490–493, 2011.

[49] M. W. Chan, D. R. Myers, B. D. Sosnowchik, Lin Liwei, and A. P. Pisano. Localized strain sensing using high spatial resolution, highly-sensitive mems resonant strain gauges for failure prevention. In *16th International Solid-State Sensors, Actuators and Microsystems Conference (Transducers)*, pages 2859–2862, 2011.

[50] K. Azgin, C. Ro, A. Torrents, T. Akin, and L. Valdevit. A resonant tuning fork force sensor with unprecedented combination of resolution and range. In *24th International Conference on Micro Electro Mechanical Systems (MEMS)*, pages 545–548, 2011.

[51] Senlin Jiang, Dacheng Zhang, Zhengchuan Yang, and Guizhen Yan. Design and fabrication of a novel silicon probe for micromachined surface profilers. In *5th IEEE International Conference on Nano/Micro Engineered and Molecular Systems (NEMS)*, pages 941–944, 2010.

[52] R. G. Azevedo, Zhang Jingchun, D. G. Jones, D. R. Myers, A. V. Jog, B. Jamshidi, M. B. J. Wijesundara, R. Maboudian, and A. P. Pisano. Silicon carbide coated mems strain sensor for harsh environment applications. *20th IEEE International Conference on Micro Electro Mechanical Systems (MEMS) 2007*, pages 643–646, 2007.

[53] K. E. Wojciechowski, B. E. Boser, and A. P. Pisano. A mems resonant strain sensor operated in air. In *17th IEEE International Conference on Micro Electro Mechanical Systems (MEMS)*, pages 841–845, 2004.

[54] K. E. Wojciechowski, B. E. Boser, and A. P. Pisano. A mems resonant strain sensor with 33 nano-strain resolution in a 10 khz bandwidth. In *IEEE Sensors*, page 4 pp., 2005.

[55] Seonho Seok, Hak Kim, and Chun Kukjin. An inertial-grade laterally-driven mems differential resonant accelerometer. In *IEEE Sensors*, pages 654–657 vol.2, 2004.

[56] Jia Yu-bin, Hao Yi-long, and Zhang Rong. Double tuning-fork resonant accelerometer. In *7th International Conference on Solid-State and Integrated Circuits Technology*, pages 1812–15 vol.3, 2005.

[57] S. X. P. Su, H. S. Yang, and A. M. Agogino. A resonant accelerometer with two-stage microleverage mechanisms fabricated by soi-mems technology. *IEEE Sensors Journal*, 5(6):1214–1223, 2005.

[58] E. J. Ng, Lee Hyung Kyu, C. H. Ahn, R. Melamud, and T. W. Kenny. Stability measurements of silicon mems resonant thermometers. In *IEEE Sensors*, pages 1257–1260, 2011.

[59] R. G. Hennessy, M. M. Shulaker, M. W. Messana, A. B. Graham, N. Klejwa, J. Provine, T. W. Kenny, and R. T. Howe. Temperature dependence of vacuum encapsulated resonators for humidity measurement. In *16th International Solid-State Sensors, Actuators and Microsystems Conference (Transducers)*, pages 1950–1953, 2011.

[60] P. Thiruvenkatanathan, J. Yan, and A. A. Seshia. Ultrasensitive mode-localized micromechanical electrometer. In *IEEE International Frequency Control Symposium*, pages 91–96, 2010.

[61] E. Marigo, J. L. Munoz-Gamarra, J. Giner, J. L. Lopez, F. Torres, A. Uranga, N. Barniol, and J. Verd. Linear operation of a 11mhz cmos-mems resonator. In *IEEE International Frequency Control Symposium*, pages 158–161, 2010.

[62] J. L. Munoz-Gamarra, E. Marigo, J. Giner, A. Uranga, F. Torres, and N. Barniol. Characterization of cmos-mems resonator by pulsed mode electrostatic actuation. In *IEEE International Frequency Control Symposium*, pages 415–418, 2010.

[63] S. T. Bartsch, D. Grogg, A. Lovera, D. Tsamados, and A. M. Ionescu. Very high frequency double-ended tuning fork nano-mechanical fin-fet resonator. *16th International Solid-State Sensors, Actuators and Microsystems Conference (Transducers)*, pages 938–941, 2011.

[64] David R. Myers, Kan Bun Cheng, Babak Jamshidi, Robert G. Azevedo, Debbie G. Senesky, Li Chen, Mehran Mehregany, Muthu B. J. Wijesundara, and Albert P. Pisano. Silicon carbide resonant tuning fork for microsensing applications in high-temperature and high g-shock environments. *Journal of Micro/Nanolithography, MEMS, and MOEMS*, 8(2):021116–021116, 2009.

[65] D. R. Myers, R. G. Azevedo, Chen Li, M. Mehregany, and A. P. Pisano. Passive substrate temperature compensation of doubly anchored double-ended tuning forks. *Journal of Microelectromechanical Systems*, 21(6):1321–1328, 2012.

[66] J. X. Liang, X. F. Li, H. S. Li, Y. F. Ni, K. Y. Li, L. B. Huang, and T. Ueda. Design and fabrication of quartz micro-electro-mechanical system-based double-ended tuning fork with variable sections. *Japanese Journal of Applied Physics*, 50(6), 2011.

[67] Jinxing Liang, Xuefeng Li, Yunfang Ni, Hongsheng Li, Libin Huang, and Kunyu Li. Formation of side electrode on quartz mems-based double-ended tuning fork using enhanced lift-off process. *Advanced Materials Research*, 328-330:507–510, 2011.

[68] Santiram Kal and Soumen Das. Development of silicon and quartz based mems high precision accelerometers. *Indian Journal of Pure and Applied Physics*, 45(4):299–303, 2007.

[69] G. Vigevani, R. J. Przybyla, Yen Ting-Ta, Lin Chih-Ming, A. Guedes, J. H. Kuypers, B. E. Boser, D. A. Horsley, and A. P. Pisano. Characterization of a single port aluminum nitride tuning fork. In *IEEE International Ultrasonics Symposium*, pages 1281–1285, 2010.

[70] F. T. Goericke, M. W. Chan, G. Vigevani, I. Izyumin, B. E. Boser, and A. P. Pisano. High temperature compatible aluminum nitride resonating strain sensor. In *16th International Solid-State Sensors, Actuators and Microsystems Conference (Transducers)*, pages 1994–1997, 2011.

[71] R. H. Olsson, K. E. Wojciechowski, M. S. Baker, M. R. Tuck, and J. G. Fleming. Post-cmos-compatible aluminum nitride resonant mems accelerometers. *Journal of Microelectromechanical Systems*, 18(3):671–678, 2009.

[72] Don L. DeVoe. Piezoelectric thin film micromechanical beam resonators. *Sensors and Actuators A - Physical*, 88(3):263–272, 2001.

[73] Singiresu S. Rao. *Mechanical Vibrations*. Addison-Wesley, Old Tappan, 2nd edition, 1990.

[74] Gabriele Vigevani. *MEMS Aluminum Nitride Technology for Inertial Sensors*. Ph.d. thesis, 2011.

[75] G. Vigevani, F. T. Goericke, I. I. Izyumin, B. E. Boser, and A. P. Pisano. Electrode design and coupling optimization of aluminum nitride detf. In *IEEE International Ultrasonics Symposium*, pages 1731–1734, 2011.

[76] R. Lifshitz and M. L. Roukes. Thermoelastic damping in micro- and nanomechanical systems. *Physical Review B*, 61(8):5600–5609, 2000.

[77] G. Vigevani, J. Kuypers, and A. P. Pisano. Piezo thermoelastic model for design optimization of resonant beams. In *IEEE International Ultrasonics Symposium*, pages 1536–1539, 2008.

[78] H. Hosaka, K. Itao, and S. Kuroda. Damping characteristics of beam-shaped micro-oscillators. *Sensors and Actuators A - Physical*, 49(1-2):87–95, 1995.

[79] F. R. Blom, S. Bouwstra, M. Elwenspoek, and J. H. J. Fluitman. Dependence of the quality factor of micromachined silicon beam resonators on pressure and geometry. *Journal of Vacuum Science & Technology B*, 10(1):19–26, 1992.

[80] Volker Kempe. *Inertial MEMS: principles and practice*. Cambridge University Press, Cambridge, 2011.

[81] S. Bouwstra and B. Geijselaers. On the resonance frequencies of microbridges. In *International Solid-State Sensors and Actuators Conference (Transducers)*, pages 538–542, 1991.

[82] Min-hang Bao. *Micro Mechanical Transducers*, volume 8 of *Handbook of Sensors and Actuators*. Elsevier Science B.V., 2000.

[83] Analog Devices. Precision 1.7 g, 5 g, 18 g single-/dual-axis imems accelerometer. *datasheet*, 2011.

[84] Fabian T. Goericke, Gabriele Vigevani, and Albert P. Pisano. Bent-beam sensing with triple-beam tuning forks. *Applied Physics Letters*, 102(25):253508, 2013.

[85] Laurie E. McNeil, Marcos Grimsditch, and Roger H. French. Vibrational spectroscopy of aluminum nitride. *Journal of the American Ceramic Society*, 76(5):1132–1136, 1993.

[86] T. Fabula, H. J. Wagner, B. Schmidt, and S. Buttgenbach. Triple-beam resonant silicon force sensor-based on piezoelectric thin-films. *Sensors and Actuators A - Physical*, 42(1-3):375–380, 1994.

[87] Fabian T Goericke, Gabriele Vigevani, Igor I Izyumin, Bernhard E Boser, and Albert P Pisano. Novel thin-film piezoelectric aluminum nitride rate gyroscope. In *IEEE International Ultrasonics Symposium*, pages 1067–1070. IEEE, 2012.

[88] N. D. Patel and P. S. Nicholson. High frequency, high temperature ultrasonic transducers. *NDT International*, 23(5):262–266, 1990.

[89] J. Castaing, P. Veyssire, L. P. Kubin, and J. Rabier. The plastic deformation of silicon between 300c and 600c. *Philosophical Magazine A*, 44(6):1407–1413, 1981.

[90] P. Boch, J. C. Glandus, J. Jarrige, J. P. Lecompte, and J. Mexmain. Sintering, oxidation and mechanical properties of hot pressed aluminium nitride. *Ceramics International*, 8(1):34–40, 1982.

[91] Zuel Chown Jou and Anil V. Virkar. High-temperature creep and cavitation of polycrystalline aluminum nitride. *Journal of the American Ceramic Society*, 73(7):1928–1935, 1990.

[92] Robert Hull. *Properties of Crystalline Silicon*. The Institution of Electrical Engineers, London, 1999.

[93] Chung-Seog Oh, George Coles, and William N. Sharpe. High temperature behavior of polysilicon. *MRS Online Proceedings Library*, 741:null–null, 2002.

[94] Ichiro Yonenaga, Andrey Nikolaev, Yuriy Melnik, and Vladimir Dmitriev. High-temperature hardness of bulk single-crystal aln. *MRS Online Proceedings Library*, 693:null–null, 2001.

[95] I. Yonenaga. High-temperature strength of bulk single crystals of iii-v nitrides. *Journal of Materials Science: Materials in Electronics*, 14(5-7):279–281, 2003.

[96] Dragan Damjanovic. Materials for high temperature piezoelectric transducers. *Current Opinion in Solid State and Materials Science*, 3(5):469–473, 1998.

[97] Sergey L. Rumyantsev, Michael S. Shur, and Michael E. Levinshtein. Materials properties of nitrides: Summary. *International Journal of High Speed Electronics and Systems*, 14(01):1–19, 2004.

[98] G.A. Slack and S.F. Bartram. Thermal expansion of some diamond-like crystals. *Journal of Applied Physics*, 46(1):89–98, 1975.

Appendix A

Fabrication process for surface-micromachined, bottom-up fabrication

Step	Action	Tool	Parameters
Insulation layer			
1.1	Obtain wafers		6”, p-type, prime-grade
1.2	Measure first curvature	flexus	
1.3	Furnace-clean	msink6	piranha clean, quick dump rinse, 1 min in 25:1 HF, quick dump rinse, spin rinse dry
1.4	Low stress nitride deposition	tystar17	lsnstda.017 (100 DCS, 25 HN3, 140 mTorr, 835 °C, 91 min, goal: 3000 Å
1.5	Measure film thickness	nanospec	5 measurements, program: 002 (SiN on Si 10x)
Bottom electrode layer			
2.1	HMDS priming	primeoven	program: 0 (1 min HMDS)
2.2	Spin OCG 825 (g-line) photoresist	svgcoat1	coater program: 2 (speed: 5000 rpm), oven program: 1 (temperature: 90 °C, time: 1 min), goal: 13000 Å
2.3	Spin OiR 10i (i-line) photoresist	svgcoat1	coater program: 1 (speed: 4100 rpm), oven program: 1 (temperature: 90 °C, time: 1 min), goal: 11000 Å
2.4	Expose photoresist	gcaws6	job file: fabian, pass: 1, mask: botelec, using best exposure time and focus from test run (typical: 1.78 sec)
2.5	Expose four center dies with blank mask	gcaws6	job file: fabian, pass: 2, mask: Berlin blank
2.6	Develop photoresist	sink	CD-30, 3 min, constant agitation

Continued on next page

Continued from previous page

Step	Action	Tool	Parameters
2.7	Deposit adhesion layer		outsourced, goal: 50 Å chromium
2.8	Deposit bottom electrode layer		outsourced, goal: 1000 Å platinum
2.9	Lift off photoresist	sink	acetone bath 10 min, acetone rinse, second acetone bath with sonication, acetone rinse, IPA bath, IPA rinse, nitrogen dry
2.10	Measure bottom electrode thickness	asiq	different areas on wafer
2.11	Measure resistance	probestation	THE feature in different areas on wafer
Aluminum nitride layer			
3.1	Dehydrate wafers	vacoven	60 min, 350 °C
3.2	Deposit aluminum nitride	aln2	current recipe, goal: 20000 Å, 0 MPa
3.3	Measure film thickness on test wafer	nanospec	program: AlN on Si
3.4	Measure film quality (FWHM)	xdif	in area of four blank center dies; chi-scan -5°to 5°, step 0.1°, find peak; then rocking curve 10°to 26°, step 0.01°using chi-offset, run 3 times
Top electrode layer			
4.1	Pre-clean	sink	ammonium hydroxide dip (temperature: 20 °C, time: 20 sec), DI water rinse, nitrogen dry
4.2	HMDS priming	primeoven	program: 0 (1 min HMDS)
4.3	Spin OCG 825 (g-line) photoresist	svgcoat1	coater program: 2 (speed: 5000 rpm), oven program: 1 (temperature: 90 °C, time: 1 min), goal: 13000 Å
4.4	Spin OiR 10i (i-line) photoresist	svgcoat1	coater program: 1 (speed: 4100 rpm), oven program: 1 (temperature: 90 °C, time: 1 min), goal: 11000 Å
4.5	Expose photoresist	gcaws6	job file: fabian, using microDFAS, mask: topelec, using best exposure time and focus from test run
4.6	Develop photoresist	sink	CD-30, 3 min, constant agitation
4.7	Deposit adhesion layer		outsourced, goal: 50 Å chromium
4.8	Deposit bottom electrode layer		outsourced, goal: 1000 Å platinum

Continued on next page

Continued from previous page

Step	Action	Tool	Parameters
4.9	Lift off photoresist	sink	acetone bath 10 min, acetone rinse, second acetone bath with sonication, acetone rinse, IPA bath, IPA rinse, nitrogen dry
4.10	Measure top electrode thickness	asiq	different areas on wafer
Bottom electrode contacts			
5.1	HMDS priming	primeoven	program: 0 (1 min HMDS)
5.2	Spin OiR 10i (i-line) photoresist	svgcoat1	coater program: 6 (speed: 820 rpm), oven program: 1 (temperature: 90 °C, time: 1 min), goal: 28000 Å
5.3	Expose photoresist	gcaws6	job file: fabian, pass: 1, mask: alnvia, using best exposure time and focus from test run
5.4	Develop photoresist	sink	CD-30, 3 min, constant agitation
5.5	UV bake photoresist	uvbake	program: S
5.6	Etch aluminum nitride	sink	ammonium hydroxide dip (temperature: 20 °C, time: 20 sec), phosphoric acid bath (temperature: 130 °C, time: 1 min), DI water rinse, nitrogen dry; repeat all steps until aluminum nitride completely removed in openings
5.7	Verify opening	probestation	confirm resistance of THE fetures
5.8	Remove photoresist	matrix	pressure: 3.75 Torr, MFC1: 40 %, RF power: 400 W, chuck temperature: 250 °C; 3x2:30 min, repeat if necessary
5.9	Solvent wafer clean	sink	acetone bath 30 min, acetone rinse, second acetone bath, acetone rinse, IPA bath, IPA rinse, DI water rinse, nitrogen dry
Aluminum nitride patterning			
6.1	Silicon dioxide deposition	tystar12	program: 12LTO400 (SiH: 90 sccm, O2: 135 sccm, temperature: 400 °C), goal: 13000 Å, typical deposition rate: 108 Å/min
6.2	HMDS priming	primeoven	program: 0 (1 min HMDS)
6.3	Spin OiR 10i (i-line) photoresist	svgcoat1	coater program: 1 (speed: 4100 rpm), oven program: 1 (temperature: 90 °C, time: 1 min), goal: 11000 Å
6.4	Expose photoresist	gcaws6	job file: fabian, using microDFAS, mask: alnetch, using best exposure time and focus from test run (typical: 2.14 sec/0)
6.5	Develop photoresist	sink	CD-30, 3 min, constant agitation
6.6	UV bake photoresist	uvbake	program: S

Continued on next page

Continued from previous page

Step	Action	Tool	Parameters
6.7	Etch oxide mask	centura-mxp	first run clean recipe on dummy wafer, recipe: O2_CLEAN_MXP (power: 300 W, pressure: 200 mTorr, O2: 50 sccm, magnet: 20 G); then run etch recipe on device wafer: MXP_OX_VAR (power: 1000 W, pressure: 45 mTorr, CHF3: 30 sccm, CF4: 15 sccm, Ar: 100 sccm, magnet: 30 G), perform in increments until oxide is etched through, typical etch rate: 3840 Å/min
6.8	Remove photoresist	matrix	pressure: 3.75 Torr, MFC1: 40 %, RF power: 400 W, chuck temperature: 250 °C; time: 2:30, repeat if necessary
6.9	Solvent wafer clean	sink	acetone bath 30 min, acetone rinse, second acetone bath, acetone rinse, IPA bath, IPA rinse, DI water rinse, nitrogen dry
6.10	Etch aluminum nitride	centura-met	first run clean recipe on dummy wafer, recipe: O2_CLEAN_MET (power: 300 W, bias: 70 W, pressure: 10 mTorr, Ar: 100 sccm); then run etch recipe on device wafer: ALNVAR (power: 500 W, bias: 70 W, pressure: 10 mTorr, Cl2: 90 sccm, BCl3: 10 sccm, Ar: 100 sccm), perform in increments until aluminum nitride is etched through, typical etch rate: 1450 Å/min
6.11	Verify etch through	probestation	check if conductivity in AlNetch test feature is not infinite (silicon surface has been reached)
Device release			
7.1	Spin OiR 10i (i-line) photoresist	svgcoat1	coater program: 1 (speed: 4100 rpm), oven program: 1 (temperature: 90 °C, time: 1 min), goal: 11000 Å
7.2	Dice wafer	disco	pitch in x- and y-directions: 10160 µm
7.3	Solvent clean of dies	sink	acetone bath 30 min, second acetone bath, IPA bath, IPA rinse, nitrogen dry
7.4	Remove oxide mask	sink	BHF 5:1 bath 4 min, DI water bath, second DI water bath, DI water rinse, nitrogen dry; repeat for shorter time if silicon dioxide not completely removed
7.5	Check electrical contact	probestation	top and bottom electrode features
7.6	Dehydrate dies	hotplate	300 °C, 2 min

Continued on next page

Continued from previous page

Step	Action	Tool	Parameters
7.7	Silicon etch	xetch	etch time per cycle: 30 sec, XeF2 pressure: 4 Torr, N2 pressure: 2 Torr; typical etch rate: 4600 Å/min, typical number of cycles: 50, run in increments until all features completely released, perform dehydration before each run
7.8	Check proof mass release	probestation	move proof mass with probetip

Appendix B

Fabrication process for surface- and bulk-micromachined, top-down fabrication

Step	Action	Tool	Parameters
Initial wafer preparation			
1.1	Obtain wafers		6”, p-type, double-sided polished
1.2	Mark wafers	diamon scribe	number on backside near wafer flat
1.3	Measure thickness	micrometer at flexus	
1.4	Measure curvature	flexus	at 0°and at 90°
1.5	Clean wafer, non-MOS	msink8	10 min Piranha at 120 °C, quick dump rinse, 1 min 5:1 BHF, quick dumpe rinse, spin rinse dry
1.5	Clean wafer, MOS	msink6	10 min Piranha at 120 °C, quick dump rinse, 1 min 5:1 BHF, quick dumpe rinse, spin rinse dry
Layer stack deposition			
2.1	First AlN layer	aln2	use current recipe, target: 10000 Å, 0 MPa
2.2	Measure rocking curve	xdif	target: 1.4°
2.3	Measure film thickness	nanospec	program: AlN on Si
2.4	Measure film stress	flexus	at 0°and at 90°
2.5	First molybdenum layer	aln2	use current recipe, target: 1000 Å, 0 MPa
2.6	Measure rocking curve	xdif	target: 2.1°
2.7	Measure film stress	flexus	at 0°and at 90°
2.8	Second AlN layer	aln2	use current recipe, target: 10000 Å, 0 MPa

Continued on next page

Continued from previous page

Step	Action	Tool	Parameters
2.9	Measure rocking curve	xdif	target: 1.6°
2.10	Measure film stress	flexus	at 0°and at 90°
2.11	Second molybdenum layer	aln2	use current recipe, target: 1000 Å, 0 MPa
2.12	Measure film stress	flexus	at 0°and at 90°
2.13	Titanium layer	edwardseb3	target: 75 Å
Pattern photoresist for top electrode patterning			
3.1	Dehydration	hotplate	130 °C, 10 min
3.2	Spin OiR 10i (i-line) photoresist	svgcoat1	coater program: 1 (speed: 4100 rpm), oven program: 1 (temperature: 90 °C, time: 1 min), goal: 11000 Å
3.3	Expose photoresist	gcaws6	job file: fabian, pass: 1, mask: NISSAN - Top Electrode, using best exposure time and focus from test run (typical: 2.5 sec)
3.4	Post exposure bake and development	svgdev6	post exposure bake program: 1 (temperature: 130 °C, time: 60 sec), development program: 3 (developer: OPD4262, time: 60 sec), no hard bake (program: 9)
3.5	UV bake photoresist	uvbake	program: S
Top electrode patterning			
4.1	Etch Ti/TiO	centura-met	recipe: MET AL-ME (power: 1000 W, bias: 100 W, pressure: 10 mTorr, Cl2: 90 sccm, BCl3: 45 sccm), time: 10 sec
4.2	Etch molybdenum	centura-met	recipe: MOLYVAR (power: 300 W, bias: 100 W, pressure: 10 mTorr, Cl2: 135 sccm, O2: 15 sccm), time: 60 sec, repeat until molybdenum etched through
4.3	Remove photoresist	matrix	pressure: 3.75 Torr, MFC1: 40 %, RF power: 400 W, chuck temperature: 250 °C; time: 2:30 min, repeat if necessary
4.4	Measure top electrode thickness	asiq	different areas on wafer
4.5	Remove Ti/TiO	centura-met	recipe: MET AL-ME (power: 1000 W, bias: 100 W, pressure: 10 mTorr, Cl2: 90 sccm, BCl3: 45 sccm), time: 10 sec
4.6	Measure top electrode thickness	asiq	different areas on wafer
Pattern photoresist for via patterning			
5.1	HMDS priming	primeoven	program: 2 (2 min HMDS)

Continued on next page

Continued from previous page

Step	Action	Tool	Parameters
5.2	Spin OiR 10i (i-line) photoresist	svgcoat1	coater program: 5 (speed: 1300 rpm), oven program: 1 (temperature: 90 °C, time: 1 min), goal: 20000 Å
5.3	Expose photoresist	gcaws6	job file: fabian, using microDFAS, mask: NISSAN - AlN Via Etch, using best exposure time and focus from test run (typical: 7 sec)
5.4	Post exposure bake and development	svgdev6	post exposure bake program: 1 (temperature: 130 °C, time: 60 sec), development program: 3 (developer: OPD4262, time: 60 sec), no hard bake (program: 9)
5.5	UV bake photoresist	uvbake	program: S
Bottom electrode patterning			
6.1	Etch aluminum nitride	sink	ammonium hydroxide dip (temperature: 20 °C, time: 15 sec), phosphoric acid bath (temperature: 130 °C, time: 30 sec), DI water rinse, nitrogen dry; repeat all steps until aluminum nitride completely removed in openings
6.2	Remove photoresist	matrix	pressure: 3.75 Torr, MFC1: 40 %, RF power: 400 W, chuck temperature: 250 °C; time: 2:30 min, repeat if necessary
6.3	Remove oxidized molybdenum	centura-met	recipe: MOLYVAR (power: 300 W, bias: 100 W, pressure: 10 mTorr, Cl2: 135 sccm, O2: 15 sccm), time: 5 sec (surface turns from golden to silverish)
Deposit hardmask oxide			
7.1	Solvent wafer clean	sink	acetone bath 10 min, acetone rinse, second acetone bath, acetone rinse, IPA bath, IPA rinse, DI water rinse, nitrogen dry
7.2	Silicon dioxide deposition	tystar12	program: 12LTO400 (SiH: 90 sccm, O2: 135 sccm, temperature: 400 °C), bookend by silicon wafers, goal: 16500 Å, typical deposition rate: 100 Å/min
7.3	nanospec	Measure silicon dioxide thickness	on silicon wafers, program: oxide on silicon
Pattern oxide hardmask			
8.1	HMDS priming	primeoven	program: 2 (2 min HMDS)
8.2	Spin OiR 10i (i-line) photoresist	svgcoat1	coater program: 1 (speed: 4100 rpm), oven program: 1 (temperature: 90 °C, time: 1 min), goal: 11000 Å

Continued on next page

Continued from previous page

Step	Action	Tool	Parameters
8.3	Expose photoresist	gcaws6	job file: fabian, using microDFAS, mask: NISSAN - AlN Feature Etch, using best exposure time and focus from test run (typical: 2 sec)
8.4	Post exposure bake and development	svgdev6	post exposure bake program: 1 (temperature: 130 °C, time: 60 sec), development program: 3 (developer: OPD4262, time: 60 sec), no hard bake (program: 9)
8.5	UV bake photoresist	uvbake	program: S
AlN/molybdenum/AlN stack patterning			
9.1	Etch silicon dioxide	sts-oxide	program: kansho, about 8 min in 2 min intervals, repeat if necessary
9.2	Remove photoresist	matrix	pressure: 3.75 Torr, MFC1: 40 %, RF power: 400 W, chuck temperature: 250 °C; time: 2x2:30 min, repeat if necessary
9.3	Etch AlN/molybdenum/ AlN	centura-met	recipe: ALNVAR (power: 500 W, bias: 70 W, pressure: 10 mTorr, Cl2: 90 sccm, BCl3: 10 sccm, Ar: 100 sccm), about 10 min in 2 min intervals, repeat if necessary
Deposit additional oxide for backside mask			
10.1	Silicon dioxide deposition	tystar12	program: 12LTO400 (SiH: 90 sccm, O2: 135 sccm, temperature: 400 °C), bookend by silicon wafers, goal: 16500 Å, typical deposition rate: 100 Å/min
10.2	nanospec	Measure silicon dioxide thickness	on silicon wafers, program: oxide on silicon
Pattern photoresist for backside oxide patterning			
11.1	Clean backside	matrix	pressure: 3.75 Torr, MFC1: 40 %, RF power: 400 W, chuck temperature: 250 °C; time: 2:30 min
11.2	HMDS priming	primeoven	program: 2 (2 min HMDS)
11.3	Spin OiR 10i (i-line) photoresist	svgcoat1	coater program: 5 (speed: 1300 rpm), oven program: 1 (temperature: 90 °C, time: 1 min), goal: 20000 Å
11.4	Expose photoresist	ksaligner	mask: NISSAN - backside 1, backside alignment to NISSAN - Top Electrode alignment mark, hardcontact, typical exposure time: 12 sec

Continued on next page

Continued from previous page

Step	Action	Tool	Parameters
11.5	Development	svgdev6	no post exposure bake (program: 9), development program: 3 (developer: OPD4262, time: 60 sec), no hard bake (program: 9)
11.6	UV bake photoresist	uvbake	program: S
Backside oxide patterning			
12.1	Etch silicon dioxide	sts-oxide	program: kansho, about 8 min in 2 min intervals, repeat if necessary
12.2	Remove photoresist	matrix	pressure: 3.75 Torr, MFC1: 40 %, RF power: 400 W, chuck temperature: 250 °C; time: 2:30 min, repeat if necessary
Pattern thick photoresist for deep silicon backside etch			
13.1	HMDS priming	primeoven	program: 2 (2 min HMDS)
13.2	Spin OCG 825 (g-line) photoresist	svgcoat1	coater programs: 2x2 (speed: 5000 rpm) + 2x4 (speed: 2200 rpm), oven program: 1 (temperature: 90 °C, time: 1 min) after each coating step, goal: (2x13000 Å+2x20000 Å=66000 Å
13.3	Expose photoresist	ksaligner	mask: NISSAN - Backside 2, frontside alignment to NISSAN - Backside 1 alignment mark, hardcontact, multiple exposure: 3x(20 sec exposure, 10 sec interval)
13.4	Development	svgdev6	no post exposure bake (program: 9), development program: 2x2 (developer: OCG 934 2:1, time: 60 sec), no hard bake (program: 9)
13.5	Hardbake	oven	120 °C, 120 min
First deep backside etch step			
14.1	Etch backside silicon	sts2	program: kirti, etch until reaching 450 µm trench depth (determine etch rate for 30 min etch first, then steps of max. 60 min)
14.2	Remove photoresist	matrix	pressure: 3.75 Torr, MFC1: 40 %, RF power: 400 W, chuck temperature: 250 °C; time: 2:30 min, repeat several times until all photoresist is removed
Attach device wafer to handle wafer			
15.1	Melt crystalbond onto handle wafer	hotplate	oxide covered handle wafer (several micro m), 140 °C, melt crystalbond on hot handle wafer surface, spread with glass slide
15.2	Place device wafer on handle wafer	hotplate	140 °C, place device wafer on handle wafer, rotate with tweezers to improve bond and align flats

Continued on next page

Continued from previous page

Step	Action	Tool	Parameters
15.3	Cooldown procedure	hotplate	transfer wafer stack to hotplat at 110 °C, wait 2 min, turn off hotplate, leave on hotplate until room temperature is reached
Final deep backside etch step			
16.1	Etch backside silicon	sts2	program: kirti, etch until all features are completely opened
Remove handle wafer			
17.1	Long acetone soak	sink	leave in covered crystallizing dish with acetone for 12 hours
17.2	Second acetone bath	sink	transfer individual devices right side up to second crystallizing dish with aceton
17.3	Isopropanol bath	sink	transfer individual devices right side up to crystallizing dish with isopropanol
17.4	Air dry	sink	transfer individual devices to TexWipe and let dry in air, then move to Gel-Pak
Remove oxide			
18.1	Off-gas dies	hotplate	250 °, 2 min
18.2	Etch in HF vapor	primaxx	program: Recipe2 (N2: 1250 sccm, EtOH: 350 sccm, HF: 310 sccm, R: 5.5), time: 5 min, check if oxide completely removed, add additional 1 min etch steps if necessary

Appendix C

Circuit diagram of quad 2-stage amplifier

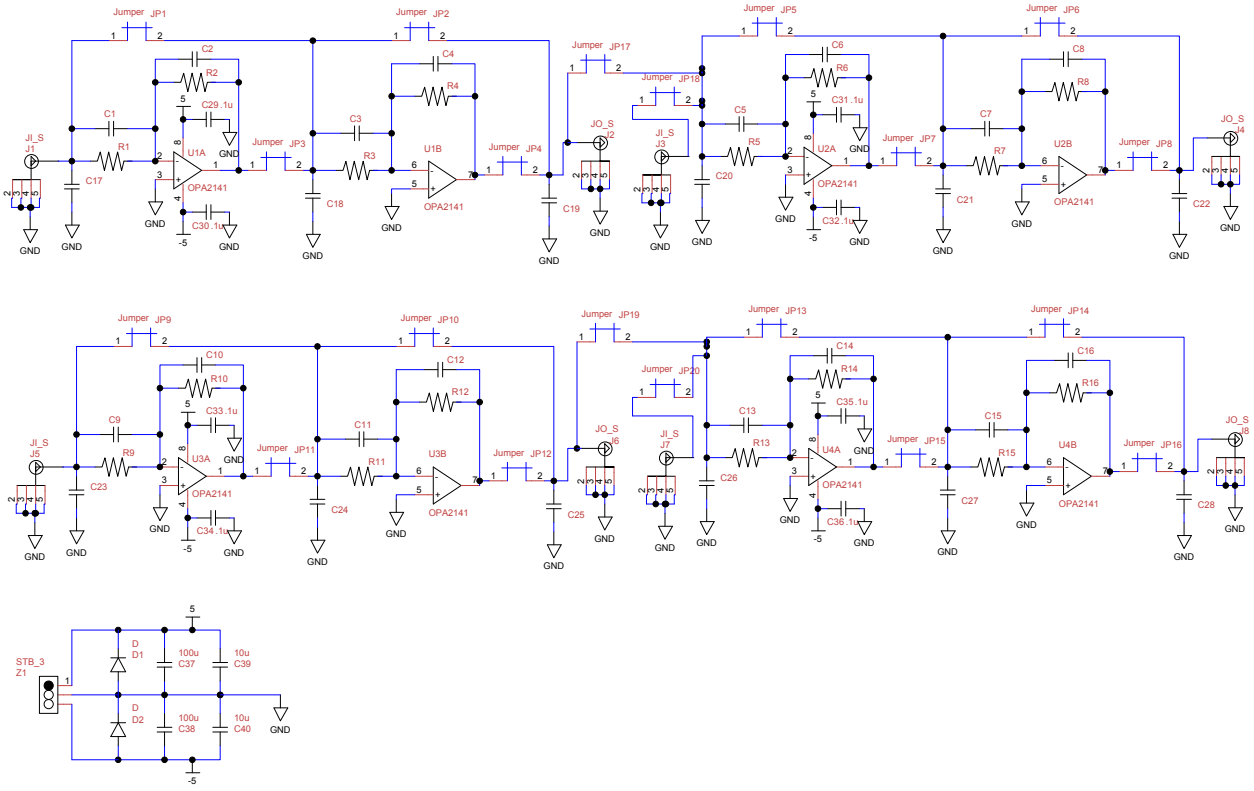

Appendix D

MATLAB code for resonance frequency extraction

```
clear;
peakarray=zeros(20,2);
foldername=strcat('D:\FileLocation\');
oldfolder=pwd;
cd(foldername);
frequency=xlsread('Data.csv','B:B');
amplitude=xlsread('Data.csv','C:C');
amplsmooth1=smooth(amplitude,10,'loess');
[pks,locs]=findpeaks(amplsmooth1,'minpeakdistance',4,'threshold',1e-6,
'npeaks',20);
for j=1:length(locs)
    peakarray(j,1)=frequency(locs(j));
    peakarray(j,2)=amplitude(locs(j));
end
hold on
plot(frequency,amplitude,'-b')
plot(frequency,amplsmooth1,'-r')
plot(peakarray(:,1),peakarray(:,2),'o')
hold off
cd(oldfolder);
```

Appendix E

ANSYS code for tuning fork accelerometer

```
finish
/clear

*dim,materialsfile,string,248
*dim,maindirectory,string,248
maindirectory(1)='D:\Dropbox\Research\ANSYS\NISSAN_Inclinometer'!for local
machine
!maindirectory(1)='I:\Fabian\NISSAN_Inclinometer'!for OOBA
materialsfile(1)='D:\Dropbox\ANSYS\common_functions\materials_v4'!for
local machine
!materialsfile(1)='I:\Fabian\common_functions\materials_v4'!for OOBA
*afun,deg

*get,xdate,active,0,dbase,ldate
*get,xtime,active,0,dbase,ltime
string1 = strcat(chrval(xdate),'_')
resultsstring = strcat(string1,chrval(xtime))

usebaseplate=0 !1: yes, 0: no
DETF=1 !1: out-of-plane (TBTF), 2: in-plane (DETF)
proofmass=1 !1: yes, 0: no
modalanalysis=1 !1: perform modal analysis, 0: do not perform modal
analysis
nonlinearanalysis=0 !1: yes (non-linear geometry), 2: no (no non-linear
geometry)
guidedmass=0 !1: proofmass can not move in z-direction, 0: proof mass is
free to move in all directions
fixedmass=1 !1: bottom of proofmass is fixed in x,y,z
predeformed=0 !0: don't tranfer deformations from static analysis to modal
analysis, 1: transfer deformations from static analysis to modal analysis
```

```
!**** Out-of-plane DETF dimensions
w_beam=24
w_beam=24
s_beam=6
l_beam=300
w_anchor=80
l_anchor=20
h_AlN1=1
h_botelec=0.1
h_AlN2=1
!****

!**** In-plane DETF dimensions
w_tether_IP=8
l_tether_IP=30
w_anchor_IP=32
l_anchor_IP=30
l_beam_IP=300
w_beam_IP=6
s_beam_IP=10
h_AlN_IP=2
!****

h_bulk=320
!tilt=120
stressdiff=110

*dim,fmatrix,array,31,1

/prep7
/nopr
/output,%resultsstring%,csv
*if,proofmass,eq,1,then
*vwrite
('Use of proof mass,yes')
*else
*vwrite
('Use of proofmass,no')
*endif

*if,usebaseplate,eq,1,then
*vwrite
('Use of baseplate,yes')
*else
*vwrite
```

```
('Use of baseplate,no')
*endif

*if,nonlinearanalysis,eq,1,then
*vwrite
('Non-linear geometry,yes')
*else
*vwrite
('Non-linear geometry,no')
*endif

*if,guidedmass,eq,1,then
*vwrite
('Guided proof mass,yes')
*else
*vwrite
('Guided proof mass,no')
*endif

*if,DETF,eq,1,then
*vwrite
('Tuning fork type,out-of-plane')
*vwrite
('width_centerbeam,spacing_beams,length_beams,width_anchor,
length_anchor,thickness_AlN1,thickness_botelec,thickness_AlN2')
*vwrite,w_beam,s_beam,l_beam,w_anchor,l_anchor,h_AlN1,h_botelec,h_AlN2
%9.3F,%9.3F,%9.3F,%9.3F,%9.3F,%9.3F,%9.3F,%9.3F
*else
*vwrite
('Tuning fork type,in-plane')
*vwrite
('width_beam,spacing_beams,length_beams,width_anchor,length_anchor,
width_tether,length_tether,thickness_AlN')
*vwrite,w_beam_IP,s_beam_IP,l_beam_IP,w_anchor_IP,l_anchor_IP,
w_tether_IP,l_tether_IP,h_AlN_IP
%9.3F,%9.3F,%9.3F,%9.3F,%9.3F,%9.3F,%9.3F,%9.3F
*endif
*vwrite
('Date,Time,Tilt(deg),X-accel(G),Y-accel(G),Z-accel(G),StrAlN1(MPa),
StrAlN2(MPa),MassThck(um),DETFuy(um),DETFuz(um),Mode1,Mode2,Mode3,Mode4,
Mode5,Mode6,Mode7,Mode8,Mode9,Mode10,Mode11,Mode12,Mode13,Mode14,Mode15,
Mode16,Mode17,Mode18,Mode19,Mode20')
/output
/gopr
```

```
!*do,stressdiff,-150,150,300
!*do,tilt,-180,180,90
!*do,h_bulk,50,400,50
!*do,y_acel,-1,1,0.25

x_acel=0 !x-acceleration in G
y_acel=0!-sin(tilt) !y-acceleration in G
z_acel=0!cos(tilt) !z-acceleration in G

stress_AlN1=-stressdiff/2
stress_AlN2=+stressdiff/2

finish
parsav,all,parameters,txt
/clear
parres,,parameters,txt

*afun,deg

/input,materialsfile(1),txt
et,1,solid186
et,2,mesh200,7

*if,DETF,eq,1,then
l_total=l_beam+2*l_anchor
w_total=w_anchor
h_total=h_AlN1+h_botelec+h_AlN2
rectng,-w_anchor/2,w_anchor/2,0,l_anchor
rectng,-w_beam/2,w_beam/2,0,2*l_anchor+l_beam
rectng,-w_beam-s_beam,-w_beam/2-s_beam,0,2*l_anchor+l_beam
rectng,w_beam/2+s_beam,w_beam+s_beam,0,2*l_anchor+l_beam
rectng,-w_anchor/2,w_anchor/2,l_anchor+l_beam,2*l_anchor+l_beam
aovlap,all
vext,all,,,,,h_AlN1
asel,s,loc,z,h_AlN1
vext,all,,,,,h_botelec
asel,s,loc,z,h_AlN1+h_botelec
vext,all,,,,,h_AlN2
*else
l_total=l_beam+2*l_anchor_IP+2*l_tether_IP
w_total=w_anchor
h_total=h_AlN_IP
rectng,-w_anchor_IP/2,w_anchor_IP/2,l_tether_IP,l_tether_IP+l_anchor_IP
rectng,-s_beam_IP/2-w_beam_IP,-s_beam_IP/2,l_tether_IP,l_tether_IP
+l_beam_IP+2*l_anchor_IP
```

```
rectng,s_beam_IP/2,s_beam_IP/2+w_beam_IP,l_tether_IP,l_tether_IP
+l_beam_IP+2*l_anchor_IP
rectng,-w_anchor_IP/2,w_anchor_IP/2,l_tether_IP+l_beam_IP+l_anchor_IP,
l_tether_IP+l_beam_IP+2*l_anchor_IP
rectng,-w_tether_IP/2,w_tether_IP/2,0,l_tether_IP+l_anchor_IP
rectng,-w_tether_IP/2,w_tether_IP/2,l_tether_IP+l_beam_IP+l_anchor_IP,
2*l_tether_IP+l_beam_IP+2*l_anchor_IP
aovlap,all
vext,all,,,,,h_AlN_IP
*endif


ptxy,-350,l_total+0,350,l_total+0,350,l_total+60
ptxy,100,l_total+310,-100,l_total+310,-350,l_total+60
poly
rectng,-350,-50,l_total-290,l_total+0
rectng,50,350,l_total-290,l_total+0

lsel,s,loc,x,-350
lsel,a,loc,x,350
asll,s,0
vext,all,,,,,h_total

*if,usebaseplate,eq,1,then
rectng,-300,300,-10,0
asel,s,loc,y,-10,0
asel,r,loc,z,0
vext,all,,,,,h_total
*endif

*if,proofmass,eq,1,then
wplane,,0,0,-h_bulk,1,0,-h_bulk,0,1,-h_bulk
ptxy,dele
ptxy,-340,l_total+0,340,l_total+0,340,l_total+55.858
ptxy,95.858,l_total+300,-95.858,l_total+300,-340,l_total+55.858
poly
rectng,-340,-60,l_total-280,l_total+0
rectng,60,340,l_total-280,l_total+0
asel,s,loc,z,-h_bulk
vext,all,,,,,h_bulk
*endif

vglue,all
asel,s,loc,x,-w_total/2,w_total/2
asel,r,loc,y,0,l_total
```

```
asel,r,loc,z,h_total

type,2
mshkey,1
mshape,0,2d
esize,60
amesh,all
allsel,below,area
lrefine,all,,,4

mat,1
vsel,s,loc,x,-w_total/2,w_total/2
vsel,r,loc,y,0,l_total
type,1
mshkey,1
mshape,0,3d
vmesh,all

vsel,s,loc,z,0,h_total
mshkey,0
mshape,1,3d
esize,60
vmesh,all

*if,proofmass,eq,1,then
vsel,s,loc,z,-h_bulk,0
esize,100
vmesh,all
*endif

*if,DETF,eq,1,then
vsel,s,loc,x,-w_anchor/2,w_anchor/2
vsel,r,loc,y,0,l_beam+2*l_anchor
vsel,r,loc,z,h_AlN1,h_AlN1+h_botelec
allsel,below,volu
mpchg,2,all
nsel,s,loc,x,-w_beam/2
nsel,r,loc,y,l_beam+2*l_anchor
nsel,r,loc,z,0
DETFTipNode=ndnext(0)
*else
nsel,s,loc,x,-w_tether_IP/2
nsel,r,loc,y,l_beam_IP+2*l_anchor_IP+2*l_tether_IP
nsel,r,loc,z,0
DETFTipNode=ndnext(0)
```

```
*endif

vsel,s,loc,z,-h_bulk,0
allsel,below,volu
mpchg,4,all

*if,usebaseplate,eq,1,then
nsel,s,loc,y,-10
*else
nsel,s,loc,y,0
*endif
d,all,ux,0,,,,uy,uz

*if,guidedmass,eq,1,then
nsel,s,loc,z,-h_bulk
d,all,uz,0
*endif

*if,fixedmass,eq,1,then
nsel,s,loc,z,-h_bulk
d,all,ux,0,,,,uy,uz
*endif

finish

/solu
allsel
antype,static
*if,nonlinearanalysis,eq,1,then
pstres,off
nlgeom,on
*else
pstres,on
nlgeom,off
*endif
acel,x_acel*9.81e6,y_acel*9.81e6,z_acel*9.81e6
*if,DETF,eq,1,then
inistate,set,dtyp,stre
vsel,s,loc,z,0,h_AlN1
vsel,r,loc,x,-w_total/2,w_total/2
vsel,r,loc,y,0,l_total
allsel,below,volu
esel,r,type,,1
inistate,define,,,,,stress_AlN1,stress_AlN1
vsel,s,loc,z,h_AlN1+h_botelec,h_AlN1+h_botelec+h_AlN2
```

```
vsel,r,loc,x,-w_total/2,w_total/2
vsel,r,loc,y,0,l_total
allsel,below,volu
esel,r,type,,1
inistate,define,,,,,stress_AlN2,stress_AlN2
*endif
allsel
solve
finish

/post1
*get,xdate,active,0,dbase,ldate
*get,xtime,active,0,dbase,ltime
str1 = strcat(chrval(xdate),'_')
str2 = strcat(str1,chrval(xtime))
/mkdir,str2
/CWD,maindirectory(1)
/cwd,str2
pldisp,0
/view,all,0,0,1
/angle,all,60,zs,0
/angle,all,-10,ys,1
/angle,all,-70,xs,1
/triad,off ! turn of the triad of the gloabl coordinate system
/plopts,minm,off ! turn of the display of minimum and maximum value
locations in contour plots
wpstyl,,,,,,,,0 ! turn of displaying of the working plane triad
/edge,all,1 ! set to 1 or 0 to turn off element edges
/dscale,1,6
/show,png,,0
PNGR,COMP,1,-1
PNGR,ORIENT,HORIZ
PNGR,COLOR,2
PNGR,TMOD,1
/GFILE,2400
/CMAP,_TEMPCMAP_,CMP,,SAVE
/RGB,INDEX,100,100,100,0
/RGB,INDEX,0,0,0,15
/REPLOT
/CMAP,_TEMPCMAP_,CMP
/DELETE,_TEMPCMAP_,CMP
/SHOW,CLOSE
/DEVICE,VECTOR,0
/CWD,maindirectory(1)
/dscale,1,auto
```

```
tipy=uy(DETFTipNode)
tipz=uz(DETFTipNode)
finish

*if,modalanalysis,eq,1,then
/solu
allsel
antype,modal
*if,nonlinearanalysis,eq,1,then
pstres,off
*else
pstres,on
*endif
*if,predeformed,eq,1,then
upcoord,1.0,on
*endif
modopt,lanb,50,1e1,2e7
solve
finish
*endif

/post1

fmatrix(1,1)=xdate
fmatrix(2,1)=xtime
fmatrix(3,1)=tilt
fmatrix(4,1)=x_acel
fmatrix(5,1)=y_acel
fmatrix(6,1)=z_acel
fmatrix(7,1)=stress_AlN1
fmatrix(8,1)=stress_AlN2
fmatrix(9,1)=h_bulk
fmatrix(10,1)=tipy
fmatrix(11,1)=tipz

*if,modalanalysis,eq,1,then

set,,1

*get,maxmode,active,0,set,nset,last
*do,i,1,20,1
*if,i,le,maxmode,then
*get,frequen,mode,i,freq
fmatrix(i+11,1)=frequen
!!! **** Save the mode shape images
```

```
set,,i
vsel,r,loc,x,-w_total/2,w_total/2 ! These 3 lines
vsel,r,loc,y,0,l_total ! are used to save only pictures
allsel,below,volu ! of the deformed
/replot,resize ! tuning fork.
/auto,1 ! Otherwise comment it out.
/CWD,maindirectory(1)
/cwd,str2
/show,png,,0
PNGR,COMP,1,-1
PNGR,ORIENT,HORIZ
PNGR,COLOR,2
PNGR,TMOD,1
/GFILE,1200 !2400
/CMAP,_TEMPCMAP_,CMP,,SAVE
/RGB,INDEX,100,100,100,0
/RGB,INDEX,0,0,0,15
/REPLOT
/CMAP,_TEMPCMAP_,CMP
/DELETE,_TEMPCMAP_,CMP
/SHOW,CLOSE
/DEVICE,VECTOR,0
/CWD,maindirectory(1)
*else
fmatrix(i+11,1)=0
*endif

!!! ****
*enddo
*endif

*mfun,fmatrixt,tran,fmatrix
/nopr
/output,%resultsstring%,csv,,append
*mwrite,fmatrixt
%G,%G,%12.3F,%12.3F,%12.3F,%12.3F,%12.3F,%12.3F,%12.3F,%12.6F,%12.6F,
%12.3F,%12.3F,%12.3F,%12.3F,%12.3F,%12.3F,%12.3F,%12.3F,%12.3F,%12.3F,
%12.3F,%12.3F,%12.3F,%12.3F,%12.3F,%12.3F,%12.3F,%12.3F,%12.3F,%12.3F
/output
/gopr

path,path1,2,10,200
ppath,1,,0,0,0
ppath,2,,0,l_total,0
pdef,defl,u,z
```

```
/header,off,off,off,off,off,off
prpath,defl

*enddo
*enddo
```

Appendix F

Circuit diagram of gyroscope circuit